Prospects for probing the structure of the proton with low-mass Drell-Yan events in ATLAS

by

Tayfun Ince
M.Sc. (Physics), University of Victoria, Victoria, Canada, 2005
B.Ed. (Physics), Marmara University, Istanbul, Turkey, 1999

A dissertation submitted in partial fulfilment
of the requirements for the degree of

DOCTOR OF PHILOSOPHY

in the Department of Physics and Astronomy.

Prospects for probing the structure of the proton with low-mass Drell-Yan events in ATLAS

by

Tayfun Ince
M.Sc. (Physics), University of Victoria, Victoria, Canada, 2005
B.Ed. (Physics), Marmara University, Istanbul, Turkey, 1999

Supervisory Committee

Dr. Richard K. Keeler, Supervisor
(Department of Physics and Astronomy)

Dr. Alan Astbury, Departmental Member
(Department of Physics and Astronomy)

Dr. Michel Lefebvre, Departmental Member
(Department of Physics and Astronomy)

Dr. Robert A. McPherson, Departmental Member
(Department of Physics and Astronomy)

Dr. David A. Harrington, Outside Member
(Department of Chemistry)

Supervisory Committee

Dr. Richard K. Keeler, Supervisor
(Department of Physics and Astronomy)

Dr. Alan Astbury, Departmental Member
(Department of Physics and Astronomy)

Dr. Michel Lefebvre, Departmental Member
(Department of Physics and Astronomy)

Dr. Robert A. McPherson, Departmental Member
(Department of Physics and Astronomy)

Dr. David A. Harrington, Outside Member
(Department of Chemistry)

Abstract

The biggest scientific experiment in history will begin taking data in late 2009 using the Large Hadron Collider (LHC) at CERN near Geneva, Switzerland. The LHC is designed to collide protons at an unprecedented 14 TeV centre of mass energy, enabling physicists to explore the constituents of matter at smaller scales than ever before. The Parton Distribution Functions (PDFs) are parametrizations of the proton structure and are best determined from experimental data. The PDFs are needed to calculate cross-sections or in other words the likelihood of observed physical processes, which are crucial in exploiting the discovery potential of the LHC. The prospects for measuring the Drell-Yan (DY) spectrum are assessed in the low invariant mass region below the Z boson resonance using e^+e^- pairs from the initial LHC data in order to probe the proton structure and further constrain the PDFs. The analysis is based on the full simulation of the ATLAS detector response to DY electrons and background processes. Assuming 100 pb^{-1} of LHC data, the total DY cross-section in the invariant mass range from 10 GeV to 60 GeV is expected to be measured as $\sigma_{\mathrm{DY}} = 5.90 \pm 0.24(\mathrm{stat}) \pm 0.18(\mathrm{syst})$ nb. The result predicts an improvement over a current theoretical uncertainty of 7.6% and indicates that the PDF uncertainties can be reduced significantly with the early LHC data.

Contents

List of Figures

List of Tables

Glossary of Abbreviations

ADC	Analogue to Digital Converter
AOD	Analysis Object Data
ATLAS	A Toroidal LHC ApparatuS
CERN	European Organization for Nuclear Research
CMS	Compact Muon Solenoid
DAQ	Data Acquisition
DIS	Deep Inelastic Scattering
DY	Drell-Yan
EF	Event Filter
EM	Electromagnetic
ESD	Event Summary Data
FSR	Final State Radiation
HLT	High Level Trigger
ISR	Initial State Radiation

LEP	Large Electron Positron Collider
LHC	Large Hadron Collider
LVL1	Level-1
LVL2	Level-2
MC	Monte Carlo
PDF	Parton Distribution Function
QCD	Quantum Chromodynamics
QED	Quantum Electrodynamics
RDO	Raw Data Object
RoI	Region of Interest
SCT	Semiconductor Tracker
SM	Standard Model
SPS	Super Proton Synchrotron
TRT	Transition Radiation Tracker

Acknowledgments

December 23rd, 2009 marks the end of an unforgettable period of my life as a graduate student. The LHC is the largest machine on earth and along with its detectors form the most sophisticated particle physics experiment ever built. Naturally, such a system is the work of many scientists and engineers including some of the greatest minds of our time. This dissertation is the product of a collective effort of many, and I would like to take this opportunity to name a few of these exceptional people.

I would like to thank: the UVic Physics and Astronomy department faculty, staff and my fellow graduate student colleagues for keeping this environment unique; the ATLAS Standard Model (SM) and Monte Carlo (MC) Generators groups for their insights and expertise, and the unified effort that led to the MC data analyzed in this work; the former SM group conveners Drs. Maarten Boonekamp, Tom LeCompte and Lucia Di Ciaccio; Maarten, in particular, for suggesting the low invariant mass region of the spectrum when I was in search of a project using the Drell-Yan process and supporting my work every step of the way; Dr. Monika Wielers for helping me understand all aspects of an electron trigger; my supervisory committee members Drs. Alan Astbury, Michel Lefebvre, Robert McPherson and David Harrington for their guidance and revisions; Michel for his inspirational passion for science and teaching me something new every time I step into his office; my external examiner Dr. Michel Vetterli; Frank Berghaus, Lorraine Courneyea and Greg King for being good friends, and fruitful discussions about physics and programming.

And, of course, the one person for whom I will always have trouble finding words to describe my gratitude is my supervisor Dr. Richard K. Keeler. Despite a Ph.D. degree and a much improved vocabulary, I will be the first to cite in acknowledgments and reference my M.Sc. thesis [31] as it is still the closest description of the greatness of Richard.

Aileme...

Sizlerin sonsuz desteğine layık olmak,

hayatımdaki en büyük hedef olmaya devam edecek.

Chapter 1

Introduction

The world of elementary particle physics is about to enter a new and exciting era. The Large Hadron Collider (LHC) [1] and its experiments (ATLAS, CMS, LHC-B, ALICE and TOTEM) [2] built and installed at CERN near Geneva, Switzerland will begin exploring the constituents of hadrons and hence matter at an unprecedented new energy scale. Higher energy implies studying the interactions of the constituents of matter at smaller distance scales; in other words, looking deeper into the structure of matter. The Standard Model (SM) [3, 4, 5] of particle physics embodies the current understanding of the elementary particles and their interactions. At this new energy scale, not only should it be possible to discover the origin of mass as predicted by the SM, but also potentially observe extensions to the SM [6] involving evidence of new physics.

The LHC will collide beams of protons. Protons are not fundamental, point-like, particles but consist of constituents collectively called partons. A proton-proton collision may be viewed as a collision between many partons. The cross-sections, or in other words the likelihood of observed physical processes, are measures of the interactions of the fundamental

particles that constitute matter and of the strength of the fundamental forces of nature. Therefore, determining the cross-sections is critical when studying a new energy regime and searching for new physics. In order to calculate a cross section at the LHC, one needs to know the probability of finding a particular pair of partons interacting at a given momentum transfer, Q, and carrying certain fractions, x, of the proton momentum. Such information is provided in the form of Parton Distribution Functions (PDFs), and currently these distributions have to be determined from experimental data. Since the LHC kinematic range in x and Q is much bigger than at any previous experiment, the PDF uncertainty is one of the dominant systematics and so it can limit discovery potential for new physics. The very high beam intensities at the LHC will mean that statistical uncertainties on the SM measurements will be negligibly small at the LHC, leaving the PDF uncertainty as one of the biggest uncertainties. Precision measurements of SM processes will improve the constraints on the most likely value of the mass of the Higgs boson and may provide evidence for new physics.

Various measurements are planned at the LHC to further constrain the PDFs. The Drell-Yan (DY) process, first described by Sidney D. Drell and Tung-Mow Yan in 1970 [7], is a key process for reaching this objective because it is a well understood process of a parton from one proton annihilating with an anti-parton from another proton producing oppositely charged leptons. The DY process historically has played a critical part in the study of the constituents of hadrons and their distributions. Particles such as the J/ψ in 1974 [8], the Υ in 1977 [9] and the Z boson in 1983 [10] are examples of discoveries that

resulted from the study of the invariant mass spectrum of the DY lepton pairs.

The charged leptons, electrons and muons specifically, are the most readily detected and arguably the most easily detectable particles of the SM by the detectors used in particle physics experiments like ATLAS working in the very complicated environment of pp collisions as will be further explained in more detail in section 2.1. Hence, a process like DY that requires two leptons in the final state has significant practical experimental advantages. The DY process therefore will play an important role in many of the physics goals envisioned at the LHC from day one until the end. Moreover, since the lepton pair comes from the annihilation of a quark and an antiquark, DY probes a well defined initial state.

This dissertation studies the prospects for measuring the Drell-Yan spectrum at low invariant mass, 10 GeV $-$ 60 GeV, using e^+e^- pairs from the initial LHC data in order to further constrain the PDFs. The Standard Model of particle physics and the LHC experimental program are briefly summarized in the following sections of this introduction. Chapter 2 provides an overview of the current theoretical understanding of the proton structure and of the Drell-Yan process as well as motivations for studying such a process at the LHC. Background processes that may leave a Drell-Yan like signature in the detectors and may present a challenge for the intended measurement are also discussed following the DY theory. Chapter 3 describes the design and expected performance of the experimental apparatus with particular focus on the ATLAS detector components to be used for this work. Chapter 4 introduces the ATLAS Monte Carlo that produced the full simulation of the detector response to DY electrons and background processes used to assess the prospects

of the intended measurement with the early LHC data. Chapter 5 studies reconstruction and identification of an electron signature in the detector, efficient electron pair selection criteria that will distinguish DY electrons from other background electrons, and estimation and reduction of the dominant background process. Chapter 6 calculates efficiencies and detector limitations in measuring DY electrons. Chapter 7 presents the expected low mass Drell-Yan spectrum before and after corrections. Chapter 8 investigates potential systematic errors. Chapter 9 compares the expected results with the current theoretical knowledge and uncertainties including previous experiments. A set of Drell-Yan electron identification criteria is proposed for the early running of the LHC in this chapter, as well. Finally, conclusions drawn from this work are given in chapter 10.

1.1 The Standard Model

The Standard Model is the theory of elementary particles and their interactions via the electromagnetic (EM), the weak and the strong forces.

Leptons, quarks and bosons (force carriers) are the categories of observed fundamental particles in the SM. They are listed in Figure 1.1. Leptons and quarks are half-integer-spin fermions that are divided into three generations. There is a corresponding antifermion with same mass and spin but opposite-charge-like quantum numbers for each type of lepton and quark. The first generation of fermions contains the particles from which all the ordinary matter in nature is constituted.

Leptons interact via the weak force and, if electrically charged, the EM force, while quarks carry an additional colour charge and hence interact via the strong force as well. The

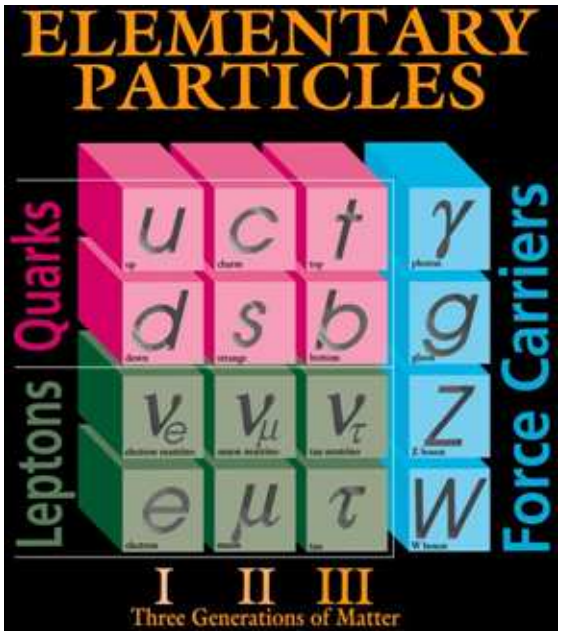

Figure 1.1: The elementary particles of the Standard Model.

nature of the strong force prevents quarks from being observed in isolation, and therefore quarks always appear in the form of colour-singlet particles called hadrons. In other words, hadrons consist of colour-singlet combinations of quarks. The pion, proton and neutron are examples of hadrons.

The SM is based on three relativistic quantum field theories: Quantum Electrodynamics (QED), the theory of weak interactions and Quantum Chromodynamics (QCD). QED describes the interactions of charged fermions (e, μ, τ and quarks). The theory of weak interactions explains the neutral weak interactions and the charged weak interactions that change the flavour of fermions from one to another. QED and the theory of weak interactions are unified to form the theory of electroweak interactions. QCD describes the strong interactions between quarks.

The interactions between fermions are mediated by integer-spin gauge bosons: the photon (γ) is the mediator of the EM force, the $W^{\pm}$ and Z gauge bosons are the mediators of the weak force, and there are eight gluons (g) that are the mediators of the strong force. The SM is a gauge theory (i.e. symmetric under local phase or gauge transformations), and hence the gauge bosons in principle should be massless. However, the $W^{\pm}$ and Z bosons are massive and acquire mass without violating the gauge invariance through a process called the Higgs Mechanism that introduces a scalar Higgs field. An observable consequence of the Higgs field is a new massive scalar (i.e. spinless) particle called the Higgs boson.

The predictions of the SM have been tested to exceptionally high precision (better than 0.1% in some cases) by a large number of complementary experiments. However, the SM cannot be the complete theory of fundamental physics as it has several universally agreed inadequacies such as: the unverified origin of mass; lack of explanation for why there are exactly three generations; gravity is not included in the theory; and there is no explanation for dark matter.

1.2 Experimental program

The designs of the LHC and the ATLAS detector [11] have been driven by several physics goals. They include understanding how electroweak symmetry is broken, making precision measurements of the SM parameters, studying the structure of the proton and searching for potential new physics beyond the SM.

The breaking of the electroweak symmetry is apparent from the observation that the weak force carriers, $W^{\pm}$ and Z bosons, have mass while the electromagnetic force carrier,

γ, is a massless particle. In the SM, the Higgs mechanism is considered to be responsible for hiding the electroweak symmetry. All elementary particles that have mass acquire their masses through the strength of their interactions with the Higgs field. Massless particles like the γ do not directly interact with the Higgs field. The Higgs boson is the only particle that is predicted by the SM, but not discovered yet, although, indirect methods and direct searches at the previous LEP experiments place a lower limit of 114 GeV on its mass. Assuming that the Higgs boson exists, the ATLAS experiment will be capable of finding it over the entire theoretically allowed mass range. The measured properties of the Higgs boson will fix the parameters of the electroweak symmetry breaking process.

The very high luminosity, the number of particles per unit area per second crossing at the point where the beams meet, and centre of mass energy design of the LHC will allow more precisely measured SM parameters. For example, the masses of the $W^{\pm}$ and Z bosons, triple gauge boson couplings, and especially the mass of the t quark and its couplings will all be improved. The collisions at this new energy regime will also extend the current knowledge of the substructure (see section 2.1) of protons.

As noted in section 1.1, the SM is not thought to be the complete theory of particles. There are various possible extensions proposed to the SM, for example Supersymmetry [12]. The ATLAS experiment will have the capability to discover or exclude new supersymmetric particles over a large portion of the theoretically possible masses and coupling strengths as well as offering the opportunity to search for new heavy gauge bosons (e.g. Z') and quarks.

Chapter 2

Theory

The current theoretical understanding of the structure of the proton and of pp collisions is described by the Parton Model and QCD.

In this chapter, the Parton Model is introduced including the effects of QCD. The physics motivations behind the study of the Drell-Yan process are described. A mathematical description is given of the cross section calculated at leading and next-to-leading orders. The production of an e^+e^- pair via the DY process is studied in this work. Therefore, background processes that have an e^+e^- pair(s) in their final state or leave DY-like signatures in the ATLAS detector are also presented.

2.1 Proton-proton collisions

Protons are used at high energy particle colliders like the LHC due to their stability and large mass compared to electrons. However, protons are not fundamental, point-like, particles which makes pp collisions rather complicated.

2.1.1 The Parton Model with QCD

QCD, in contrast to QED, is a non-Abelian gauge theory [13] or in other words the gauge or local symmetry transformations under which the theory is invariant form a non-commutative group. Hence the fields' quanta, gluons, can interact with each other as well as being the force carriers of the strong coupling between quarks. As a result of the self interactions of the gluons and the specific number of types of quarks in nature, the strength of the coupling between strongly interacting partons increases at lower momentum transfers, Q^2, or long distances. This leads to confinement of quarks and gluons into hadrons. Therefore, the perturbation theory fails when treating strong interactions at low momentum transfers (often referred to as soft interactions). Due to the difficulties of non-perturbative calculation methods, soft interactions in QCD are not calculable quantitatively in a reliable way. At high momentum transfers or short distances, the strong coupling weakens such that quarks and gluons can be considered as free particles and perturbative calculations are possible. This is also known as asymptotic freedom.

In the Parton Model with QCD, protons consist of three valence quarks, uud, and a sea of virtual quarks and gluons. The sea quarks and gluons are produced through a mechanism analogous to bremsstrahlung and pair production in QED. When observed in high energy collisions, valence quarks are seen to radiate gluons that can produce virtual quark-antiquark ($q\bar{q}$) or gluon pairs and that these virtual particles in turn can radiate gluons as well. The virtual quarks are called sea quarks. Valence quarks, sea quarks and gluons are collectively called partons.

A pp collision can be considered as a collision between partons. Each parton carries only a fraction (e.g. a valence quark, on average, carries approximately 15% at the LHC energies) of the proton momentum, so the collision between two partons is not in the centre of mass frame but generally is boosted along the beam axis.

In pp collisions, most of the time, partons interact via soft scattering, low momentum transfer, and only a few hard scattering, large momentum transfer, events happen that are of interest for discovering new physics. The final state after a hard scatter interaction in a pp collision may contain leptons, quarks and gauge bosons. If a parton, quark or gluon is produced in the final state, then it will not remain isolated, as mentioned in section 1.1, but will undergo a process called hadronization that results in many hadrons, collectively called a jet that will have a direction collinear with the originally struck parton. Figure 2.1 illustrates a pp collision where a parton a from a proton A interacts with a parton b from a proton B with an interaction cross-section given by $\hat{\sigma}$ to produce a final state $c + X$.

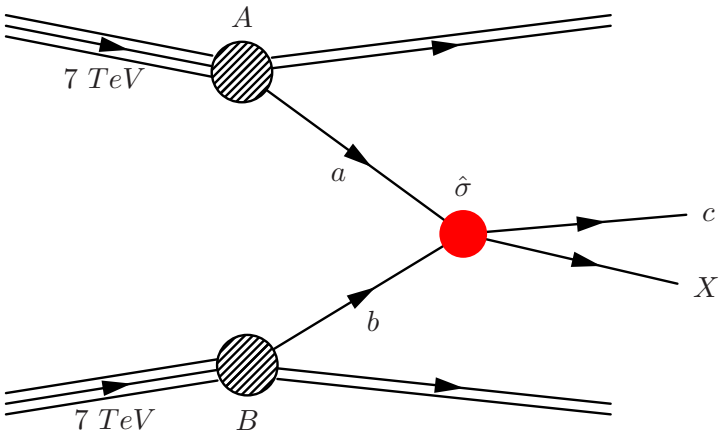

Figure 2.1: Schematic diagram of a proton-proton collision.

The Parton Model, requires a knowledge of how the partons are distributed in a proton. This is known as the parton distribution function (PDF). The PDF, denoted as $f_{a/A}(x_a, Q^2)$, gives the probability density of finding a parton a with a momentum fraction x_a when probed by a fixed momentum transfer Q^2 in a proton A. Due to the non-perturbative nature of QCD at low Q^2, the PDFs must be determined experimentally. CTEQ [14] and MRST [15] are the two main groups providing PDFs by analyzing all the available experimental data using a global fitting procedure. The PDFs are essential input to the precision measurements of the SM at a hadron collider and are needed to calculate the cross-section of a given physical process in pp or other hadron-hadron collisions.

The uncertainty of PDFs increases at low x and high Q^2 due to the lower interaction energies and the amount of data that were available at previous experiments. The kinematic range of partons at the LHC in terms of Q^2 and x is presented in figure 2.2 including the kinematic reach of HERA [16] and fixed target experiments. As can be seen, although the data from HERA and fixed target experiments cover the kinematic range of the LHC in terms of x within the geometrical acceptance of the ATLAS detector, the LHC will provide these momentum fractions x in a much bigger range of Q^2.

For instance, consider a process $A + B \to c + X$ where c is a fermion and X can be any particle or multiple particles. See appendix A for a more detailed description of the kinematics. The total cross-section σ for producing the fermion c, in the lowest order (LO), is calculated as [18]

$$(\sigma)_{\mathrm{LO}} = \sum_{a,b} C_{ab} \int dx_a dx_b \left[f_{a/A}(x_a, Q^2) f_{b/B}(x_b, Q^2) + (A \leftrightarrow B \text{ if } a \neq b) \right] \hat{\sigma} \qquad (2.1)$$

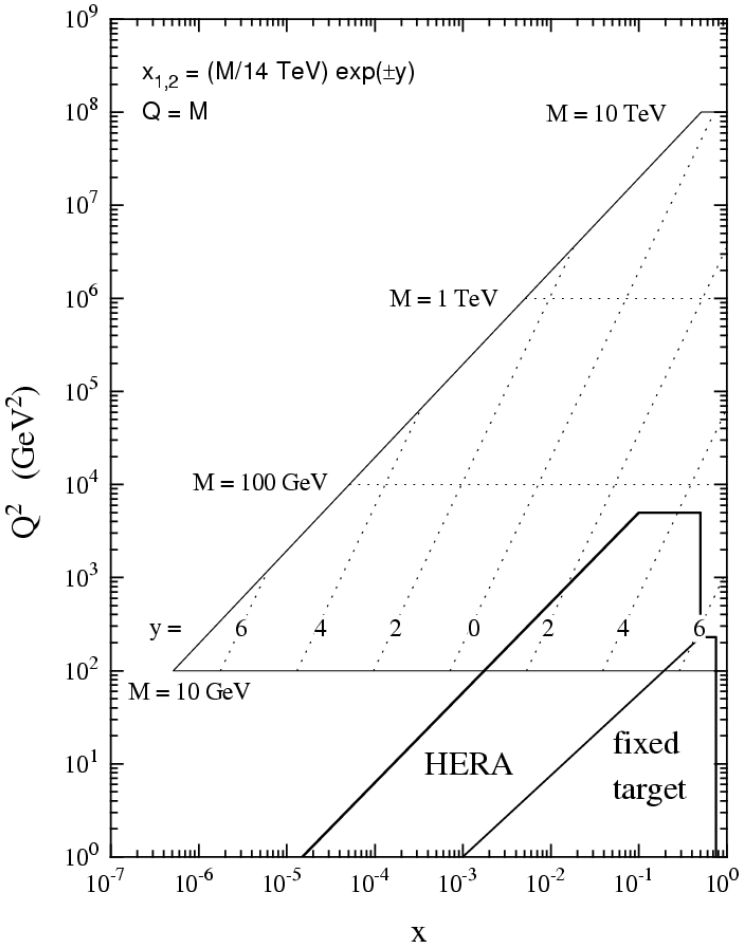

Figure 2.2: Kinematic range of partons at the LHC [17]. Shown are values of Q^2 versus x including kinematic reach of the HERA and fixed target experiments.

where a and b are the partons in the protons A and B respectively, C_{ab} is the initial colour-averaging factor, $\hat{\sigma}$ represents the subprocess or constituent level cross section for the interaction of the two partons a and b to form the final state c and X, and $\sum$ is the sum over all possible parton pairs, including all possible colours, that can produce $c + X$. The term $A \leftrightarrow B$ is

$$A \leftrightarrow B \equiv f_{a/B}(x_b, Q^2) f_{b/A}(x_a, Q^2)$$

to account for the possibility of the parton a coming from the proton B carrying a momentum fraction x_b and the parton b coming from the proton A carrying a momentum fraction x_a. The initial colour averaging factors for quarks and gluons are

$$C_{q\bar{q}} = \frac{1}{9} \ , \ C_{qg} = \frac{1}{24} \ , \ C_{gg} = \frac{1}{64}$$

since there are three and eight different colour-charges carried by each quark and gluon, respectively.

The momentum fraction $x_{a,b}$ carried by each parton, ignoring the parton masses, is given by

$$p_{a,b} = x_{a,b} p_{A,B} \tag{2.2}$$

where $p_{a,b}$ ($p_{A,B}$) represents the four-momentum of each parton (proton). Thus, the invariant mass squared $\hat{s}$ of the parton pair, assuming that the protons are in the centre of mass frame and there is no angle between the interacting partons, is

$$\hat{s} = (p_a + p_b)^2 = x_a x_b s = \tau s \tag{2.3}$$

where s is the invariant mass squared of the proton pair and the variable $\tau = x_a x_b$, a number between 0 and 1, is defined in order to simplify future formulations. Rewriting the cross-section in terms of x_a and τ yields

$$(\sigma)_{\mathrm{LO}} = \sum_{a,b} C_{ab} \int_0^1 d\tau \int_\tau^1 \frac{dx_a}{x_a} \left[f_{a/A}(x_a, Q^2) f_{b/B}(\frac{\tau}{x_a}, Q^2) + (A \leftrightarrow B \text{ if } a \neq b) \right] \hat{\sigma} \tag{2.4}$$

and hence, the differential cross-section can be written as

$$\left(\frac{d\sigma}{d\tau} \right)_{\mathrm{LO}} = \sum_{a,b} \frac{d\mathcal{L}_{ab}}{d\tau} \hat{\sigma}(\hat{s} = \tau s) \tag{2.5}$$

where

$$\frac{d\mathcal{L}_{ab}}{d\tau} = C_{ab} \int_{\tau}^{1} \frac{dx_a}{x_a} \left[f_{a/A}(x_a, Q^2) f_{b/B}(\frac{\tau}{x_a}, Q^2) + (A \leftrightarrow B \text{ if } a \neq b) \right] \tag{2.6}$$

is called the parton luminosity since multiplication of it with the parton cross-section $\hat{\sigma}$ gives the total cross-section in a pp (or hadron-hadron) collision.

In hadron-hadron collisions, it is more convenient to use rapidity, y, in calculations of cross-sections or other observables since the hard scatter (ab system) centre of mass moves in the lab frame (i.e. x_a and x_b are not necessarily equal) along the beam axis, and the shapes of observable distributions in y are relativistically invariant. The rapidity is a variable that transforms simply, by adding a constant, under boosts. It is defined as

$$y = \frac{1}{2} \ln \left(\frac{E^{(\text{c.m.})} + p_{||}^{(\text{c.m.})}}{E^{(\text{c.m.})} - p_{||}^{(\text{c.m.})}} \right) = \frac{1}{2} \ln \frac{x_a}{x_b} \tag{2.7}$$

where $E^{(\text{c.m.})}$ is the energy and $p_{||}^{(\text{c.m.})}$ is the longitudinal momentum of the ab system in the AB centre of mass frame. The AB centre of mass frame is the lab frame for the LHC. Pseudorapidity is often used as an approximation for y when the mass of a particle is small compared to its energy and is defined as $\eta = -\ln\left(\tan\frac{\theta}{2}\right)$ where θ is the polar angle. The rapidity can be written in terms of x_a and x_b only when assuming that the partons are massless and there is no angle between them. The momentum fraction $x_{a,b}$ can be rewritten in terms of y and τ as

$$x_{a,b} = \sqrt{\tau} e^{\pm y} \tag{2.8}$$

and therefore the differential cross-section in terms of y and τ is

$$\left(\frac{d^2\sigma}{dy d\tau} \right)_{\text{LO}} = \frac{d^2\sigma}{dx_a dx_b} = \sum_{a,b} C_{ab} \left[f_{a/A}(x_a, Q^2) f_{b/B}(\frac{\tau}{x_a}, Q^2) + (A \leftrightarrow B \text{ if } a \neq b) \right] \hat{\sigma} \tag{2.9}$$

and therefore,

$$\frac{d^2\sigma}{dyd\tau} = (x^2 + 4\tau)^{\frac{1}{2}} \frac{d^2\sigma}{dxd\tau}$$

where $x = x_a - x_b$ is the longitudinal momentum fraction of the ab system or, along with τ, one can write $x_{a,b} = \frac{1}{2}[(x^2 + 4\tau)^{\frac{1}{2}} \pm x]$.

2.1.2 QCD corrections to the Parton Model

The Parton Model formalism given in the previous section is at a fixed Q^2 and hence does not include the possibility that additional gluons can be emitted or exchanged by the hard interacting partons due to the strong interaction. Allowing for such gluon exchange (or emission) creates singularities in the calculation of the cross-section. The singularities are due to divergences from very soft gluon emission (non-perturbative part of QCD as mentioned in section 2.1.1) and gluon emission parallel to the incoming quark. These divergences are often referred to as infrared and collinear, respectively. Fortunately, these singularities can be factored into the PDFs.

The PDFs including soft QCD corrections are calculated with the Dokshitzer-Gribov-Lipatov-Altarelli-Parisi (DGLAP) equations [19]:

$$\begin{aligned} t\frac{\partial}{\partial t}\begin{pmatrix} q_i(x,t) \\ g(x,t) \end{pmatrix} &= \frac{\alpha_s(t)}{2\pi} \sum_{q_i,\bar{q}_j} \int_x^1 \frac{d\xi}{\xi} \\ &\times \begin{pmatrix} P_{q_iq_j}\left(\frac{x}{\xi}, \alpha_s(t)\right) & P_{q_ig}\left(\frac{x}{\xi}, \alpha_s(t)\right) \\ P_{gq_j}\left(\frac{x}{\xi}, \alpha_s(t)\right) & P_{gg}\left(\frac{x}{\xi}, \alpha_s(t)\right) \end{pmatrix} \begin{pmatrix} q_j(\xi,t) \\ g(\xi,t) \end{pmatrix} \end{aligned} \quad (2.10)$$

where $t = \mu^2$ is the factorization scale and the running coupling constant, $\alpha_s(\mu^2)$, [12] of the strong interactions is

$$1/\alpha_s(\mu^2) \equiv \frac{33 - 2N_f}{12\pi} \ln \frac{\mu^2}{\Lambda^2} \quad (2.11)$$

where Λ is the QCD scale parameter and N_f is the number of quark flavours that have masses less than μ. The $q_i(x,t)$ and $g(x,t)$ both are PDFs (equivalent of $f(x,Q^2)$ in equation 2.1) and represent quark and gluon distributions, respectively. The splitting functions can be calculated as

$$P_{q_iq_j}(x,\alpha_s) = \delta_{ij}P^{(0)}_{qq}(x) + \frac{\alpha_s(t)}{2\pi}P^{(1)}_{q_iq_j}(x) + ... \quad (2.12)$$

$$P_{qg}(x,\alpha_s) = P^{(0)}_{qg}(x) + \frac{\alpha_s(t)}{2\pi}P^{(1)}_{qg}(x) + ... \quad (2.13)$$

$$P_{gq}(x,\alpha_s) = P^{(0)}_{gq}(x) + \frac{\alpha_s(t)}{2\pi}P^{(1)}_{gq}(x) + ... \quad (2.14)$$

$$P_{gg}(x,\alpha_s) = P^{(0)}_{gg}(x) + \frac{\alpha_s(t)}{2\pi}P^{(1)}_{gg}(x) + ... \quad (2.15)$$

where δ_{ij} is the Kronecker delta function. To the lowest order, the splitting functions can be expressed as

$$P^{(0)}_{qq} = C_F\left[\frac{1+x^2}{(1-x)_+} + \frac{3}{2}\delta(1-x)\right] \quad (2.16)$$

$$P^{(0)}_{qg} = T_R\left[x^2 + (1-x)^2\right] \quad (2.17)$$

$$P^{(0)}_{gq} = C_F\left[\frac{1+(1-x)^2}{x}\right] \quad (2.18)$$

$$P^{(0)}_{gg} = 2C_A\left[\frac{x}{(1-x)_+} + \frac{1-x}{x} + x(1-x) + \delta(1-x)\frac{(11C_A - 4N_cT_R)}{6}\right] \quad (2.19)$$

where $\delta(1-x)$ is the Dirac delta function, $N_c = 3$ is the number of colour-charges, $C_A = 3$, $T_R = \frac{1}{2}$, $C_F = \frac{N_c^2-1}{2N_c}$, and the plus sign denotes that

$$\frac{1}{(1-x)_+} \equiv \frac{1}{1-x} \quad \text{for} \quad 0 \le x < 1 \quad (2.20)$$

$$\int_0^1 dx \frac{f(x)}{(1-x)_+} \equiv \int_0^1 dx \frac{f(x)-f(1)}{1-x}\ . \quad (2.21)$$

Once the singularities are factored into the PDFs, the remaining corrections coming

from high momentum transfer interactions between gluons and quarks are finite and can be added to LO cross section perturbatively in α_s. Therefore, the QCD improved version of the equation 2.1 can be written as [19]

$$\begin{aligned}\sigma &= \sum_{a,b} C_{ab} \int dx_a dx_b \left[f_{a/A}(x_a, Q^2) f_{b/B}(x_b, Q^2) + (A \leftrightarrow B \text{ if } a \neq b) \right] \\ &\times \left[\hat{\sigma}_0 + \frac{\alpha_s(Q^2)}{2\pi} \hat{\sigma}_1 + \left(\frac{\alpha_s(Q^2)}{2\pi} \right)^2 \hat{\sigma}_2 + ... \right] \end{aligned} \tag{2.22}$$

where the power of α_s (i.e. the order of perturbation) is equivalent to the number of gluon emissions allowed in the process. The next-to-leading order (NLO) correction, $\mathcal{O}(\alpha_s)$, to the cross-section is sometimes approximated as an effective constant known as the K-factor so that

$$(\sigma)_{\text{NLO}} = K \, (\sigma)_{\text{LO}} \ . \tag{2.23}$$

2.2 Drell-Yan physics

The Parton Model was originally developed for Deep Inelastic Scattering (DIS) and first applied to the DY processes in hadron-hadron collisions.

2.2.1 Introduction

As introduced in the first chapter, the DY process will be key at the LHC for understanding the performance of and calibration of the ATLAS detector that will be necessary in order to search for new physics. The e^+e^- final state is the focus of this dissertation. The excellent tracking and EM calorimeters combined with the transition radiation detector of ATLAS provide good electron identification.

The LHC will produce many more DY pairs over a larger invariant mass range than any other collider experiment conducted before and hence will allow further study of the structure of the proton and can improve the accuracy of the PDFs, especially at low-x approximately down to 10^{-4}.

The very large amount of data that can be collected at the LHC using the well known and understood SM processes such as the production and decay of the Z boson will also make the DY process a key in improving the accuracy of the mass, m_W, of the $W^{\pm}$ bosons, and hence the mass, m_t, of the top quark. These more precise measurements will improve the constraints on the most likely value of the mass, m_H, of the Higgs boson and will help increase the discovery potential.

The DY process will be essential in searches for new physics at the LHC as well. The search for new heavy gauge bosons such as Z', is possible through the decay channels of such particles into DY pairs.

At LHC energies, production mechanisms for both the known physics processes such as inclusive jets and the potential new physics predicted will mostly involve the scattering of gluons. Strong interactions of gluons are governed by the QCD part of the SM. Therefore, a detailed understanding of the QCD phenomena is vital for almost all of the physics at the LHC. QCD is highly successful at describing the strong interactions at high momentum transfers, Q^2, where perturbative methods based on asymptotic freedom can be applied. However, at low-Q^2, perturbative methods are not applicable or at best can be approximated by resummation of some perturbative terms in all orders. Moreover, there is a lack of

experimental data at low-x, where the non-perturbative part of QCD becomes important. Hence, the theoretical uncertainties are currently large for the low-x part of QCD. The measurement described in this dissertation will provide a good test of QCD at low-x and requires an in-depth study of inclusive jet events.

2.2.2 Tree level process

The Drell-Yan process consists of a quark-antiquark annihilation creating a virtual photon or Z boson which then produces a lepton-antilepton pair, $q\bar{q} \to \gamma^*/Z \to \ell^+\ell^-$. The formula can be expressed as the Feynman diagram shown in figure 2.3.

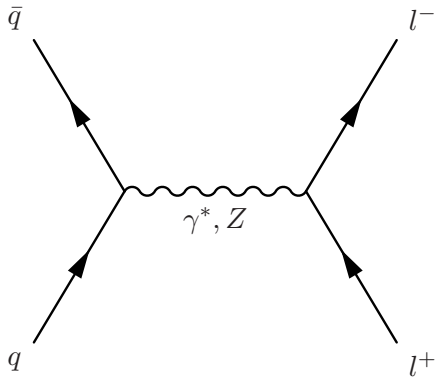

Figure 2.3: Feynman diagram of the tree level Drell-Yan process.

The total cross-section for producing a DY pair (i.e. lepton-antilepton pair) can be calculated to LO in the parton model [19] described in section 2.1.1 (more of the mathematical details are given in appendix A) and is given by

$$(\sigma)_{LO} = \sum_q \int dx_1 dx_2 \left[f_{q/A}(x_1, m_{ll}^2) f_{\bar{q}/B}(x_2, m_{ll}^2) + (q \leftrightarrow \bar{q}) \right] \hat{\sigma}_{q\bar{q}\to l^+l^-} \tag{2.24}$$

where unlike for a p$\bar{\text{p}}$ collision, the $q \leftrightarrow \bar{q}$ term is added explicitly rather than multiplying with a factor of two since there is an imbalance of quarks and anti-quarks in a pp collision

because there are no valence antiquarks in a proton. In the lowest order, the subprocess cross-section $\hat{\sigma}$ due to the exchange of a virtual photon is given by

$$\hat{\sigma}(q(p_1)\bar{q}(p_2) \to \gamma^* \to l^+l^-) = N_c C_{q\bar{q}} \frac{4\pi\alpha^2}{3\hat{s}} e_q^2 \tag{2.25}$$

where $\hat{s} = (p_1 + p_2)^2 = m_{ll}^2$, e_q is the quark electric charge, and p_1 and p_2 are the four-momenta of the quarks. The running electromagnetic coupling, $\alpha \equiv \alpha(m_{ll}^2)$, is given by

$$\alpha(m_{ll}^2) = \frac{\alpha(m_e^2)}{1 - \frac{\alpha(m_e^2)}{3\pi}\left[\sum_f e_f^2 N_c \left(\ln\frac{m_{ll}^2}{m_f^2} - \frac{5}{3}\right)\right]} \tag{2.26}$$

with the fine structure constant $\alpha(m_e^2) = 1/137.036$ [12]. N_c is equal to one for leptons and three for quarks. m_{ll} is the invariant mass of the lepton pair while m_f represents the fermion masses less than m_{ll}. The factor $N_c C_{q\bar{q}} = \frac{1}{3}$ reflects the fact that only three of nine colour combinations from a quark and antiquark pair are possible matching colours that can lead to a colourless virtual photon. The subprocess differential cross-section for producing a DY pair of invariant mass squared m_{ll}^2 can be calculated as

$$\frac{d\hat{\sigma}}{dm_{ll}^2} = N_c C_{q\bar{q}} \frac{4\pi\alpha^2}{3m_{ll}^2} e_q^2 \delta(\hat{s} - m_{ll}^2) \tag{2.27}$$

where the Dirac delta function $\delta(\hat{s} - m_{ll}^2)$ imposes $\hat{s} = m_{ll}^2$. Hence the total differential cross-section is given by

$$\begin{aligned}
\left(\frac{d\sigma}{dm_{ll}^2}\right)_{LO} &= \int_0^1 dx_1 dx_2 \sum_q \left[f_{q/A}(x_1, m_{ll}^2) f_{\bar{q}/B}(x_2, m_{ll}^2) + (q \leftrightarrow \bar{q})\right] \times \frac{d\hat{\sigma}}{dm_{ll}^2}(q\bar{q} \to l^+l^-) \\
\left(\frac{d\sigma}{dm_{ll}^2}\right)_{LO} &= N_c C_{q\bar{q}} \frac{4\pi\alpha^2}{3m_{ll}^2} \int_0^1 dx_1 dx_2 \delta(x_1 x_2 s - m_{ll}^2) \\
&\quad \times \sum_q e_q^2 \left[f_{q/A}(x_1, m_{ll}^2) f_{\bar{q}/B}(x_2, m_{ll}^2) + (q \leftrightarrow \bar{q})\right]
\end{aligned} \tag{2.28}$$

and finally rewriting this equation in terms of $\tau = m_{ll}^2/s$ yields

$$\begin{aligned}\left(\frac{d\sigma}{dm_{ll}^2}\right)_{LO} &= N_c C_{q\bar{q}} \frac{4\pi\alpha^2}{3m_{ll}^4}\tau \int_0^1 dx_1 dx_2 \delta(x_1 x_2 - \tau) \\ &\quad \times \sum_q e_q^2 \left[f_{q/A}(x_1, m_{ll}^2) f_{\bar{q}/B}(x_2, m_{ll}^2) + (q \leftrightarrow \bar{q})\right] \\ \left(\frac{d\sigma}{dm_{ll}^2}\right)_{LO} &= N_c \frac{4\pi\alpha^2}{3m_{ll}^4} \sum_q e_q^2 \frac{\tau d\mathcal{L}(\tau)}{d\tau} \qquad (2.29) \\ \left(\frac{d\sigma}{dm_{ll}}\right)_{LO} &= N_c \frac{8\pi\alpha^2}{3m_{ll}^3} \sum_q e_q^2 \frac{\tau d\mathcal{L}(\tau)}{d\tau} \qquad (2.30)\end{aligned}$$

which depends on τ and m_{ll}. $\frac{d\mathcal{L}(\tau)}{d\tau}$ was defined in equation 2.6. Note that the differential cross-section $\frac{d\sigma}{dm_{ll}}$ is inversely proportional to the cube of the DY lepton pair invariant mass m_{ll}, i.e. $\frac{d\sigma}{dm_{ll}} \propto \frac{1}{m_{ll}^3}$. The double differential cross-section with respect to τ and y can be written as [6]

$$\left(\frac{d^2\sigma}{dm_{ll}dy}\right)_{LO} = N_c C_{q\bar{q}} \frac{8\pi\alpha^2}{3m_{ll}^3}\tau \sum_q e_q^2 \left[f_{q/A}(\sqrt{\tau}e^y, m_{ll}^2) f_{\bar{q}/B}(\sqrt{\tau}e^{-y}, m_{ll}^2) + (q \leftrightarrow \bar{q})\right] \quad (2.31)$$

To include the contributions from the Z boson, the following replacement of e_q^2 by three terms, including contributions from γ-Z interference (second term) and the Z boson (third term) derived using the formulae in appendix A of [20], is needed in the previous equations:

$$\begin{aligned}e_q^2 \quad \rightarrow \quad & e_q^2 + \frac{m_{ll}^2(m_{ll}^2 - m_Z^2)(1 - 4\sin^2\theta_W)}{8\sin^2\theta_W \cos^2\theta_W \left[(m_{ll}^2 - m_Z^2)^2 + m_Z^2\Gamma_Z^2\right]} \upsilon_i e_q \\ & + \frac{3m_{ll}^4 \Gamma_{Z\rightarrow l^+l^-}}{16\alpha m_Z \sin^2\theta_W \cos^2\theta_W \left[(m_{ll}^2 - m_Z^2)^2 + m_Z^2\Gamma_Z^2\right]} (\upsilon_i^2 + 1) \qquad (2.32)\end{aligned}$$

where m_Z, Γ_Z and $\Gamma_{Z\rightarrow l^+l^-}$ are the mass, the full width and the partial width of the Z boson respectively and have been determined experimentally. The partial width of a particle is the probability of the particle's decay into a particular final state times the full width which

is inversely proportional to the lifetime of that particle. For up-type quarks (i.e. u,c,t), υ_i is $\upsilon_u = 1 - \frac{8}{3}\sin^2\theta_W$, and for down-type (i.e. d,s,b) quarks, it is $\upsilon_d = -1 + \frac{4}{3}\sin^2\theta_W$ with θ_W as the Weinberg angle.

2.2.3 Higher order corrections

Higher order QCD corrections to the DY cross-section are due to interactions with gluons, as discussed in section 2.1.2. The first order, $\mathcal{O}(\alpha_s)$, processes contributing to the tree level DY process are given in figure 2.4 where (a) shows virtual gluon corrections to the annihilating $q\bar{q}$ in the initial state, (b) shows a real gluon emission in the process of producing the γ^*/Z, resulting in a DY pair plus a gluon final state, (c) shows the gluon-quark(antiquark) scattering processes that lead to the desired final state DY pair and an additional parton.

The QCD corrected total cross-section for the DY process can be written as [19]

$$\sigma = \sum_q \int dx_1 dx_2 \left[f_{q/A}(x_1, m_{ll}^2) f_{\bar{q}/B}(x_2, m_{ll}^2) + (q \leftrightarrow \bar{q})\right] \times \left[\hat{\sigma}_0 + \frac{\alpha_s(m_{ll}^2)}{2\pi}\hat{\sigma}_1 + ...\right] \quad (2.33)$$

and the corresponding NLO differential cross-section to $\mathcal{O}(\alpha_s)$ in the Modified Minimal Subtraction ($\overline{\text{MS}}$) [12] scheme with renormalization scale $\mu^2 = m_{ll}^2$ is given by [19]

$$\begin{aligned}\left(\frac{d\sigma}{dm_{ll}}\right)_{NLO} &= N_c C_{q\bar{q}} \frac{8\pi\alpha^2}{3m_{ll}^3}\tau \int_0^1 dx_1 dx_2 dz \delta(x_1 x_2 z - \tau) \\ &\times \left[\sum_q e_q^2 \left[f_{q/A}(x_1, m_{ll}^2) f_{\bar{q}/B}(x_2, m_{ll}^2) + (q \leftrightarrow \bar{q})\right]\right. \\ &\times \left(\delta(1-z) + \frac{\alpha_s(m_{ll}^2)}{2\pi} D_q(z)\right) \\ &+ \sum_q e_q^2 \left[f_{g/A}(x_1, m_{ll}^2)\left(f_{q/B}(x_2, m_{ll}^2) + f_{\bar{q}/B}(x_2, m_{ll}^2)\right) + (q, \bar{q} \leftrightarrow g)\right] \\ &\left.\times \frac{\alpha_s(m_{ll}^2)}{2\pi} D_g(z)\right] \end{aligned} \quad (2.34)$$

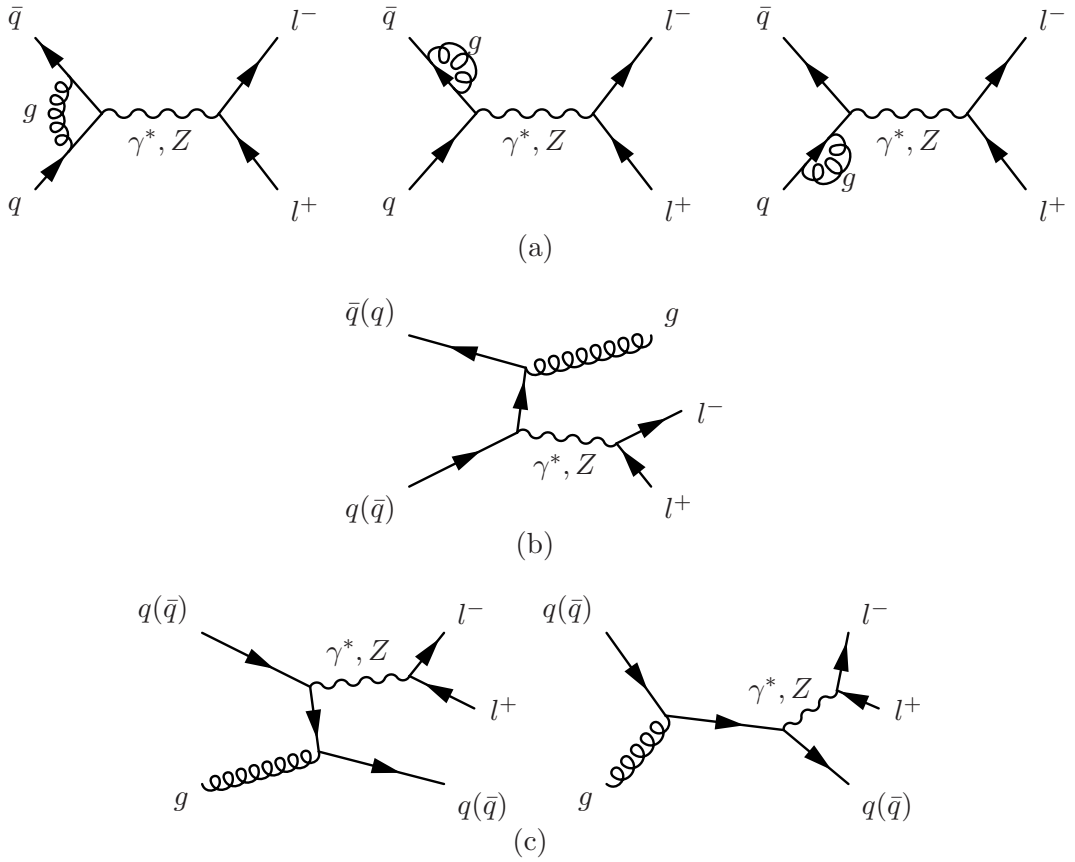

Figure 2.4: Feynman diagrams for corrections to the lowest order Drell-Yan process.

where the functions $D_q(z)$ and $D_g(z)$ are

$$D_q(z) = C_F \left[4(1+z^2) \left(\frac{\ln(1-z)}{1-z} \right)_+ - 2\frac{1+z^2}{1-z} \ln z + \delta(1-z) \left(\frac{2\pi^2}{3} - 8 \right) \right] \quad (2.35)$$

$$D_g(z) = T_R \left[\left(z^2 + (1-z)^2 \right) \ln \frac{(1-z)^2}{z} + \frac{1}{2} + 3z - \frac{7}{2} z^2 \right] . \quad (2.36)$$

The K-factor for the lowest order DY cross-section can be approximated as [18]

$$K = 1 + \frac{\alpha_s(m_{ll}^2)}{2\pi} \frac{4}{3} \left(1 + \frac{4}{3}\pi^2 \right) . \quad (2.37)$$

2.3 Backgrounds to the Drell-Yan process

There are several physics processes that may occur in pp collisions that will produce a two (or more) electron final state or fake a DY-like signature in the detector. All such processes will be considered background. There are a number of background processes to DY, for example: inclusive jets, $t\bar{t}$, $W^{\pm}Z$, $W^{\pm}W^{\pm}$, ZZ and $\tau^{+}\tau^{-}$ events. Expected LO production cross sections of these processes are given in [21] and references therein. In order to set the scale for the DY signal, the cross-section for DY pairs in the invariant mass range between 10 GeV $\leq m_{ee} \leq$ 110 GeV is about 7.8 nb.

Jets typically produce hadronic showers that leave different signatures in the detector than that of electrons. However, hadronic showers may contain electrons, but also there are substantial amounts of EM energy deposited in the calorimeter that may mimic electrons. Although the probability of inclusive jets faking at least two electrons is quite low, the cross-section of inclusive jet production at the LHC is about 70×10^{6} nb which is enormously higher than DY, hence making inclusive jet events a significant background source to the DY. In contrast to the previous experiments, a non-negligible amount of inclusive jet events will originate from heavy flavour quarks b and c at the LHC. A hadron from a heavy quark will decay leptonically about 10% of the time, producing an electron and another hadron or less frequently even two electrons. Therefore, there will be real electrons as well as fakes in the inclusive jet events making them the dominant background. There are ways of identifying fake electrons coming from inclusive jet events. For example, they generally will leave hadronic signatures in the detector in the form of some energy

leakage into the hadronic calorimeters. A real electron from an inclusive jet event will not be isolated like a DY electron as it will have a close-by jet due to the other hadron coming from the decay of the heavy flavour quark. Hence, these non-isolated background electrons can also be distinguished from DY electrons.

The pair production of $t\bar{t}$ quarks is quite large at the LHC and the probability of such pairs decaying leptonically, $t\bar{t} \to W^+W^-b\bar{b} \to e^+\nu_e e^-\bar{\nu}_e b\bar{b}$, is significant to be a background to the DY process. The LO cross-section at the LHC for $t\bar{t}$ production is 0.59 nb. The probability of both t quarks in a pair decaying leptonically is about 1%. Due to the missing transverse energy (neutrinos) content of these processes, it is sometimes possible to separate them from the DY processes. It is also possible for $t\bar{t}$ events to have only one or none of the W bosons decaying leptonically and still produce a DY-like signature with one or both of the b quarks decaying leptonically, similarly to the inclusive jet events above.

Di-boson events such as $W^\pm W^\pm$, $W^\pm Z$, and ZZ decaying leptonically (e.q. $W^\pm Z \to e^\pm\bar{\nu}_e e^+e^-$) will produce final states with two or more electrons faking the DY process. Given the relatively low cross-section of di-boson production (0.070 nb for $W^\pm W^\pm$, 0.026 nb for $W^\pm Z$ and 0.011 nb for ZZ) compared to DY and the low probability (about 1%) of both bosons decaying leptonically, di-boson events are not expected to contribute significantly to the DY background.

The production of a $\tau^+\tau^-$ pair from a decay of γ^*/Z is another DY process with equal probability to e^+e^-. Hence the leptonic decay of both taus, $\tau^+\tau^- \to e^+\nu_e\bar{\nu}_\tau e^-\bar{\nu}_e\nu_\tau$, though only about a 3% probability, will be a considerable background as well.

Chapter 3

Experimental setup

The LHC [22] is installed at CERN near Geneva, Switzerland in an existing circular tunnel that was built for the now completed LEP [23] physics program. ATLAS [24] along with CMS [25] is one of two general purpose detectors that are built at the LHC.

In this chapter, the design and performance requirements of the LHC machine and of the ATLAS detector are presented with particular focus on the detector components most relevant for this work.

3.1 The Large Hadron Collider

The LHC consists of two beam pipes that contain counter circulating proton beams located in an underground tunnel approximately 27 km in circumference. Super-conducting magnets with a magnetic field of 8.5 Tesla keep the protons in a circular path. Two beams of protons at 450 GeV will be injected into the LHC rings from the Super Proton Synchrotron (SPS) and accelerated up to 7 TeV each before being brought into head-on collision. Hence, the LHC will provide proton-proton (pp) collisions at a centre of mass energy of 14 TeV [26] making the LHC the highest energy accelerator and collider ever built. The schematic

layout of the LHC is shown in figure 3.1.

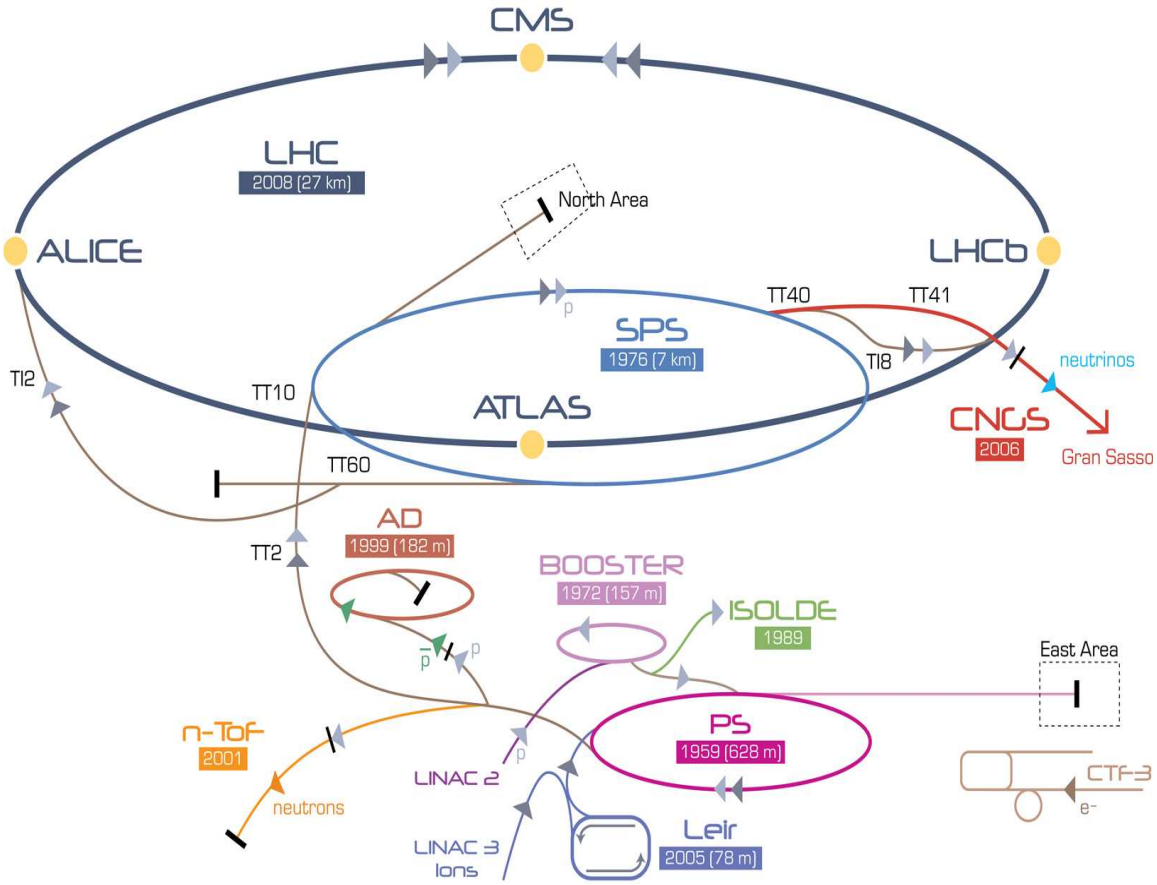

Figure 3.1: Schematic layout of the LHC complex [27].

There are three main reasons for using two beams of protons in the collider instead of antiprotons and protons or electrons and positrons. First, protons are easier to produce compared to antiprotons whilst still having approximately the same total cross-section for interacting. Second, there is much less synchrotron radiation loss for protons compared to electrons of the same energy. Third, hadrons (i.e. composite particles) will provide a broad spectrum of constituent collisions compared to electrons (i.e. point-like particles) which is

good for surveying many energies at once, but it makes it difficult to know the exact energy of the constituent collisions.

As mentioned in section 1.2, the primary purpose of the LHC is to find out whether the Higgs boson exists, and therefore the LHC is designed to provide high enough energy to produce the Higgs boson over its full theoretically possible mass range. However, the probability of producing the Higgs boson or any new physics is predicted to be very small. Therefore, the LHC is also designed to run at a very high luminosity, $L = 10^{34}$ cm^{-2}s^{-1}. The rate of pp interactions at a given luminosity, L, can be calculated from $R = L\sigma$ where σ is the cross-section of a pp interaction. In order to accomplish such high luminosity, the protons need to be stacked in bunches very close to each other. The result is a bunch separation and hence crossing time of 25 ns. Taking into account the probability that two protons will interact (i.e. total cross-section), this will mean an average of 22 events occurring per bunch crossing or a signal rate of 7×10^8 Hz at full design luminosity. An event, in this case, is defined as an inelastic interaction of two protons that produces a detectable signal in the ATLAS detector. These events can be categorized as hard and soft interactions. Hard interactions are those high-momentum-transfer physics processes of interest such as the production of the Higgs or Z bosons. Soft interactions are long range or low-momentum-transfer processes which are also called minimum bias events. A large fraction of pp collisions at the LHC will be minimum bias events.

Due to the high rate of interactions, the detectors at the LHC are required to be radiation hard, have very fast and complex read-out electronics systems, and hard inter-

action events will need to be carefully selected with a sophisticated trigger system. Fast read-out is crucial to avoid measuring events overlapping from different bunch crossings at the same time. Such overlap is considered as pileup to the physics event of interest. The pileup due to minimum bias events from the same bunch crossing cannot be avoided. The effect of pileup whether it is from the same bunch crossing or different bunch crossings will vary depending on the intended physics measurement.

3.2 The ATLAS detector

The ATLAS detector is designed to be capable of withstanding the high radiation environment produced by the LHC for several years while providing fast read-out and selection of the interesting physics events. It consists of several subdetectors, as shown in figure 3.2, designed to achieve the full physics program envisioned.

3.2.1 Coordinate system

The ATLAS coordinate system is used to describe the direction of particles from the collision centre as well as the orientation of the detector components. It is a spherical polar coordinate system with its origin being the interaction point of the proton beams. The positive z direction lies along the beam axis and forms a right handed coordinate system with the x-axis pointing towards the center of the LHC ring, and the y-axis pointing upwards. The polar angle, θ, is measured from the z-axis. In practice, the polar angle is expressed in terms of pseudorapidity, η, and is defined as $\eta = -\ln\left(\tan\frac{\theta}{2}\right)$. The use of η simplifies the calculation of cross-sections and other observables for the case when the hard scatter centre

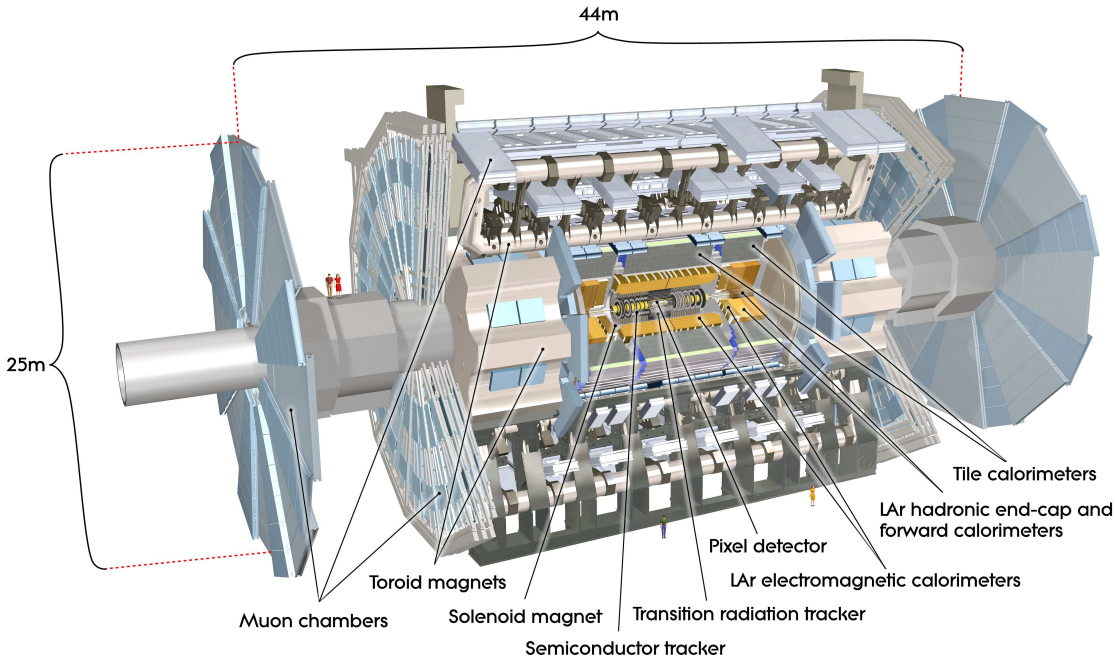

Figure 3.2: Geometrical layout of the ATLAS detector. The detector is about 44 m in length, 25 m in height and weighs 7000 tons. The different parts of the detector labeled in the diagram are described in the text.

of mass moves in the lab frame as is the case for pp collisions at the LHC. The detector components are segmented in equal η intervals wherever possible as the number of particles from minimum bias events will approximately be the same per interval. The transverse components of the physical quantities such as momentum and energy are defined in the x-y plane transverse to the direction of the proton beams.

3.2.2 Tracking

The inner detector [28] is designed to measure the direction, momentum, and sign of the electrically charged particles produced in each proton-proton collision. It will provide some information on the identity of particles as well. The inner detector is composed of a high

resolution pixel detector and a semiconductor tracker (SCT) surrounding the collision origin, and a lower resolution transition radiation tracker (TRT) surrounding the SCT. The inner detector covers the pseudorapidity region $|\eta| \leq 2.5$. The set of signals, called hits, left by a charged particle as it traverses the detectors is called a track. Charged particle tracks are bent by a 2 Tesla magnetic field generated by a super-conducting solenoidal magnet enclosing the inner detector. Figure 3.3 shows a cut-away view of the inner detector.

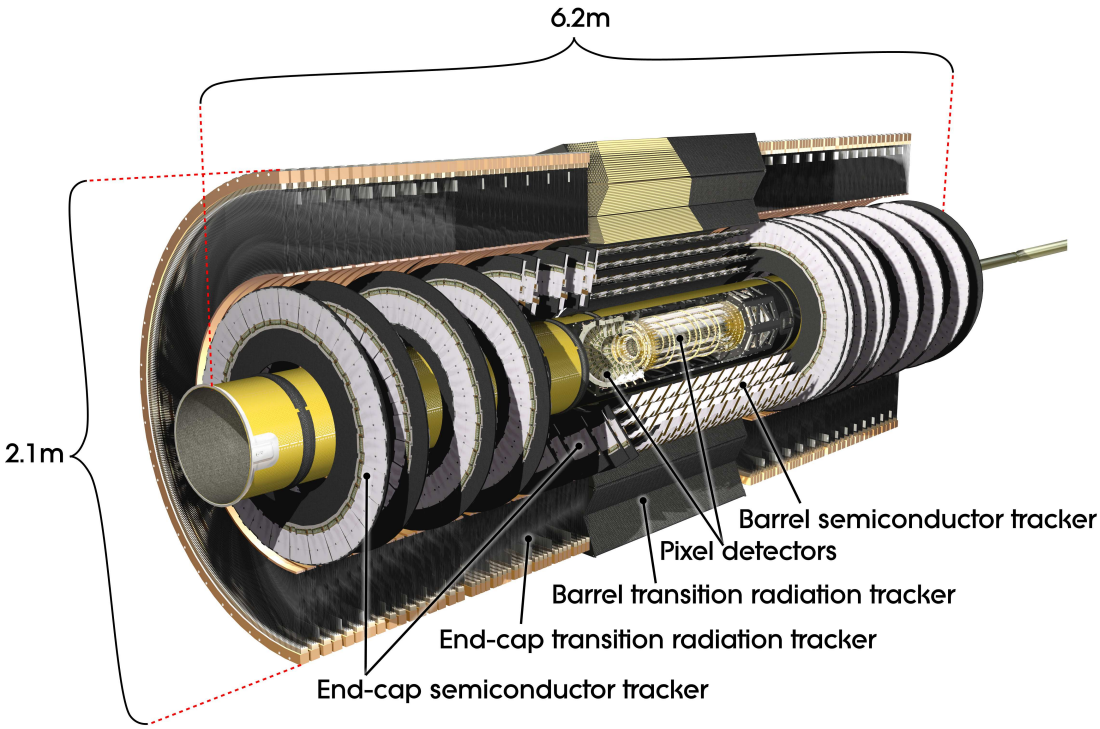

Figure 3.3: Geometrical layout of the ATLAS inner detector.

Pixel detector

The pixel detector is the innermost layer of the inner detector. It consists of three concentric cylindrical barrel layers around the beam axis and three disks perpendicular to the beam

axis on each endcap side. Barrel layers are located at radii of 5 cm, 9 cm and 12 cm, while the inner and outer radii of the endcap disks are at 9 cm and 15 cm respectively. The minimum pixel size is 50 μm in $r-\phi$ and 400 μm in z. With about 80 million channels, the pixel detector will provide a precise measurement of the momentum of charged particles and will largely determine the secondary vertices of short-lived particles such as B hadrons. High granularity of the pixel detector is also essential for pattern recognition in order to identify each charged track among hundreds of others. The closest pixel layer to the interaction point, called the vertexing-layer, will have to be replaced after three years of operation at high luminosity as it will not survive the high radiation. The intrinsic resolution of the pixel detector is 10 μm in $r-\phi$ and 115 μm in z.

Semiconductor tracker

The SCT uses silicon microstrip technology for tracking charged particles. It has four cylindrical double layers of strips in the barrel and nine disks on each endcap side. In the barrel, each layer has one set of strips parallel to the beam axis and the other set offset by a 40 mrad angle in order to measure both coordinates. The layers are located at radii 30 cm, 37 cm, 44 cm and 51 cm. In the endcap, each disk has one set of strips arranged radially and the other at a 40 mrad angle similar to the barrel layers. The inner radius of the disks is 27 cm, and the outer radius is 56 cm. The intrinsic resolution of the SCT layers is 17 μm in $r-\phi$ and 580 μm in z. The SCT contributes to the precise measurement of momentum and pattern recognition of hits that belong to a track.

Transition radiation tracker

The TRT consists of polyimide drift tubes, called straws, each with a 4 mm diameter, that provide up to 36 charged-track hits for further tracking information in ϕ that can contribute to the momentum measurement. The TRT covers the pseudorapidity region $|\eta| \leq 2.0$ and has an inner radius of 56 cm and an outer radius of 106 cm. The intrinsic resolution of the TRT straws is 130 μm. The straws are interleaved with polypropylene fibers in the barrel and foils in the endcap that will cause emission of photons when charged particles cross the TRT. These photons are called transition radiation and have energies in the X-ray range, about 1 keV. The number of photons emitted is proportional to the Lorentz factor, $\gamma = E/m$ where E is the energy and m is the mass of the charged particle. Therefore, at a given energy, lighter particles like electrons with higher γ values can be distinguished from those heavier particles such as hadrons with lower γ values. The straws are filled with a xenon gas mixture in order to detect this transition radiation.

3.2.3 Calorimetry

The calorimetry system surrounds the solenoidal magnet and the inner detector, and covers the pseudorapidity region $|\eta| \leq 4.9$. It measures the energy and the position of both charged and neutral particles. The ATLAS calorimetry system employs liquid argon (LAr) sampling calorimetry [29] and scintillating tile calorimetry [30] technologies. A brief discussion of sampling calorimetry as well as a detailed description of interactions of particles with detector materials can be found in [31]. LAr is used in the calorimeters close to the beam axis mainly because it has good energy and spatial resolution while it is radiation hard and

easy to calibrate. The calorimeters are divided into an inner part optimized to measure electrons referred to as an electromagnetic (EM) calorimeter and outer part optimized to detect hadrons. All read-out towers of the calorimeters point towards the collision origin. Figure 3.4 shows a cut-away view of the ATLAS calorimetry system.

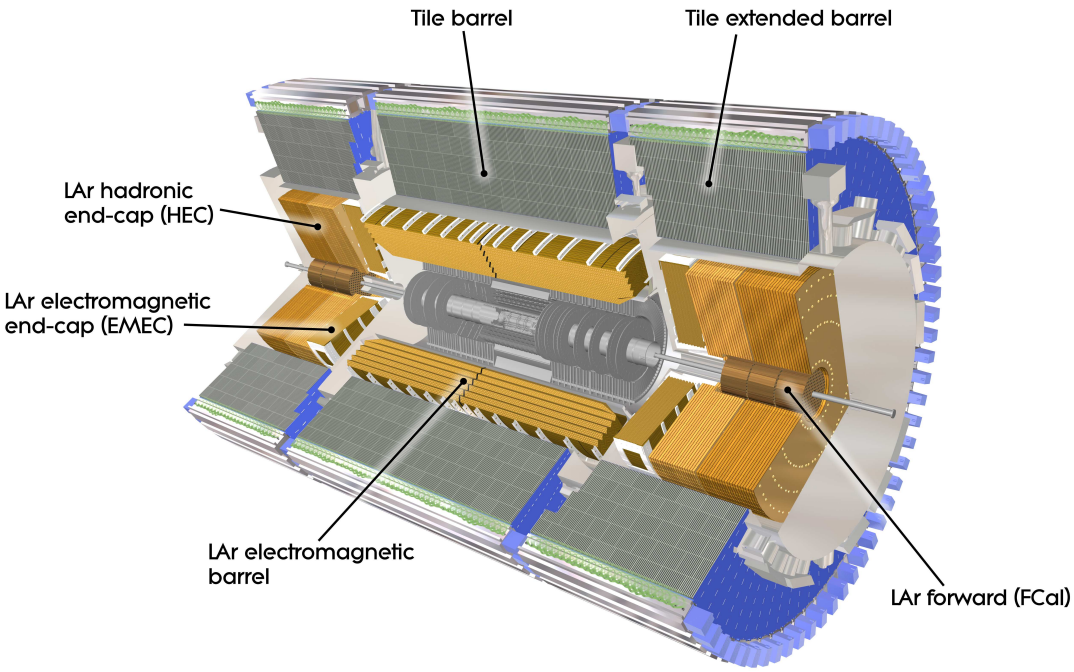

Figure 3.4: Geometrical layout of the ATLAS calorimetry system.

Electromagnetic calorimeter

The electromagnetic calorimeters consist of two identical half-barrels with a 6 mm gap, called the crack, in between that cover $|\eta| \leq 1.475$ and two endcaps each of which are made up of two coaxial, inner and outer, wheels that cover $1.375 \leq |\eta| \leq 3.2$ and have a 3 mm gap in between. There is also a small crack at $|\eta \approx 1.45|$ in the transition region between barrel and endcap EM calorimeters that is used to route cables and services from the inner

detector. The EM calorimeters use lead (Pb) absorbers arranged in a unique accordion shape that provides excellent hermiticity in ϕ for each section. The read-out electrodes are also accordion shaped and made of three layers of copper (Cu) separated by insulating polyimide sheets. They are segmented in three longitudinal layers in depth in the barrel and outer wheels of the endcaps, and two longitudinal layers in the inner wheels of the endcaps. The absorbers and electrodes are arranged axially with accordion waves running radially in the barrel, whereas the arrangement is radial with the waves running parallel to the beam axis in the endcaps. The folding angles and amplitudes of the accordion waves are varied when necessary to keep the combined thickness of LAr and absorber, that would be traversed by particles, constant in η in order to achieve a uniform response.

The EM calorimeters are more than 22 radiation lengths (X_0) thick for the barrel, the distance over which an incident electron energy is reduced by a factor of $1/e$ due to bremsstrahlung only, and 24 X_0 in the endcaps. The EM calorimeters are segmented in three longitudinal layers for $|\eta| \leq 2.5$ and are preceded by a presampler, an active layer of LAr, in the region $|\eta| \leq 1.8$ to compensate for the loss of energy of electrons and photons due to dead material, up to 4 X_0, in front of the EM calorimeters. The presampler has a granularity of $\Delta\eta \times \Delta\phi = 0.025 \times 0.1$. The first layer, layer-1, of the EM calorimeters has a granularity of 0.0031×0.1 where the very small segmentation in η allows for separation of photons and pions as well as providing a precise position measurement. The second layer, layer-2, has a granularity of 0.025×0.025, and combined with the fine granularity of layer-1 it provides a very good measurement of the direction of neutral particles such as photons

that do not leave a track in the inner detector. The third layer, layer-3, has a granularity of 0.05×0.025. The longitudinal thicknesses of these three layers are about 4 X_0, 16 X_0 and 4 X_0, respectively. Hence, most of the EM energy from electrons or photons is contained in layer-2.

The energy resolution of an EM sampling calorimeter can be expressed as

$$\frac{\sigma(E)}{E} = \frac{a}{\sqrt{E}} \oplus \frac{b}{E} \oplus c \tag{3.1}$$

where a is the sampling term coefficient which depends on the intrinsic fluctuations of the EM shower and the sampling fluctuations, b is the coefficient of a term proportional to the electronic noise, and c is the constant term reflecting local non-uniformities of the response of the calorimeter due to the mechanical imperfections of the calorimeter and incomplete shower containment. The terms are added in quadrature. The expected performance of the ATLAS EM calorimeters in terms of energy resolution is $10\%\sqrt{\text{GeV}}$ in the sampling term coefficient, 200 MeV in the noise coefficient and 0.7% in the constant term. The angular resolution is estimated to be in the range $50 - 60$ mrad$/\sqrt{E[\text{GeV}]}$.

Hadronic calorimeters

The hadronic calorimeters are placed behind the EM calorimeters. In the central and extended barrel regions, $|\eta| \leq 1.7$, iron (Fe) absorbers and scintillating plastic tiles are arranged to point towards the collision centre. In the endcap region, LAr is the active material instead of scintillating plastic tiles. Cu plate absorbers are used in the region $1.5 \leq |\eta| \leq 3.2$, while the very forward calorimeters covering the region $3.1 \leq |\eta| \leq 4.9$ have an EM component with Cu absorbers and hadronic component with tungsten (W)

absorbers. The longitudinal depth of the hadronic calorimeters is approximately 10 nuclear interaction lengths (λ) which is sufficient enough to contain any high energy jet of hadrons.

3.2.4 Muon spectrometer

The muon spectrometer [32] surrounds all of the other detectors and provides standalone identification and measurement of the momentum of muons specifically. The information from the muon spectrometer can be combined with the inner detector to further improve the precision of the muon momentum measurement. It is the outermost layer of the ATLAS detector because muons will generally go thorough the other detectors with very low energy loss. The muon trajectory is deflected by a 4 Tesla magnetic field provided by air-core toroidal magnets. The open structure minimizes multiple scattering and hence improves the muon momentum resolution.

3.2.5 Trigger system

The very high luminosity collisions at the LHC will provide an event rate of approximately 1 GHz at the design luminosity. ATLAS will record about 1.5 megabytes of data per event on average. This would mean 1.5 petabytes of data would have to be recorded every second in ATLAS in order to store data from every collision. This is impossible with the current technology in electronics systems and storage elements. In addition, only a small fraction of these events would actually contain hard interaction (high momentum transfer) processes that are of physics interest. Therefore, a three level trigger system is designed for ATLAS to determine whether an event shall be recorded while reducing the event rate several orders of magnitude in order to match the capacity of the data acquisition (DAQ) system.

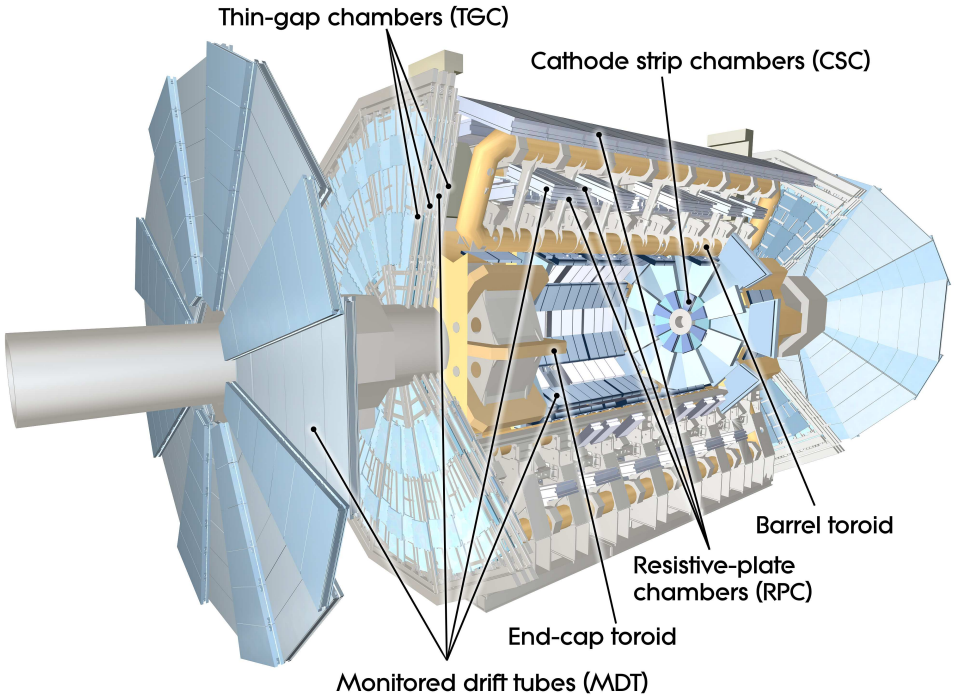

Figure 3.5: Geometrical layout of the ATLAS muon system.

The ATLAS trigger system is composed of hardware based level-1 (LVL1) and software based level-2 (LVL2) and event filter (EF) triggers. Each successive level of trigger has progressively more complex algorithms to determine physics signatures of interest and therefore requires more time, known as latency, to reach a decision. A schematic diagram of the ATLAS trigger system is presented in figure 3.6.

The LVL1 trigger only uses information from the calorimeters and muon spectrometer and reduces the data rate from 1 GHz to 75 kHz with a latency of about 2 μs [33]. For each selected event, the LVL1 trigger also sends information to the Region of Interest Builder (RoIB) regarding where in the calorimeters and/or the muon spectrometer, the interesting physics object (e.g electron, photon, muon, etc) is identified so that the LVL2 can

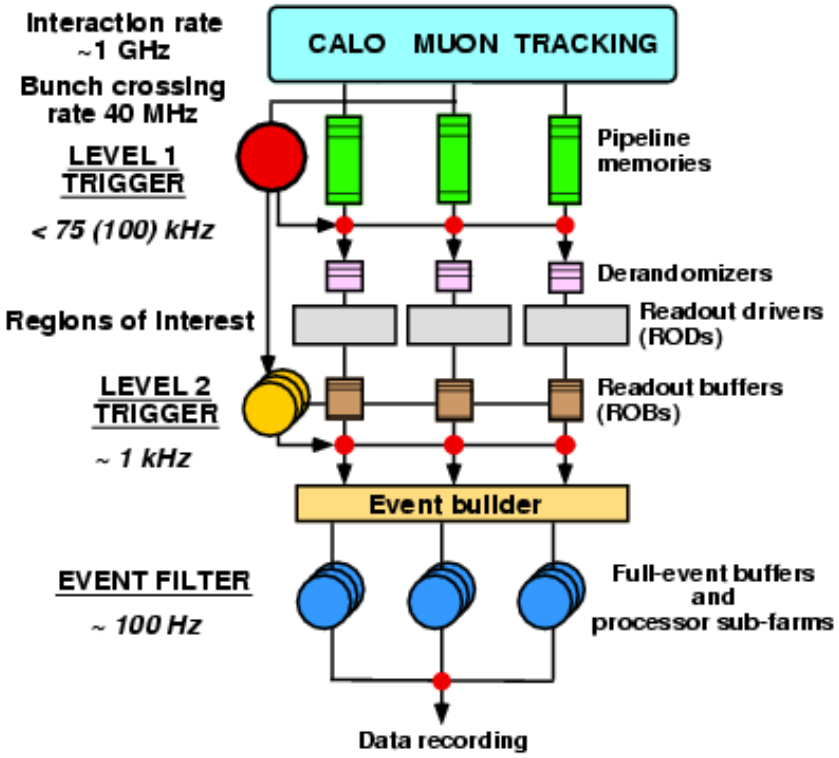

Figure 3.6: Schematic diagram of the ATLAS trigger system.

make fast decisions using only information from the RoIs rather than looking at all parts of the calorimeters and the muon spectrometer.

The LVL2 and the EF triggers together are also known as the High Level Trigger (HLT) [34]. The LVL2 trigger can also make use of the other sub-detectors, the inner detector for instance, depending on the physics object being identified. The LVL2 trigger reduces the data rate from 75 kHz to about 1 kHz with a latency of up to 10 ms.

The final selection of an interesting physics event that is to be recorded and used for subsequent detailed offline analyses is made by the EF. The latency at the EF is about 1 s, and hence several processors are used in parallel in order to produce a data rate of 100 Hz.

3.2.6 Observables

The data that will be recorded by the ATLAS detector will not actually be coming directly from particles of interest such as the Higgs boson but rather from their decay products that in general will be photons, charged leptons, jets of hadrons and neutrinos. Each of these particles will interact differently with various parts of the detector leaving distinct patterns known as signatures with the exception of neutrinos that are not directly detected. Photons will deposit almost all of their energy in the EM calorimeters due to EM interactions with the medium as will electrons. However, electrons also leave tracks in the inner detector and leave a distinct signature in the TRT as well. Jets of hadrons will reach further into the detector depositing energy in both EM and hadronic calorimeters. Muons will exit the entire detector leaving tracks in both the inner detector and the muon spectrometers whilst depositing very little energy in the calorimeters. The existence of neutrinos in the final state can be deduced from any missing transverse energy as the total momentum of the final state has to be zero. This is known as missing energy or more typically missing transverse energy because of the possibility of particles to escape down the beam pipe. It is called energy rather than momentum because it is usually measured with the calorimetry system.

The ATLAS detector is designed to precisely measure the energy, vector momentum, and sign of the particle charge for all of the final state decay particles sufficiently well that the objectives set by the physics program are met.

Chapter 4

The ATLAS Monte Carlo

Particle physics experiments are conducted in order to test the predictions of theories. Due to the complex geometry of the particle detectors and hence a lack of an analytical expression for the detector response and sometimes the theory, Monte Carlo (MC) methods are used to simulate the theory and detector response. The MC uses the same framework through which the experimental data are processed so that a direct comparison can be made. Since the theory is mostly known at the parton level, MC is also used to fragment partons to leptons and jets containing composite particles (e.g. pions) made of partons.

The theoretical predictions coming from the MC methods are important to set requirements and specifications for resolutions etc, when designing a detector and a trigger system that will recognize the wanted signal. They are also needed in order to study detector acceptances, to estimate rates, to devise a means for separating a signal like DY from the background processes and hence to estimate the feasibility of a potential measurement. Finally, the MC will be used to compare theory directly to experimental data.

In this chapter, a brief overview of the ATLAS MC production chain of a physics

event is given in three basic stages: generation, simulation, and reconstruction.

4.1 Generation

PYTHIA [35] and HERWIG [36] are multi-purpose event generators at LO that are used to simulate all stages of a pp collision and output a list of particles from the initial, intermediate and final states of the physics process along with their associated four-momenta.

The generation of an event in a pp collision can be summarized as follows:

- A parton from one proton collides with a parton from the other proton in a so-called hard subprocess and produces two final state partons. Initial state partons may form a short lived resonance, like γ^*/Z in the case of DY, which then decays into fermions.

- Initial state partons may radiate gluons or photons, referred to as initial state radiation (ISR), before the collision. Gluon radiation is called QCD radiation while photon radiation is referred to as QED radiation.

- Final state partons may radiate gluons, and partons and charged leptons may radiate photons collectively referred to as final state radiation (FSR). In ATLAS, QED radiation is modeled by PHOTOS [37].

- Final state partons undergo hadronization to form jets of hadrons. The hadrons may be unstable and hence decay further.

- The remaining partons from each proton now carry net colour due to the colour-charge taken away by the hard interaction partons and hence also will undergo hadronization,

and the hadrons produced will decay further if they are unstable. These are called the underlying event.

- There may be other parton-parton interactions between the remaining partons from each proton in the pp collision. These are also considered as part of the underlying event. For HERWIG and HERWIG-based generators, JIMMY [38] normally is used for underlying event generation in ATLAS.

CTEQ PDFs are chosen as the default for both PYTHIA and HERWIG in ATLAS. A schematic diagram of a MC event is shown in figure 4.1.

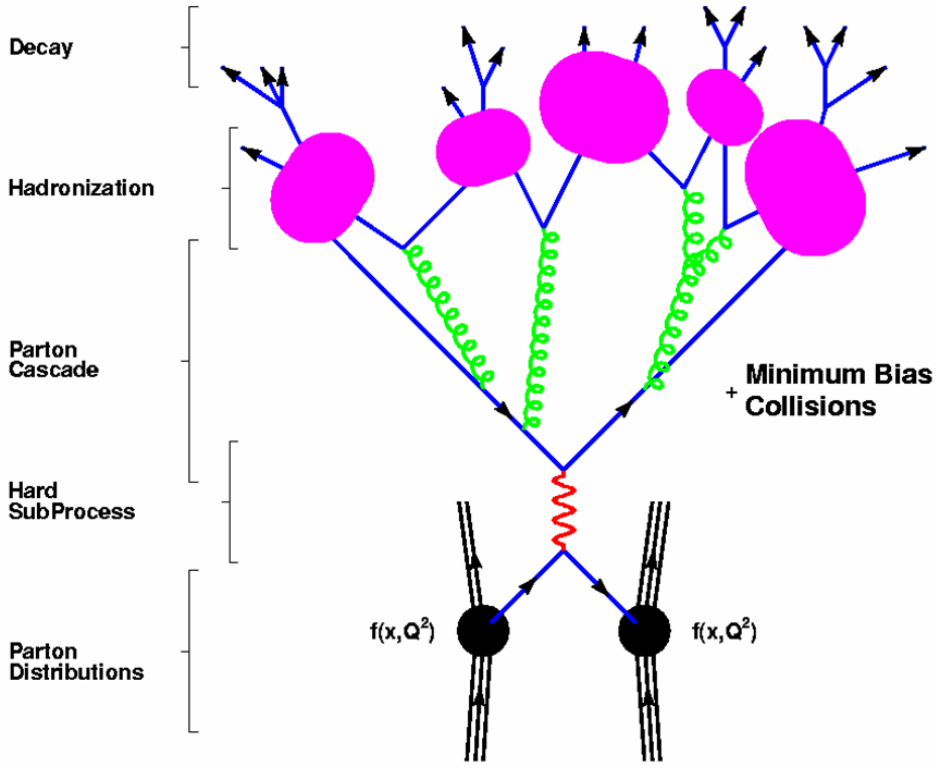

Figure 4.1: Schematic diagram of a MC event [39].

PYTHIA and HERWIG differ mainly in the way the hadronization is modeled. PYTHIA uses a string model in which a gluon produces a $q\bar{q}$ pair that are moving apart from each other with a string attached between them to denote the colour-field between the pair. As the pair move apart, the potential energy in the string increases until reaching enough energy to break-up and produce a $q\bar{q}$ pair. The string carries the colour information from the initial quark (antiquark) to the new antiquark (quark), such that a colour-singlet hadron can be formed. The process continues until all colour carrying partons form hadrons. HERWIG describes hadronization with a cluster model in which gluons are split into $q\bar{q}$ pairs that are grouped to form colour-singlet clusters that then decay into hadrons.

4.2 Simulation

GEANT [40] is a simulation program used to describe the interactions of the particles from the event generators with the elements of the ATLAS detector.

Each generated particle is followed as it traverses through the detector in the direction of its momentum vector and allowed to interact with the matter. In GEANT, the unit distance traveled by the particle in the detector is called a step. A step is small enough that only one type of detector material is traversed making it easier to model the interactions between the particle and the material. After each step, a data element called a hit is recorded that contains information about the type of the detector element traversed, the position and the energy deposited in that element. The same procedure is also applied for those particles produced through the interactions of the generated particles with the detector material, and hits for those particles are recorded as well.

The hits produced from the detector simulation are digitized in 25 ns bins just as the real data are collected by the ADCs that digitize the signal every 25 ns. The effects resulting from the characteristics of the detector and its electronics such as light attenuation and electronic noise are applied to simulate actual detector response. The digitized outputs are called Raw Data Objects (RDOs) that are the same format as the real data so that it can be used in the same reconstruction procedure as data thereby allowing for direct comparison.

At the high luminosities expected at the LHC, there are multiple events at each beam crossing. The superposition of multiple signals coming from the same beam crossing or the beam crossings nearby is called pile-up and the ATLAS simulation has an additional processing stage besides GEANT to add pile-up effects to the event being simulated.

4.3 Reconstruction

The RDOs are fed into the reconstruction software that builds higher level objects for final analysis. In ATLAS, the output of the reconstruction has two main types: the Event Summary Data (ESD) and Analysis Object Data (AOD).

The reconstruction stage includes several algorithms some of which are for sub-detector specific reconstruction like tracks in the inner detector and some combine information from various detector components for optimum information such as the four-momentum of a particle. The ESD contains all detector specific and combined reconstruction data such as calorimeter cell energies and positions, clusters of cells, tracks, calibration and initial particle identification (e.g. EM object). The AOD contains only a small sub-set of the ESD

data in the form of analysis objects such as electrons, photons, muons, jets and missing transverse energy. Final analyses are to be done on the AOD, since the ESD is of too large a size to be distributed to all physicists. However, the ESD is a key component of the fast re-reconstruction of data and reproduction of the AOD without having to go back to the RDO that will be necessary in the case, for example, of applying new calibration or corrections to the data.

In addition to the detailed MC simulation described above, there is a fast simulation program, designed for ATLAS, known as ATLFAST [41]. This program takes input from event generators, applies calorimeter and tracking resolutions known from full simulation studies and outputs reconstructed physics objects. Essentially, ATLFAST combines simulation and reconstruction steps, saving on processing time at the expense of the fine-detailed geometry and response available from the full MC.

Chapter 5

Analysis method and event selection

Particles produced in the physics processes of interest are identified and measured through the characteristics of the signatures they leave in the detector due to interactions with the medium traversed.

In this chapter, simulated data samples used in this work are described, followed by a detailed explanation of the reconstruction and identification of an electron signature in the detector. Then, efficient electron pair selection criteria that will distinguish Drell-Yan electrons from other background electrons are developed. Finally, inclusive jet background, which is the dominant background, is estimated and reduced.

5.1 Data samples

All data samples used in this work are based on the detailed simulation of the ATLAS detector response to the physics processes studied. Table 5.1 lists the data samples in this dissertation including their cross-sections, and number of events simulated. The data samples are scaled to correspond to an assumed integrated luminosity of 100 pb^{-1} for the

rest of this dissertation unless stated otherwise.

Data sample	σ [pb]	ϵ_{filter}	N_{event}	$\mathcal{L}$ [pb^{-1}]
Signal, $\gamma^*/Z \to e^+e^-$	3.53×10^5	0.0102	227666	63
Inclusive jets	7.0×10^{10}	0.0584	2478450	6.1×10^{-4}
$t\bar{t}$	8.34×10^2	0.553	573700	1245
$Z \to \tau^+\tau^-$	1.64×10^3	0.15	49500	201
$W^+W^- \to e^+\nu_e e^-\bar{\nu}_e$	1.275	1.0	20000	1.6×10^4
$ZZ \to l^+l^-l^+l^-$	14.8	1.0	48000	3.2×10^4
$W^+Z \to l^+\nu_l l^+l^-$	29.4	1.0	49950	1.7×10^4
$Z \to e^+e^-$	1.67×10^3	0.846	346450	245
$\Upsilon \to e^+e^-$	1.68×10^5	0.327	143000	2.6
$J/\psi \to e^+e^-$	5.37×10^6	0.027	285000	2.0

Table 5.1: Simulated Drell-Yan signal and background data samples. The Z, Υ and J/ψ samples used for efficiency calculations that are presented in chapter 6 are also listed. The cross-sections for di-boson and $t\bar{t}$ samples are calculated to NLO while the rest are given in LO. Descriptions of the filters are provided in the text.

The Drell-Yan signal sample is generated with PYTHIA in the parton pair invariant mass range 1 GeV $< \sqrt{\hat{s}} <$ 60 GeV. It takes approximately 15 minutes to produce a physics event through the ATLAS Monte Carlo chain. Much of the processing time is spent at the simulation step. Therefore, in order to save processing time and to minimize the statistical uncertainties, the signal events are pre-filtered at the generation level to select and simulate only those events with electrons in the kinematic range that correspond to electrons that can be measured taking into account the limitations of the ATLAS detector. This will be explained in more detail in the next sections. In this case, events with electrons of transverse momentum, p_{T}, greater than 3 GeV in the pseudorapidity range $|\eta| < 2.7$ are selected.

The inclusive jet sample is also generated with PYTHIA. The events are pre-filtered to select events with at least one jet of transverse energy, E_{T}, greater than 6 GeV within a

narrow window of $\Delta\eta \times \Delta\phi = 0.06 \times 0.06$ in the range $|\eta| < 2.7$. Such a jet is considered more likely to fake an electron signature in the detector.

The $t\bar{t}$ sample is generated using MC@NLO [42], a HERWIG based generator at NLO. Only the events with at least one lepton are simulated. Therefore, those $t\bar{t}$ events in which both W bosons decay hadronically are excluded as the likelihood of such a fully hadronic final state faking two electrons is negligibly small.

Di-boson samples are generated with MC@NLO as well. The W^+Z and ZZ samples are inclusive of all possible leptonic decays of W and Z bosons. The W^+W^- events only contain decays to electrons. Di-boson events are not pre-filtered as their cross-sections are relatively small, and hence samples with reasonable numbers of events could be produced.

The Drell-Yan resonances (Z, Υ and J/ψ) studied for the signal selection efficiency calculations shall be discussed in detail in chapter 6. They are generated with PYTHIA. The Υ and J/ψ events are pre-filtered to require both electrons to have $p_{\mathrm{T}} > 3$ GeV and to be in the range $|\eta| < 2.7$. Only one of the electrons is required to have $p_{\mathrm{T}} > 10$ GeV and $|\eta| < 2.7$ for the Z sample. The Z boson sample is generated for invariant masses $\sqrt{\hat{s}} > 60$ GeV.

5.2 Electron reconstruction

The ATLAS detector uses two of its components, namely the inner detector and calorimetry, to detect and measure electrons through their interactions with the detector elements [43]. Figure 5.1 shows a schematic view of a typical electron signature in the ATLAS detector.

An electron coming from the interaction point first goes through the inner detector.

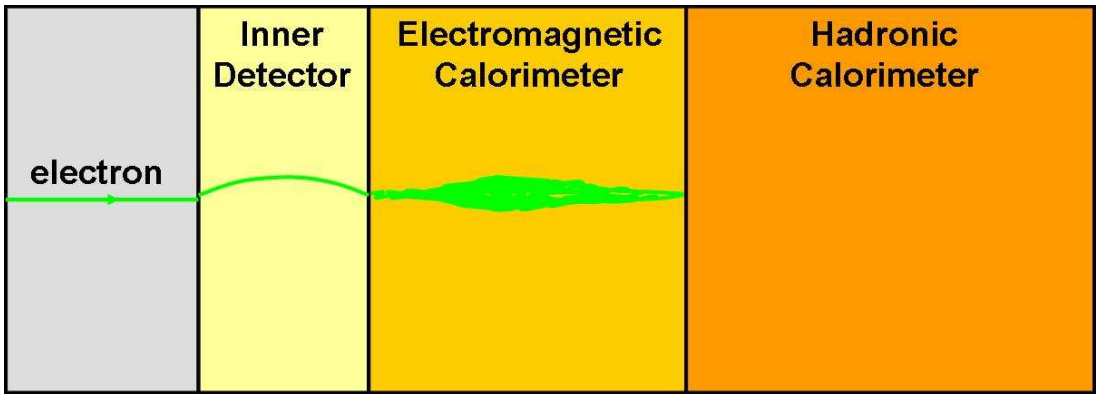

Figure 5.1: Schematic view of an electron signature in the ATLAS detector.

As the electron traverses the pixel detector and the SCT, like all charged particles it will produce electron-hole pairs in the silicon in the pixel detector and the SCT. In the case of the TRT, the electron and its transition radiation will ionize the gas. With the help of an electric field and electronics, currents induced by the liberated electrons in the silicon-based detectors and by the ionization electrons in the TRT are collected and read-out. Each small read-out component (e.g. a pixel), that has some charge in it, is said to be hit by the charged particle passing through. Following these hits from the interaction point out and connecting them together, the electron track can be reconstructed. The track will be curved due to the magnetic field generated by the solenoidal magnet system. A negatively charged track will curve towards the positive ϕ direction while a positively charged track will curve in the opposite direction. The radius of curvature will be inversely proportional to the magnitude of the electron momentum. Therefore, the measurement of momentum will be less precise, as the transverse momentum increases and the radius of curvature gets larger (i.e. straighter). In order to distinguish the pattern of the hits caused by the

electron from the tracks of all the other charged particles in the same event and from the minimum-bias pileup events, the ATLAS track reconstruction software makes use of all three sub-components of the inner detector whenever possible. The tracking algorithm also takes into account the possibility of a change of curvature as the electron may radiate a bremsstrahlung photon. Bremsstrahlung is more likely in the endcap region of the detector as the amount of detector material increases. Hence, it is more challenging to reconstruct an electron track in the endcap region.

The electron will next enter the electromagnetic calorimeter. The electron, depending on its energy, will undergo a series of interactions such as bremsstrahlung, ionization and excitation [31] within the calorimeter and hence lose energy. For DY electrons at the LHC, the most likely energy loss mechanism will be through bremsstrahlung radiation. The radiated photon depending on its energy will also have a series of interactions with the calorimeter medium including pair production, photoelectric effect and Compton scattering. The most likely interaction for a high energy photon is the pair production to an electron-positron pair. Consequently, the electron loses all of its energy via interactions with the calorimeter and a cascade of particles is produced through a succession of these interaction mechanisms. Each particle in the cascade will in turn go through similar interactions producing additional particles. All of these particles originated by the electron and by the particles that the electron has produced are referred to as an electromagnetic shower. All the particles in the EM shower will eventually lose all their energy in the calorimeter and the shower will stop. The calorimeter samples and collects the ionization current pro-

duced by the EM shower particles. The amount of ionization is directly proportional to the energy of the incident electron. Hence, in contrast to the inner detector, the electron energy is measured more precisely as the energy increases. The smallest read-out unit in the calorimeter is called a cell. As described in section 3.2.3, the ATLAS EM calorimeter has three longitudinal layers in the region $|\eta| < 2.5$ and a presampler at $|\eta| \leq 1.8$ with different granularity, in other words with various cell sizes. In layer-2 which is the thickest layer and hence contains most of the EM shower, the size of a cell is $\Delta\eta \times \Delta\phi = 0.025 \times 0.025$ or approximately 4 cm $\times$ 4 cm. In order to measure the electron energy, energies deposited in cells along the EM shower direction by the shower particles are summed. The collection of cells used to determine the electron energy is called an EM cluster. The default clustering algorithm at ATLAS that determines which cells belong to the same EM cluster uses a technique called a sliding window. In this technique, first a fixed size window is chosen. The window size is equivalent to 3×7 layer-2 cells in the $\eta - \phi$ plane for the barrel region of the EM calorimeter and 5×5 layer-2 cells in the endcap region. This window is then moved in each η and ϕ direction, and energies of cells from all EM calorimeter layers and the presampler inside the window are summed at every step until a local maximum is found. If the cluster E_{T} is greater than 3 GeV, the cluster is kept and the algorithm moves on to find other EM clusters if any. These clusters are then corrected for the effects such as the potential unsampled energy loss in the inner detector, lateral energy leakage due to fixed window size and possible energy leakage into the hadronic calorimeters for very high energy electrons.

An EM shower in the calorimeter can be initiated either by an electron or a photon. There are slight differences between a shower originating from an electron and a shower from a photon, mostly due to the difference between bremsstrahlung and pair production in that a photon on average will traverse a bit more than a radiation length of calorimeter medium before pair-producing electrons, while an electron will start radiating photons immediately upon interacting with the medium. However, this difference is quite small and is not enough to clearly distinguish an electron from a photon. Therefore, information from the inner detector has to be combined with the calorimeter information to accurately identify and measure electrons, since photons are charge neutral particles and do not leave traces in the inner detector. For an EM cluster to be considered as originating from an electron, a matching inner detector track must be found within a window of size $\Delta\eta \times \Delta\phi = 0.05 \times 0.1$ and with the ratio, E/p, of the cluster energy and the track momentum less than 10. When there are multiple matching tracks, the one with E/p closest the unity is chosen. Once the matching is done, the EM cluster and the associated track are considered as an electron. The charge and direction of the electron are considered the same as the track since the inner detector has better position resolution than the calorimeter. The energy of the electron will be that of the EM cluster as the calorimeter energy resolution is better than the inner detector.

5.3 Electron identification

A reconstructed electron candidate with a cluster of energy in the EM calorimeter and an associated track from the inner detector may not actually be an electron as there are other

charged particles like muons and hadrons that will leave tracks in the inner detector and deposit energy in the EM calorimeter. Even if the electron candidate is a real electron, it may be a decay product of a particle like a heavy flavour hadron and hence may not be an electron of interest. For example, a DY electron will be a decay product of a virtual photon or a Z boson and will be isolated such that there will not be a significant amount of energy deposit close-by due to an associated jet. Therefore further inspection of the characteristics of the electron candidate is necessary in order to determine the likelihood of it being a real isolated electron coming directly from the interaction point.

The ATLAS standard electron identification consists of three main sets of identification criteria based on properties of the EM shower, the track and the matching between the two. These identification categories are called loose, medium and tight respectively. The quantities used in the ATLAS standard electron identification are defined as follows:

ClusterEtaRange is the η position of the EM cluster calculated using layer-2 of the EM calorimeter. This selection ensures that the EM cluster is within the η range of the tracking system.

ClusterHadronicLeakage is the ratio of the transverse energy deposited in the first layer of the hadronic calorimeters to the transverse energy of the EM cluster. A DY electron will deposit all its energy in the EM calorimeter without leakage into the hadronic calorimeters, so this ratio should be close to zero for the Drell-Yan electrons.

ClusterMiddleEnergy is the energy deposited in the middle, layer-2, of the EM calorimeter in an area of 7×7 cells in $\eta - \phi$ plane.

ClusterMiddleEratio37 is the ratio of the energy deposited in an area of 3×7 cells to the energy deposited in a 7×7 cell area in the EM calorimeter layer-2. The ratio should be very close to unity for a DY electron since typically 95% of an EM shower is contained in a cylindrical area with a diameter of 3 EM layer-2 cells.

ClusterMiddleWidth is the energy weighted lateral size of the EM shower in layer-2. An EM shower will generally be much narrower than a hadronic shower.

ClusterStripsDeltaEmax2 is the ratio of the second largest energy deposit in the η direction in layer-1 of the EM calorimeter to the E_{T} of the EM cluster.

ClusterStripsDeltaE is the difference between the second largest energy deposit in the η direction in layer-1 and the minimal energy deposit between the largest and the second largest energy deposited cells in the η direction in layer-1. Along with the previous variable, this quantity is used to identify those electron fakes due to jets with one or more neutral pions decaying into photons. Showers produced by such jets often will have multiple maxima, and the very fine granularity of the EM calorimeter layer-1 allows for detection of multiple maxima and hence the possibility of separating this kind of fake from real electrons.

ClusterStripsWtot is the energy weighted lateral shower size determined in layer-1. The very small size of layer-1 cells in η allows for precise determination of the lateral size. A shower with smaller lateral size is more likely to be an EM shower rather than a hadronic shower.

ClusterStripsFracm is the ratio of the difference between the energy deposited in seven and three layer-1 cells to the energy deposited in three layer-1 cells in the η direction at the shower core.

ClusterStripsWeta1c is the energy weighted lateral shower size determined using only three layer-1 cells in the η direction at the shower core.

ClusterIsolation is the ratio of energy deposited around the EM cluster in an annular cone of half opening angle $\Delta R = \sqrt{\Delta\eta^2 + \Delta\phi^2} = 0.2$ to the energy of the EM cluster. The ratio should be very close to zero for a real electron.

TrackBlayer is the number of hits in the first layer, also called b-layer, of the pixel detector. An electron should leave at least one hit in this layer to ensure it comes directly from the interaction point.

TrackPixel is the number of hits in all layers of the pixel detector. A real electron should have at least one hit in the pixel detector.

TrackSi is the total number of hits in the pixel detector and the SCT. There should be at least nine hits for an electron.

TrackA0 is the transverse distance to the interaction point. It is also called the transverse impact parameter. The impact parameter for those background electrons that are decay products of heavy flavour hadrons should be bigger than DY electrons as these background electrons are not coming directly from the interaction point.

TrackMatchEta is the difference between the cluster η position calculated using the EM calorimeter layer-1 cells and the track η position extrapolated to layer-1.

TrackMatchPhi is the difference between the cluster ϕ position calculated using the EM calorimeter layer-2 cells and the track ϕ position extrapolated to layer-2.

TrackMatchEoverP is the ratio of the cluster energy to the track momentum. It should be close to unity for a real electron as the electron mass is negligibly small compared to its energy at the LHC.

TrackTRThits is the total number of hits left in the TRT by the electron candidate.

TrackTRTratio is the ratio of the high threshold hits to the total number of hits in the TRT. The ratio should be bigger for an electron compared to a heavier particle as the number of transition radiation photons emitted is inversely proportional to the mass of charged particle passing through the TRT.

For each variable a threshold value or a threshold window between a minimum and a maximum value is determined. Then, for a given identification variable, the electron candidate is required to have a value above or below the threshold or in the threshold window. Electron candidates without the desired identification values are not selected and are said to be cut. Therefore, threshold values are often referred to as cut values and groups of selections are referred to as cuts. The ATLAS standard identification is optimized (i.e. cut values are determined) in several bins of the electron candidate E_{T} and η taking into account variations of the ATLAS detector response in different regions especially due to the change

in the amount of dead material in front of the EM calorimeter. MC simulated samples of single electrons and electrons from the $Z \to e^+e^-$ process for the signal, and MC simulated sample of inclusive jets for the background are used for this optimization.

The loose identification combines ClusterEtaRange, ClusterHadronicLeakage, ClusterMiddleEnergy, ClusterMiddleEratio37 and ClusterMiddleWidth quality variables. The medium identification requires, in addition to the loose identification, ClusterStripsDeltaE, ClusterStripsWtot, ClusterStripsFracm, ClusterStripsWeta1c, TrackPixel, TrackSi and TrackA0 selections. The tight identification requires all of the standard selection criteria. The identification category is optimized to a certain target efficiency for identifying real electrons and jet rejection based on requirements from various intended physics measurements. The loose identification is highly efficient in selecting real electrons at the expense of a low background rejection. The tight selection, on the other hand, is about 64% efficient in identifying isolated electrons with E_{T} in the range 10 GeV - 40 GeV, but provides a jet rejection of the order of 10^5.

For Drell-Yan electrons, distributions of all identification variables in the tight selection are studied to determine the discrimination power of each variable against the inclusive jet background. The formula used to estimate the discrimination power is

$$\text{Power} = \sum_{i}^{n_{\text{bins}}} \frac{(S_i - B_i)^2}{S_i + B_i} \tag{5.1}$$

where S_i is the number of all DY signal electrons in a bin i, and B_i is the number of all inclusive jet background electrons in the same bin i. Table 5.2 lists the identification variables based on their rank in discriminating DY signal electrons against the inclusive jet

background. Only those electron candidates with $E_{\mathrm{T}} > 6$ GeV and $|\eta| < 2.5$ excluding the crack region, $1.37 < |\eta| < 1.52$, between barrel and endcap EM calorimeters, are considered in this estimate. Not surprisingly, ClusterIsolation is the most discriminant identification

Identification variable	Power	Rank
ClusterIsolation	1.2048	1
TrackMatchEta	0.9426	2
ClusterMiddleEratio37	0.8706	3
TrackTRTratio	0.7194	4
ClusterHadronicLeakage	0.6627	5
ClusterStripsWtot	0.5722	6
ClusterStripsDeltaE	0.5526	7
TrackMatchEoverP	0.5070	8
ClusterMiddleWidth	0.4189	9
ClusterStripsDeltaEmax2	0.3646	10
TrackMatchPhi	0.2670	11
ClusterStripsFracm	0.2061	12
ClusterStripsWeta1c	0.1128	13
ClusterMiddleEnergy	0.1079	14
TrackA0	0.0522	15
TrackTRThits	0.0458	16
TrackPixel	0.0423	17
ClusterEtaRange	0.0391	18
TrackBlayer	0.0232	19
TrackSi	0.0069	20

Table 5.2: Ranking of the ATLAS standard electron identification variables based on their discrimination against the inclusive jet background.

variable. It identifies those jets faking electrons since jets generally will deposit energy in a much bigger area both laterally and longitudinally than a real electron. ClusterIsolation also identifies those non-isolated background electrons that are decay products of heavy flavour hadrons since these electrons will have a near-by energy deposit from the associated jet. Figure 5.2 shows distributions of the six standard electron identification variables with

the largest discrimination power for signal and background electrons.

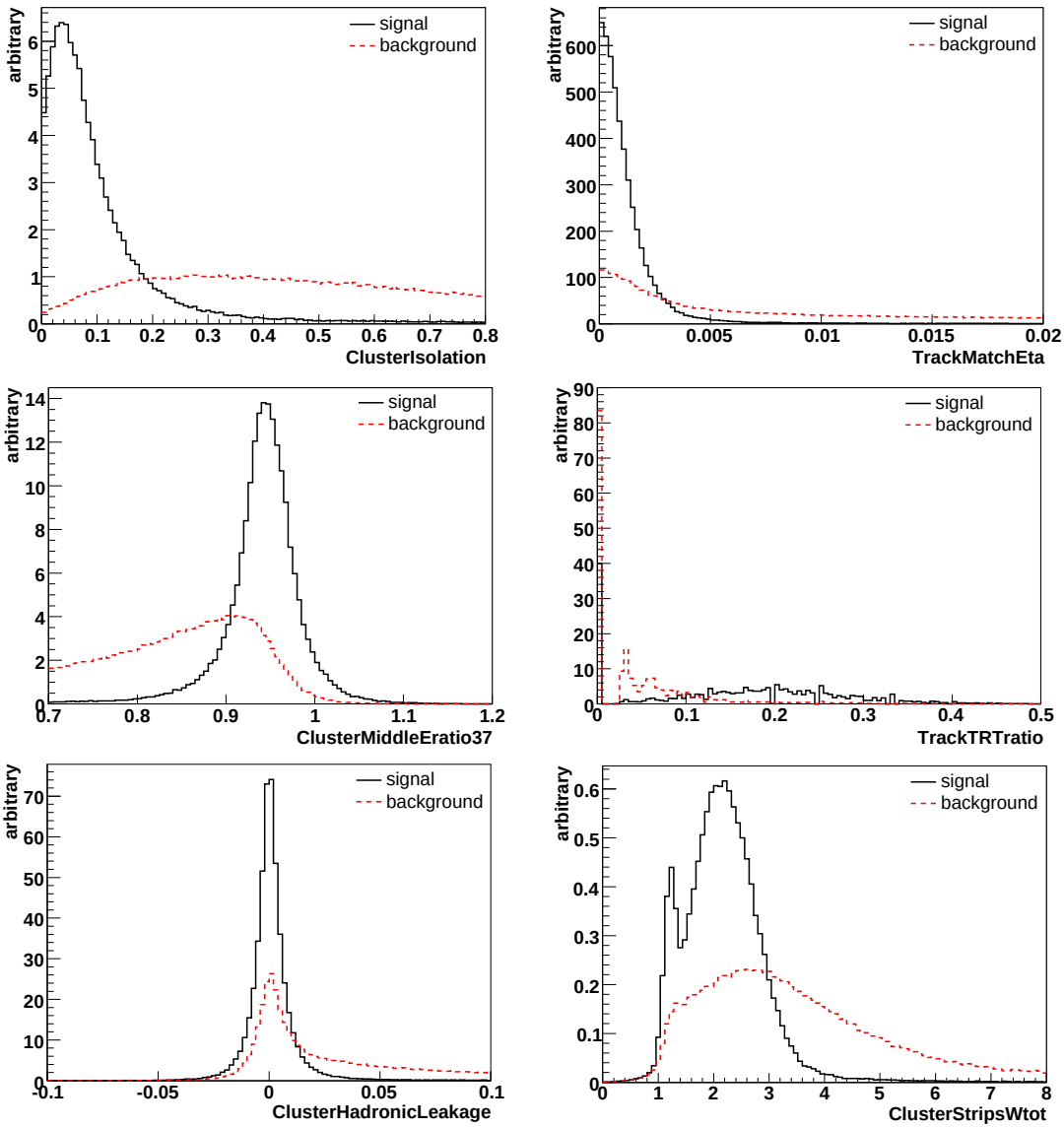

Figure 5.2: Distributions of the six standard electron identification variables with the largest discrimination power. Both signal and background distributions for each variable are normalized to unity.

5.4 Di-electron selection criteria

The measurement of the Drell-Yan spectrum using e^+e^- pairs starts online at the trigger level. At ATLAS, several triggers are designed to select those events with at least one or more electron candidates. Such triggers are essential in quickly identifying and recording well understood SM processes such as the production of J/ψ and Υ mesons and the Z boson that are used to understand the performance of and to calibrate the ATLAS detector in preparation for searching for the unknown (i.e. new physics).

Drell-Yan like events will initially be selected using a low threshold di-electron trigger, called `2e5`, that identifies events with at least two electron candidates, each of which has $E_{\mathrm{T}} > 5$ GeV. After the trigger selection, a series of offline selection criteria are required to identify efficiently Drell-Yan electron pairs while reducing all potential background. The first of these selection criteria requires each electron candidate to be within the tracking range, $|\eta| < 2.5$ of the detector excluding the transition region, $1.37 < |\eta| < 1.52$, between the barrel and endcap EM calorimeters. The transition region is excluded at the early stages of the LHC operation as it will take some time to understand and calibrate particles going through this part of the detector. Each electron candidate also must have $E_{\mathrm{T}} > 8$ GeV. The reason for requiring a higher E_{T} threshold than the trigger is to exclude electrons in the so-called trigger turn-on region. The trigger uses a cluster of read-out towers with reduced granularity, $\Delta\eta \times \Delta\phi = 0.1 \times 0.1$, to measure the energy of electron candidates in order to make a quick decision on whether to record the event, and the E_{T} resolution of electrons as seen by the trigger is worse than the E_{T} measured offline using the full granularity of

the calorimeter. Therefore, the trigger efficiency for identifying electron candidates with a certain E_{T} threshold decreases dramatically when close to the trigger threshold, and consequently it will take longer to understand and measure the efficiency in this region near the threshold. Each electron is also required to satisfy the standard tight identification criteria. The tight selection is essential in eliminating most of the inclusive jet background from fake electrons or from secondary electrons coming from decays of heavy flavour hadrons. A DY event is then required to have exactly two such electrons that are oppositely charged. This requirement especially eliminates those background events with more than two electrons. In addition, a DY event must not have a significant amount of missing transverse energy, $E_{\mathrm{T}}^{\mathrm{miss}} < 25$ GeV, as it should not have any undetected particles like neutrinos. The value 25 GeV is about three times the $E_{\mathrm{T}}^{\mathrm{miss}}$ resolution of the ATLAS detector and nearly all Drell-Yan events have $E_{\mathrm{T}}^{\mathrm{miss}}$ less than this amount. Finally, the invariant mass, m_{ee}, of the DY electron pair is required to be within the range, 10 GeV $< m_{ee} <$ 60 GeV, of interest. The effect of each selection criterion on signal and background events is listed on table 5.3.

Selection	Signal	$\tau^+\tau^-$	Di-boson	$t\bar{t}$	Inclusive jets
Trigger	29302 ± 215	291 ± 12	1401 ± 8	1824 ± 12	$10^7 \pm 10^6$
Exclude crack	27977 ± 210	272 ± 12	1341 ± 8	1814 ± 12	$10^7 \pm 10^6$
$E_{\mathrm{T}} > 8$ GeV	15685 ± 157	245 ± 11	1307 ± 8	1684 ± 12	$10^6 \pm 10^6$
Tight identification	9138 ± 120	85 ± 7	643 ± 5	419 ± 6	0 ± 0
$E_{\mathrm{T}}^{\mathrm{miss}} < 25$ GeV	9075 ± 120	64 ± 6	288 ± 3	39 ± 2	
$10 < m_{ee} < 60$ GeV	8061 ± 113	48 ± 5	14 ± 1	12 ± 1	

Table 5.3: Drell-Yan signal and background event rates after each selection for 100 pb^{-1} LHC data. Due to lack of enough simulated data, the inclusive jet background is estimated with an alternative method based on single electrons described in section 5.5.

Although there are over two million simulated inclusive jet events, the corresponding integrated luminosity is very small due to their high cross-section and is 10^5 times less than the simulated signal sample. Therefore, a Drell-Yan like di-electron selection analysis as listed in table 5.3 yields a result that is statistically not reliable. In order to have a reasonable number of events for such an analysis, about a billion inclusive jet events need to be simulated. Simulation of such a large sample would take a long time and is not feasible. Consequently, an alternative method is used to estimate this background from the available number of events as explained in section 5.5. The three other types of background are very small accounting combined for less than 1% of all selected events with the $\tau^+\tau^-$background being the dominant one.

5.5 QCD background estimation

The number of inclusive jet events containing a pair of oppositely charged electrons passing the selection criteria listed in table 5.3 is found to be compatible with zero, but this may be an artifact of an inadequate number of simulated inclusive jet events. An alternative method of estimation based on single electrons is developed. The principle of this method is to determine the probability of finding a good (i.e. satisfying the desired criteria) pair of oppositely charged electrons per event given the probability of finding a single good electron which can be calculated from the available simulated inclusive jet sample. In addition to the estimation of the amount of inclusive jet background which will be referred to as normalization from here on, the shape of the background distribution is of importance and is determined as well.

In order to estimate the normalization, the jet background electrons are considered in two main categories: electrons faked by jets and non-isolated real electrons coming from heavy hadron decays. Real electrons and fakes need to be treated separately as their signatures in the detector have different characteristics, and hence the efficiency of the selection criteria rejecting them differs. Figure 5.3 illustrates typical signatures that jets will leave in the detector. The background coming from jets originating from light flavour

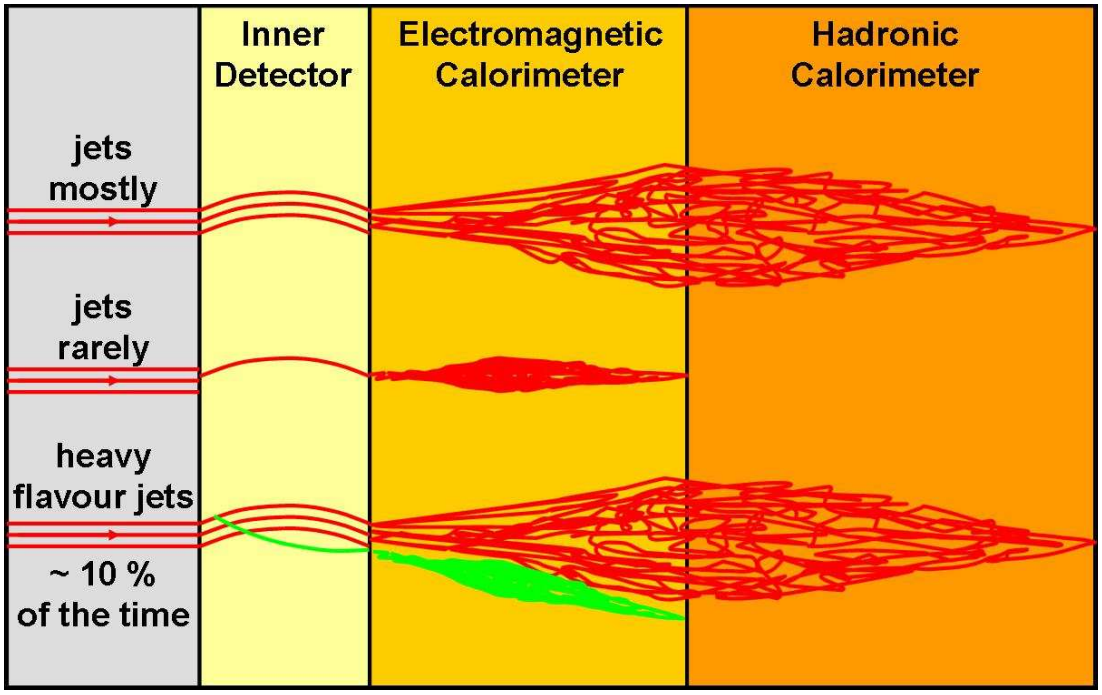

Figure 5.3: Schematic view of typical signatures of jets in the ATLAS detector.

partons (u, d and s quarks, and gluons) is mostly due to fake electrons whereas jets from heavy flavour partons (b and c quarks) are more likely to produce real non-isolated electrons than to fake electrons [44]. For this reason, the inclusive jet sample is separated into light and heavy events [45]. A heavy event means it must contain at least one jet originating from

a heavy flavour parton of $p_{\mathrm{T}} > 2$ GeV within $|\eta| < 3.5$ that has some chance of producing a non-isolated real electron. If an event is not heavy then it considered as light. Analytically, it can be formulated as

$$N_{\mathrm{T}} = N_{\mathrm{T}} \left(f_{\mathrm{l}} + f_{\mathrm{h}} \right) \tag{5.2}$$

where N_{T} is the total number of inclusive jet events, f_{l} is the fraction of light events, and f_{h} is the fraction of heavy events. The total probability of a good background electron pair with opposite charges is, then, defined as

$$P_{\mathrm{T}} = \left(f_{\mathrm{l}} P_{\mathrm{l}} + f_{\mathrm{h}} P_{\mathrm{h}} \right) / 2 \tag{5.3}$$

where P_{l} and P_{h} are the probabilities of a good pair from a light and heavy event, respectively. The occurrence of a jet faking an electron is random and, hence, follows the Poisson distribution. The probability of a good pair in a light event can be calculated with

$$P_{\mathrm{l}} = P(2, \lambda_{\mathrm{l}}) = \frac{\lambda_{\mathrm{l}}^2}{2!} e^{-\lambda_{\mathrm{l}}} \tag{5.4}$$

where λ_{l} is the average number of fake electrons in a light event. On the other hand, a heavy event, assuming two hadrons originating from heavy partons, may produce three different types of a good pair where both electrons may be real electrons or one may be real while the other is fake or both may be fakes. The probability of a good pair thence can be written as

$$P_{\mathrm{h}} = B_e^2 \epsilon_e^2 + 2 B_e \epsilon_e (1 - B_e) P(1, \lambda_{\mathrm{h}}) + (1 - B_e)^2 P(2, \lambda_{\mathrm{h}}) \tag{5.5}$$

where B_e is the effective branching ratio, probability, for a heavy hadron decaying into an electron and another hadron, and ϵ_e is the efficiency of accepting those non-isolated real

electrons. In other words, ϵ_e is the fraction of the time those real background electrons that pass the selection criteria. The quantity $\lambda_{\rm h}$ is the average number of fake electrons in a heavy event, and it should approximately be the same as $\lambda_{\rm l}$.

Equation 5.5 is written for the simple case of a heavy event with two heavy flavour hadrons. However, heavy events are more complicated. There are processes where a heavy event may end up having one, three or four heavy flavour hadrons as well. For example, originally a parton-parton interaction may produce a heavy quark and a gluon. The gluon may pair produce two more heavy quarks resulting in three heavy quarks which will then turn into three heavy hadrons. There may be two gluons from the final state of a parton-parton interaction and both gluons may pair produce heavy quarks turning into four heavy hadrons in the heavy event. There may also be a small number of simple scattering processes of heavy and light quarks causing one heavy and one light hadron in the event. Finally, a heavy hadron may cause production of multiple real electrons through either a direct decay into two electrons such as from an Υ meson or indirectly where the heavy hadron decays into one electron and another heavy hadron which also may decay leptonically resulting in more than one electron from such a cascade. Taking all these possibilities into account, equation 5.5 can be extended to

$$P_{\rm h} = f_g \left[f_{\rm c}^2 B_e^2 \epsilon_e^2 + 2 f_{\rm c} B_e \epsilon_e (1 - B_e) P(1, \lambda_{\rm h}) + (1 - B_e)^2 P(2, \lambda_{\rm h}) \right] \tag{5.6}$$

where $f_{\rm c}$ is the effective factor of correlation to include the possibility for a heavy hadron causing production of multiple real electrons, and $f_{\rm g}$ is the effective gluon splitting factor that includes the possibility of the number of heavy hadrons per event being different than

two. f_c is defined as

$$f_c^2 = \frac{N_{\text{pair}}}{P_{\text{single}}^2 N_{\text{hpart}}}$$

where N_{pair} is the total number of pairs of real electrons coming from heavy hadron decays, and N_{hpart} is the total number of heavy hadrons. P_{single} is the probability of a real electron coming from a heavy hadron decay.

For the validation of this method, much looser selection criteria than those in table 5.3 are defined so that comparison of the results of this method with the DY-like di-electron selection method is possible with the existing size of the simulated inclusive jet sample. All electron candidates satisfying the standard loose identification criteria with E_{T} > 6 GeV and $|\eta| < 2.5$ excluding the crack region are considered. The offline E_{T} threshold of 6 GeV is chosen to be the lowest feasible given the generator filter already applied to this inclusive jet sample is 6 GeV. In order to calculate all of the parameters in equations 5.4 and 5.6 and hence the probability of finding a pair of loose electrons of $E_{\text{T}} > 6$ GeV and $|\eta| < 2.5$ excluding the crack region in a inclusive jet event, two histograms are produced as shown in figure 5.4. The upper plot presents the number of events falling into each category of event classification except for the right most bin which shows the total number of heavy hadrons, labeled as nheavy, in all events. The lower plot shows the number of background electrons passing the loose selection criteria. Event classification is done using the theoretical information from the generation level of the ATLAS MC chain. The description of each horizontal bin label is as follows:

total is the number of all inclusive jet events.

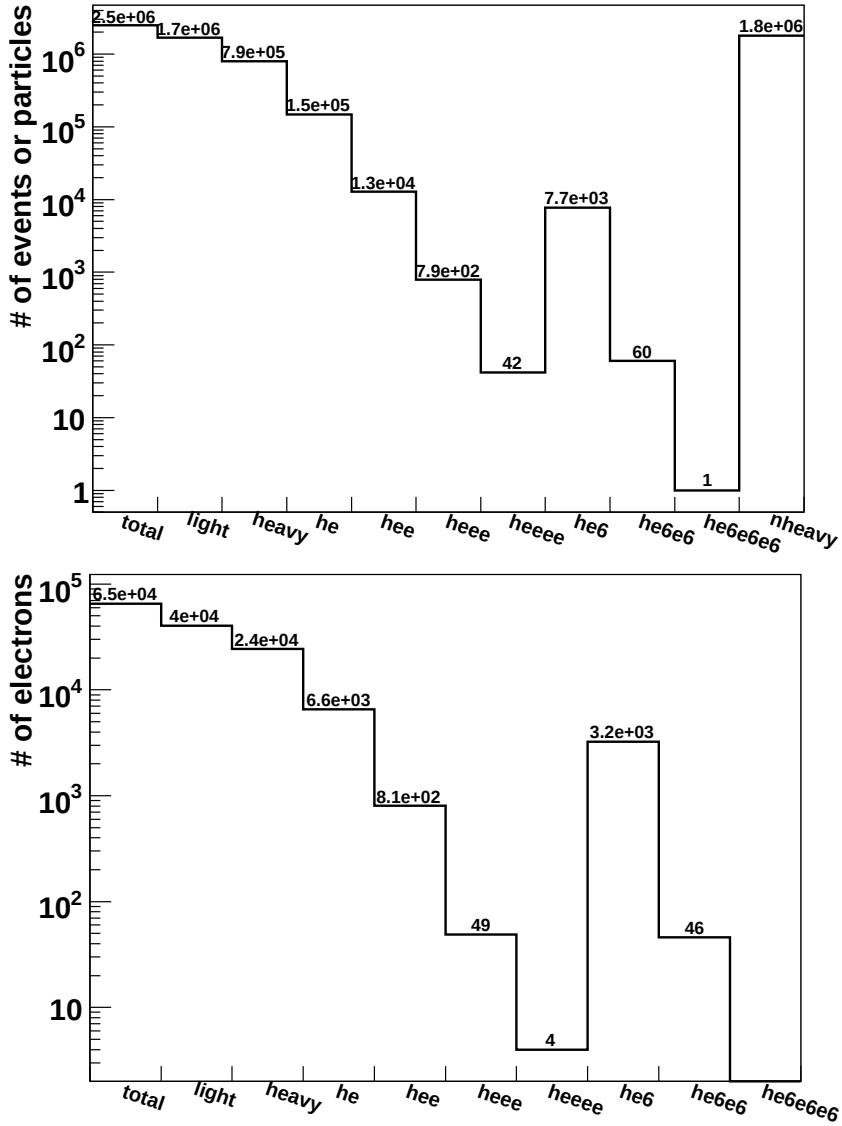

Figure 5.4: Classification of inclusive jet events in the upper plot and background electrons in the lower plot. The sample corresponds to 6.1×10^{-4} pb^{-1} of LHC data. Detailed description of each plot is provided in the text.

light is the number of light inclusive jet events.

heavy is the number of heavy inclusive jet events.

he is the number of heavy events where one heavy hadron decayed leptonically producing at least one real electron per event.

hee is the number of heavy events where two heavy hadrons decayed leptonically each producing at least one real electron per event.

heee is the number of heavy events where three heavy hadrons decayed leptonically each producing at least one real electron per event.

heeee is the number of heavy events where four heavy hadrons decayed leptonically each producing at least one real electron per event.

he6 is the number of heavy events where there is one real electron of $E_{\mathrm{T}} > 6 - 3 \times \sigma_E$ GeV and $|\eta| < 2.5 + 3\sigma_\eta$ excluding the crack region per event coming from a heavy hadron decay that is likely to be reconstructed and pass the selection criteria. The σ_E and σ_η are the calorimeter energy and η position resolutions, respectively, as given in section 3.2.3.

he6e6 is the number of heavy events with two real electrons likely to be reconstructed and identified per event coming from heavy hadron decays.

he6e6e6 is the number of heavy events with three real electrons likely to be reconstructed and identified per event coming from heavy hadron decays.

The variables of equations 5.4 and 5.6 are calculated as follows

$$
\begin{aligned}
\lambda_{\mathrm{l}} &= \frac{N_{\mathrm{ele}}(\mathrm{light})}{N_{\mathrm{evt}}(\mathrm{light})} = 0.024 \\
f_g &= \frac{N_{\mathrm{prt}}(\mathrm{nheavy})}{2N_{\mathrm{evt}}(\mathrm{heavy})} = 1.13 \\
f_c &= \sqrt{\frac{N_{\mathrm{ele}}(\mathrm{he6e6}) + 2N_{\mathrm{ele}}(\mathrm{he6e6e6})}{\left[\frac{[N_{\mathrm{ele}}(\mathrm{he6})+2N_{\mathrm{ele}}(\mathrm{he6e6})+3N_{\mathrm{ele}}(\mathrm{he6e6e6})]^2}{N_{\mathrm{prt}}(\mathrm{nheavy})}\right]}} = 1.35 \\
B_e &= \frac{N_{\mathrm{evt}}(\mathrm{he}) + 2N_{\mathrm{evt}}(\mathrm{hee}) + 3N_{\mathrm{evt}}(\mathrm{heee}) + 4N_{\mathrm{evt}}(\mathrm{heeee})}{N_{\mathrm{prt}}(\mathrm{nheavy})} = 0.098 \\
\epsilon_e &= \frac{N_{\mathrm{ele}}(\mathrm{he}) + N_{\mathrm{ele}}(\mathrm{hee}) + N_{\mathrm{ele}}(\mathrm{heee}) + N_{\mathrm{ele}}(\mathrm{heeee})}{N_{\mathrm{evt}}(\mathrm{he}) + 2N_{\mathrm{evt}}(\mathrm{hee}) + 3N_{\mathrm{evt}}(\mathrm{heee}) + 4N_{\mathrm{evt}}(\mathrm{heeee})} = 0.042 \\
\lambda_{\mathrm{h}} &= \frac{N_{\mathrm{ele}}(\mathrm{heavy}) - N_{\mathrm{ele}}(\mathrm{he}) - N_{\mathrm{ele}}(\mathrm{hee}) - N_{\mathrm{ele}}(\mathrm{heee}) - N_{\mathrm{ele}}(\mathrm{heeee})}{N_{\mathrm{evt}}(\mathrm{heavy}) - N_{\mathrm{evt}}(\mathrm{he}) - N_{\mathrm{evt}}(\mathrm{hee}) - N_{\mathrm{evt}}(\mathrm{heee}) - N_{\mathrm{evt}}(\mathrm{heeee})} = 0.027
\end{aligned}
$$

where the bin labels from figure 5.4 are included in brackets. N_{ele}, N_{evt} and N_{prt} are the number of electrons, events and particles respectively. Note that λ_{l} is similar to λ_{h} as expected. Consequently, the probability of finding a pair of oppositely charged loose electrons of $E_{\mathrm{T}} > 6$ GeV and $|\eta| < 2.5$ excluding the crack region in an inclusive jet event is found to be $P_{\mathrm{T}} = (2.00 \pm 0.02) \times 10^{-4}$. The uncertainty on the total probability is calculated using the error propagation theory and the error matrix method [46].

The next step is to estimate the shape of the background distribution. Figure 5.5 shows a comparison between the invariant mass distribution of all possible pairs of background electrons with $E_{\mathrm{T}} > 6$ GeV and $|\eta| < 2.5$ excluding the crack region in the dashed-lined histogram which will be referred to as the base distribution and those also passing the loose identification criteria in the solid-lined histogram. The change in shape is due to the change in the efficiency of loose identification in rejecting background electrons as the E_{T} of the electron candidates changes. Figure 5.6 shows the fraction of inclusive jet

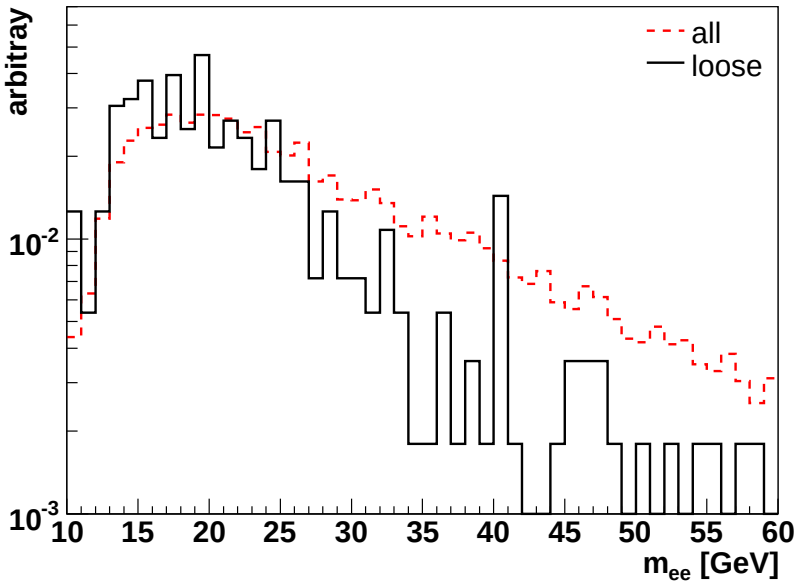

Figure 5.5: Change in shape of the inclusive jet background distribution after applying loose identification criteria. Both histograms are normalized to unity.

background electrons passing the loose identification as a function of the E_{T} of the electron candidate. At low E_{T}, the rejection power of the loose identification decreases. This change in efficiency can be parametrized and used to re-weight the base invariant mass distribution of all background electrons with $E_{\mathrm{T}} > 6$ GeV and $|\eta| < 2.5$ excluding the crack region to predict the shape of the distribution after the loose identification is applied. That is, for the invariant mass of each pair from the base distribution, to assign a weight that is the product of the weights for each electron candidate of the pair, obtained from figure 5.6 based on their E_{T}, to estimate the shape of the distribution after the loose identification is applied. The function used for parametrization is of the form

$$f_{\mathrm{w}}(E_{\mathrm{T}}) = \frac{p_0}{E_{\mathrm{T}}^{p_1}} \tag{5.7}$$

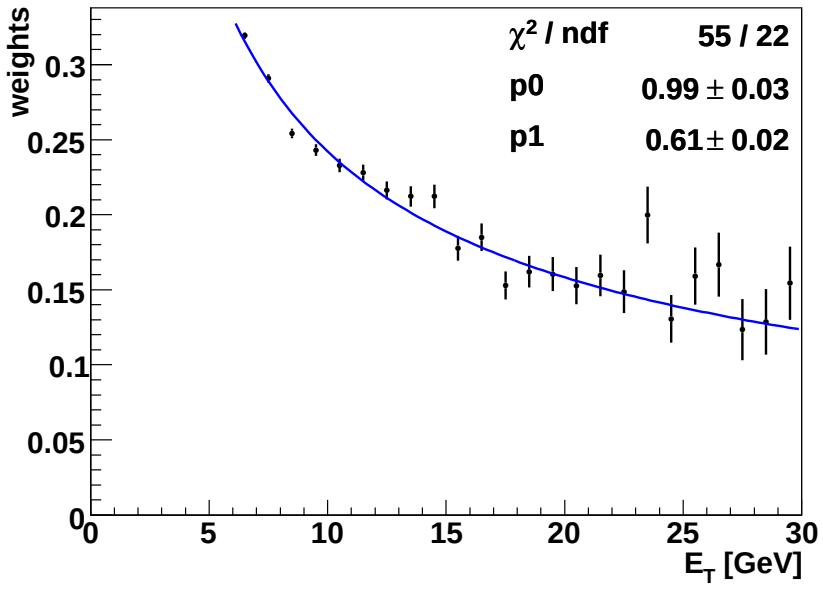

Figure 5.6: Fraction of inclusive jet background electrons passing loose identification as a function of electron E_{T}.

where p_0 and p_1 are parameters determined with a χ^2 minimization, and the best values are shown on the plot.

With the normalization determined earlier and prediction of the shape described above, the invariant mass distribution of inclusive jet background electrons of $E_{\mathrm{T}} > 6$ GeV and $|\eta| < 2.5$ excluding the crack region and passing the loose identification is estimated and compared to the direct method of Drell-Yan like di-electron selection on figure 5.7. Though the method using single electrons seems to slightly overestimate the normalization of the background, this is not a concern as it provides a conservative estimate of likely the dominant background to Drell-Yan.

The method therefore can be repeated to estimate the inclusive jet background after the tight selection listed on table 5.3 for which the DY like di-electron selection does not

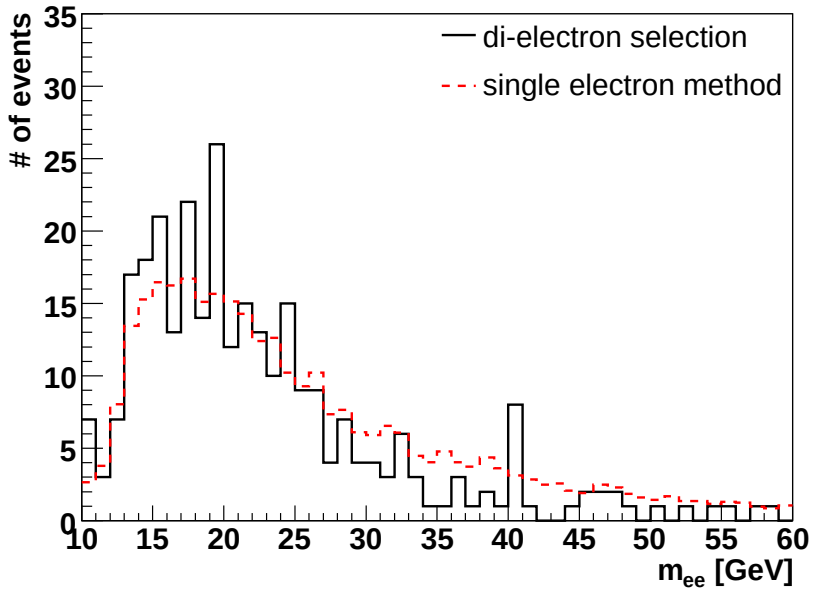

Figure 5.7: Validation of the inclusive jet background estimation method. The solid-lined histogram is obtained with a DY like di-electron selection, while the dashed-lined histogram is the estimation using single electrons.

lead to a reliable result due to the small size of the inclusive jet sample. Consequently, the probability of finding a pair of inclusive jet background electrons passing the selection criteria listed on table 5.3 is found to be $P_{\mathrm{T}} = (8.35 \pm 0.63) \times 10^{-8}$. Figure 5.8 presents the invariant mass distributions of Drell-Yan signal and all background electron pairs including an estimate of the inclusive jet background. The solid-lined distribution is the sum of DY signal and all background species and illustrates what will be measured with the LHC data. The inclusive jet background constitutes about three quarters of the measured spectrum. The ATLAS standard tight identification is obviously not enough to select the DY signal sufficiently pure of the background in this low invariant mass region. The standard tight selection needs to be optimized and/or expanded with more identification variables to

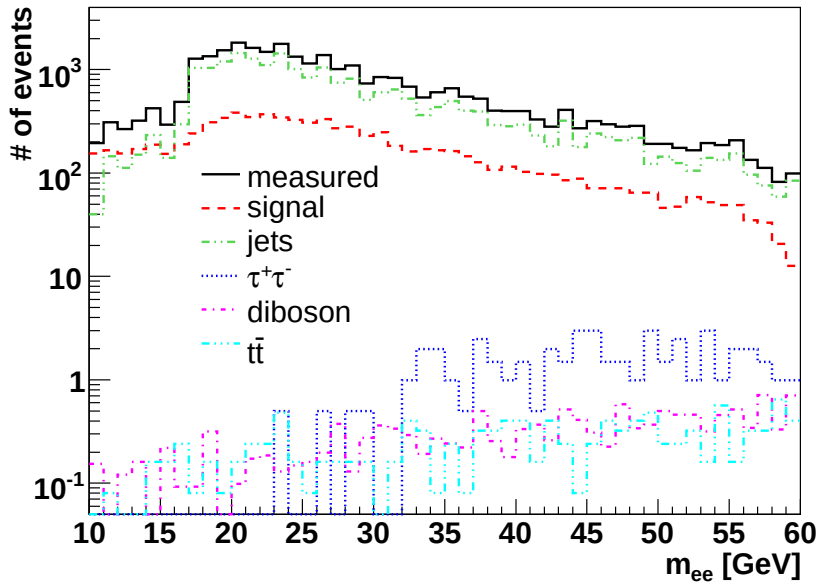

Figure 5.8: Invariant mass distributions of Drell-Yan signal and background events passing the tight selection listed on table 5.3 for 100 pb^{-1} of LHC data. The solid-lined distribution represents the sum of the signal and all background species.

efficiently reject the inclusive jet background in this region.

5.6 Reduction of the QCD background

Reduction of the inclusive jet background requires understanding its composition and characteristics. Given the event classification described in the previous section, figure 5.9 shows the composition of inclusive jet background electrons with $E_{\mathrm{T}} > 8$ GeV and $|\eta| < 2.5$ excluding the crack region that pass the ATLAS standard tight selection. One fifth of these background electrons are from light flavour events while the remainder are from heavy flavour events. About 88% of those electrons from the heavy flavour events are real non-isolated electrons. In general, approximately 70% of the background electrons are real

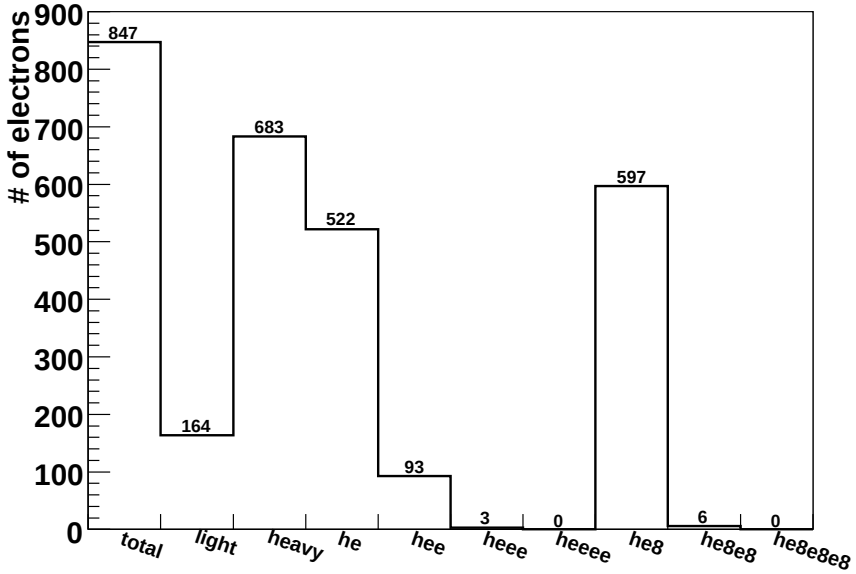

Figure 5.9: Classification of inclusive jet background electrons passing the tight identification. The sample corresponds to 6.1×10^{-4} pb^{-1} of LHC data.

non-isolated electrons while 30% are fakes neglecting a small fraction of real electrons coming from light hadron decays such as π^0 and from photons pair-producing due to interactions with the inner detector material. This small fraction of real background electrons remains as an irreducible background since they are isolated like DY electrons and are essentially indistinguishable from them.

As illustrated in figure 5.3, a real non-isolated background electron coming from heavy hadron decay leaves a detector signature with two main characteristics. The first is the fact that this electron will not be coming directly from the interaction point unlike a DY electron, as the heavy hadron on average will travel some distance before it decays. The second characteristic is that there will be a jet produced by the hadron coming also from the heavy hadron decay near-by the electron. As for the fake electrons, the main characteristic is

that they in general produce much bigger showers than DY electrons both transversely and longitudinally. Given all these characteristics, three identification variables are identified that can be used to distinguish the remaining inclusive jet background electrons from DY electrons. The variables are ClusterIsolation, TrackA0 and PtRelJetAxis. PtRelJetAxis is the electron p_{T} relative to the closest jet direction and is used along with the TrackA0 to reduce those real non-isolated background electrons. ClusterIsolation is used to reduce both fakes and real non-isolated electrons. Figure 5.10 shows the distributions of these variables using DY signal and background electrons that pass the standard tight identification. As can be seen, all three variables have clear identification power to separate more of the background electrons from DY electrons. The vertical solid lines and arrows show the thresholds for each variable and the selected candidates for the barrel region. Distributions are very similar for the endcap region. ClusterIsolation and TrackA0 already exist in the standard tight selection, but they can be optimized for this low E_{T} region. There are no significant correlations between these variables as shown in figure 5.11.

In order to determine the cut values for further reduction of the inclusive jet background, each variable is considered separately at first. For each variable, a starting cut value is chosen and applied in addition to the standard tight selection. DY signal selection efficiency and purity is calculated. Then, the cut value is changed by small amounts up and down. For each step, efficiency and purity is calculated. The cut value that maximizes the product of efficiency and purity is chosen to be the optimum cut value for each variable. The optimum cut value for ClusterIsolation is 0.12 for both barrel, $|\eta| < 1.37$, and endcap,

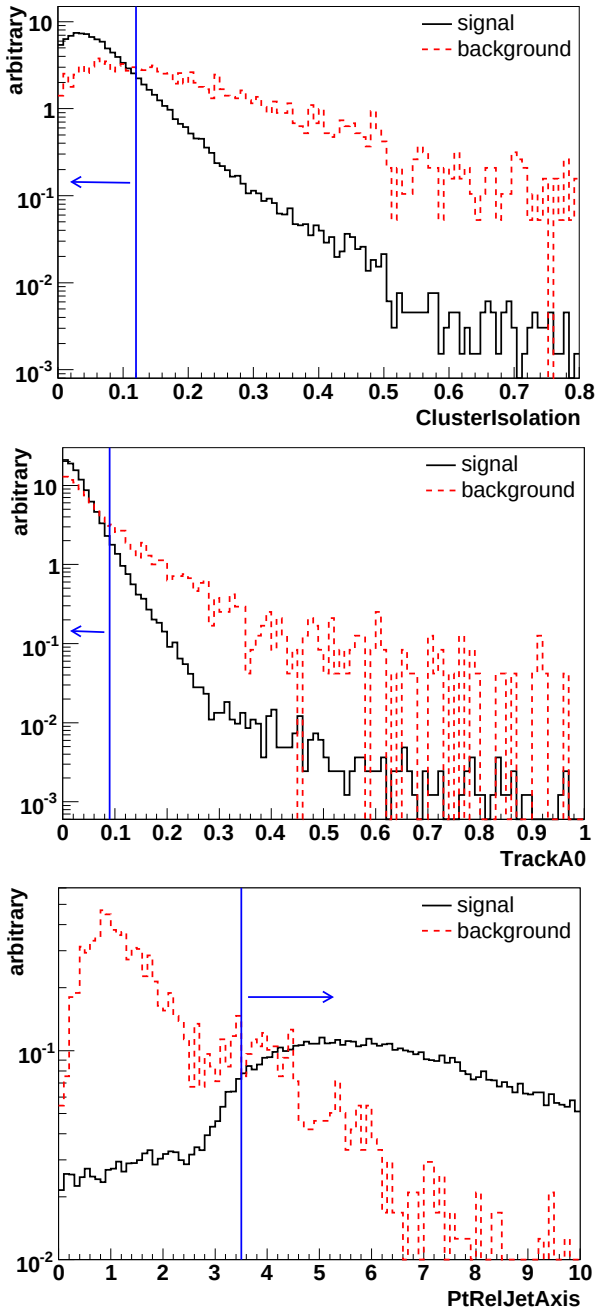

Figure 5.10: Distributions of the three additional variables to the standard tight identification. Both signal and background distributions for each variable are normalized to unity. The vertical solid lines and arrows show the thresholds and the selected candidates for the barrel region. Distributions are very similar for the endcap region.

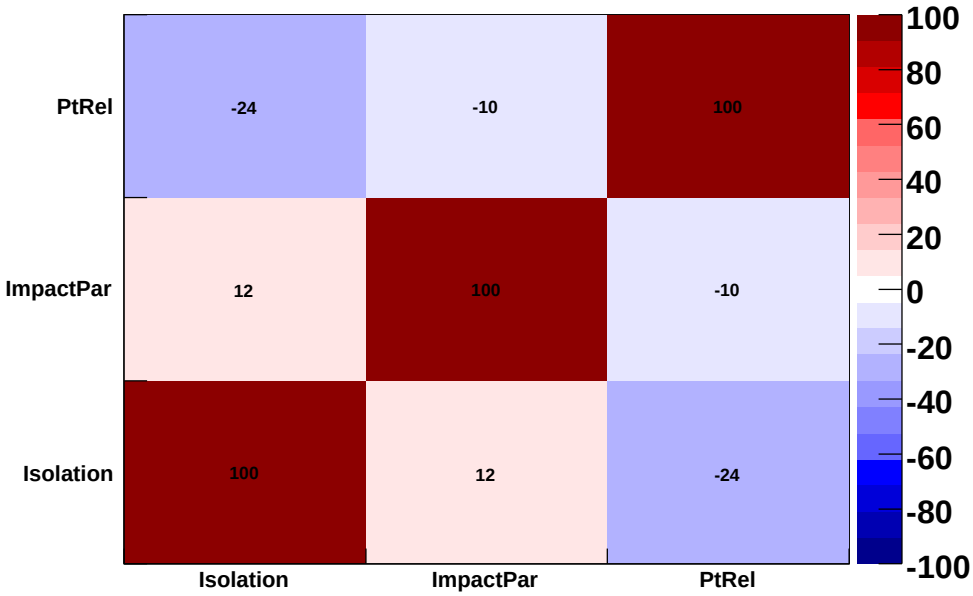

Figure 5.11: Correlation matrix of the three additional variables to the standard tight identification. The matrix is calculated using signal electrons passing the tight selection.

$|\eta| > 1.52$, regions. For TrackA0, the cut values are 0.09 mm and 0.15 mm for barrel and endcap regions respectively. The cut value for the PtRelJetAxis variable is 3.5 GeV for both barrel and endcap regions.

Figure 5.12 shows the remaining inclusive jet background electrons that satisfy these three additional identification criteria as well as the standard tight selection. The vertical axis range is kept the same for easy comparison with figure 5.9. About 83% of those background electrons passing the standard tight selection fail to pass the tighter selection that includes these three additional identification criteria as well as the standard tight selection.

The tighter selection criteria in addition to the selection listed in table 5.3 is applied

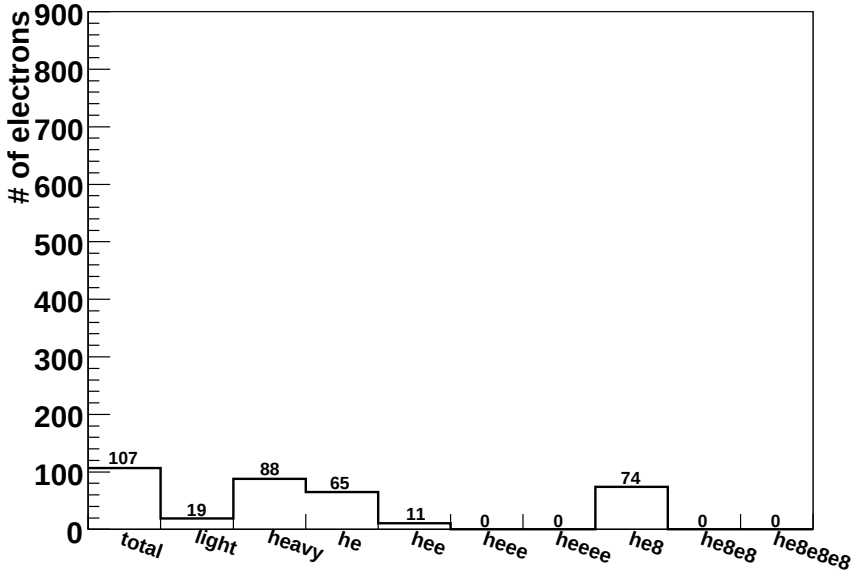

Figure 5.12: Classification of inclusive jet background electrons passing the tighter identification. The sample corresponds to 6.1×10^{-4} pb^{-1} of LHC data.

to both the DY signal and all background samples. The probability of finding a pair of inclusive jet background electrons passing the tighter selection in addition to the selection listed on table 5.3 is found to be $P_{\mathrm{T}} = (1.42 \pm 0.31) \times 10^{-9}$. Table 5.4 shows the event rates calculated for 100 pb^{-1} of LHC data. The inclusive jet background is reduced by

Selection	Signal	$\tau^+\tau^-$	Di-boson	$t\bar{t}$	Inclusive jets
Table 5.3 criteria	8061 ± 113	48 ± 5	14 ± 1	12 ± 1	22400 ± 445
Tighter identification	5732 ± 95	28 ± 4	13 ± 1	7 ± 1	383 ± 7

Table 5.4: Drell-Yan signal and background event rates after the estimation and reduction of inclusive jet background for 100 pb^{-1} LHC data. The tighter identification requires, in addition to the ATLAS standard tight selection, identification based on the electron p_{T} relative to the closest jet axis as well as more strict isolation and impact parameter criteria optimized to reduce the inclusive jet background for this measurement.

about a factor of 60 at the expense of approximately 30% loss in DY signal efficiency. The

corresponding invariant mass distributions of the DY signal and all background species are shown in figure 5.13. The DY signal now constitutes 93% of the measured spectrum.

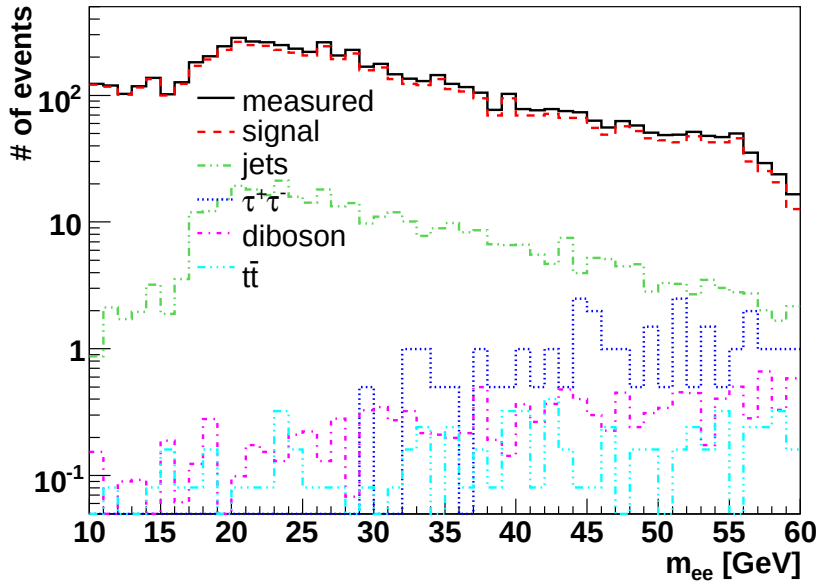

Figure 5.13: Invariant mass distributions of Drell-Yan signal and background events passing the tighter selection listed on table 5.4. The solid-lined distribution represents the sum of the signal and all background species.

The inclusive jet background only makes up about 6% of the measured spectrum as the dominant background.

Chapter 6

Determination of experimental limitations

The extent to which an experiment tests a particular scientific theory is limited by the capabilities of the experimental setup. For the ATLAS experiment, these limitations can be divided into two main categories called acceptance and efficiency. Particles produced in proton-proton collisions leaving the interaction point come in many different types, energies and directions. Acceptance is the energy and direction range of capability of the ATLAS detector in measuring these particles. Efficiency is the probability of correctly determining the type of a particle based on the signature left in the detector.

In this chapter, the acceptance and efficiency of the ATLAS detector in measuring Drell-Yan electrons are calculated in order to correct the invariant mass spectrum obtained in chapter 5.

6.1 Acceptance

ATLAS will not be able to identify electrons well in the forward region of the detector, since the inner detector only covers the region $|\eta| \leq 2.5$. It is very difficult to distinguish

electrons from photons using the calorimeters alone without reliable information from the inner detector since both particles leave very similar signatures. In other words, the ATLAS detector can only identify electrons if they go through certain parts of the detector geometry. This is known as geometrical acceptance.

In this work, electrons with $E_{\mathrm{T}} > 8$ GeV and $|\eta| \leq 2.5$ excluding the crack region, $1.37 < |\eta| < 1.52$, are considered within the acceptance. In order to calculate the acceptance as a function of the invariant mass of the Drell-Yan electron pairs, the distribution of all theoretically possible DY pairs is compared to those pairs of electrons within the acceptance. When calculating the number of pairs within the acceptance, the effect of detector resolution needs to be taken into account. For instance, an electron of E_{T} slightly less than 8 GeV in reality may be measured as $E_{\mathrm{T}} > 8$ GeV and hence be accepted or an electron of E_{T} slightly more than 8 GeV in reality may be rejected. The detector resolution is dependent on both the energy and direction of particles as detailed in section 3.2. Figure 6.1 shows the EM calorimeter energy resolution for electrons in two different energy and η ranges as examples. The narrower distribution in the higher energy range indicates that the calorimeter resolution improves at higher energy. The wider distribution in the higher η range indicates a degradation in energy resolution. This is due to the increase in the amount of dead material in front of the calorimeters that causes energy loss by bremsstrahlung. The asymmetric tails on the left side of the distributions in figure 6.1 are the result of such energy loss.

For the calculation of acceptance, the calorimeter energy resolution is parametrized

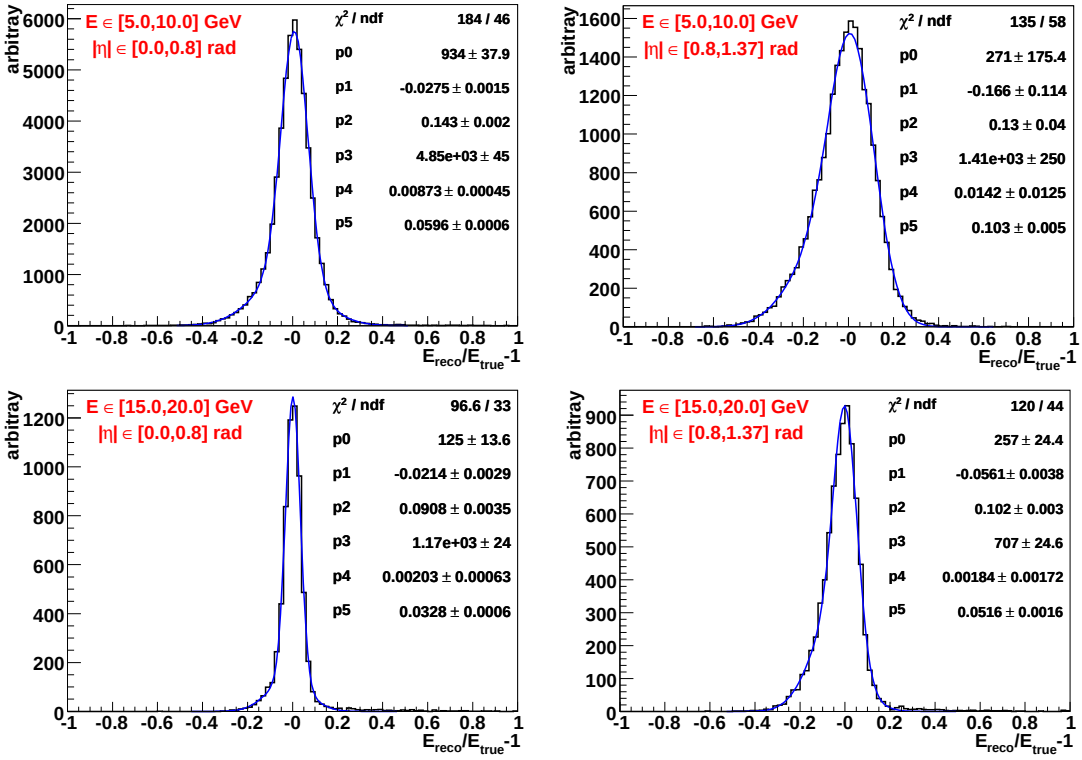

Figure 6.1: Energy resolution for electrons in the EM barrel calorimeter. E_{reco} is the electron energy reconstructed including detector effects. E_{true} is the true electron energy from the generation level of the ATLAS MC production.

with a double gaussian function in several E bins, {0.0, 5.0, 10.0, 15.0, 20.0, 30.0, 50.0, infinity}, and η bins, {0.0, 0.8, 1.37, 1.52, 1.8, 2.0, 2.35, 2.5}. The energy of each true electron from a DY pair is first smeared with these functions. Then, the fraction of those DY pairs with both electrons within the acceptance is calculated. Figure 6.2 displays the acceptance of DY electron pairs as a function of the pair invariant mass. The discontinuity seen at m_{ee} of about 43 GeV is due to a statistical fluctuation in the DY sample. The acceptance is only about 0.5% at 10 GeV due to the distortion of the spectrum caused by the E_{T} threshold. It increases to 10% at 20 GeV and reaches 30% at 50 GeV.

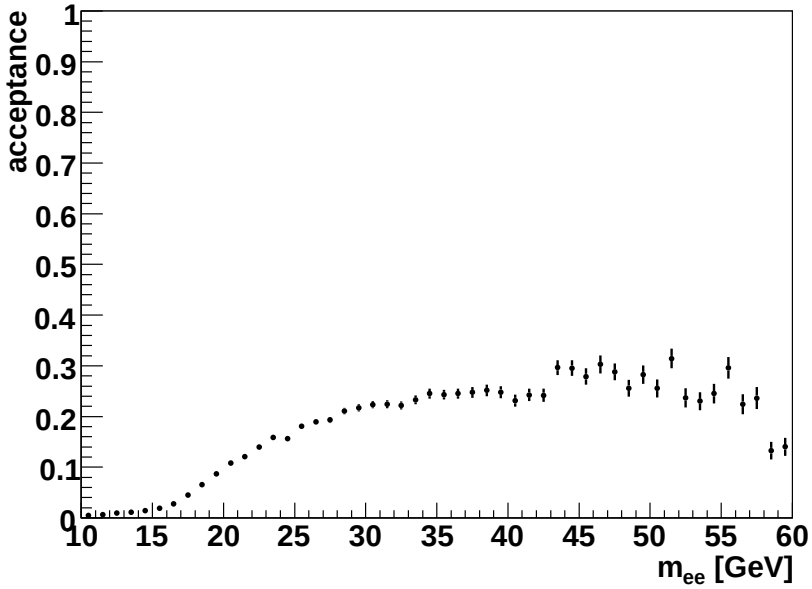

Figure 6.2: Drell-Yan event acceptance as a function of pair invariant mass for electrons with $E_{\mathrm{T}} > 8$ GeV and $|\eta| \leq 2.5$ excluding the crack region. The error bars represent statistical errors for 100 pb^{-1} of data, but the fluctuations are due to a sample size of 63 pb^{-1}.

6.2 Efficiency

The efficiency of finding Drell-Yan electrons within the acceptance will not be 100% as there will be limiting factors in reconstruction, identification and triggering which cause loss of efficiency.

Electron reconstruction involves reconstruction of an EM cluster with $E_{\mathrm{T}} > 3$ GeV and a matching inner detector track within a window of size $\Delta\eta \times \Delta\phi = 0.05 \times 0.1$ and with the ratio, E/p, of the cluster energy and the track momentum less than 10 as explained in section 5.2. Reconstruction efficiency is defined as the ratio of the number of reconstructed electrons to the number of true electrons within the acceptance. Since the detector resolution smears the direction of electrons, reconstructed electrons within ΔR of 0.1 of the true

electrons of the same charge are counted. The loss of efficiency in reconstructing electrons is largely due to the amount of dead material in front of the EM calorimeter. Electrons emitting bremsstrahlung photons in the inner detector may have an E/p ratio bigger than 10 and may not be reconstructed. The more dead material there is, the more likely such a loss is to happen. Hence, the efficiency decreases with increasing η. Figure 6.3 shows the reconstruction efficiency of Drell-Yan electrons within the acceptance as a function of electron E_{T} on the left and η on the right. The reconstruction efficiency as a function of

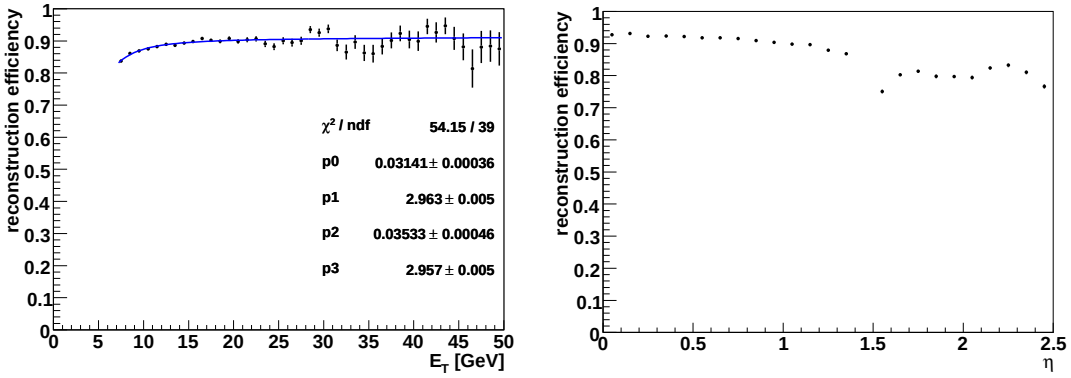

Figure 6.3: Drell-Yan electron reconstruction efficiency as a function of electron E_{T} on the left and η on the right.

E_{T} can be parametrized as illustrated in the left histogram with a function of the form

$$f_{\mathrm{reco}}(E_{\mathrm{T}}) = \frac{p_0 E_{\mathrm{T}}^{p_1}}{1 + p_2 E_{\mathrm{T}}^{p_3}} \tag{6.1}$$

where p_0, p_1, p_2 and p_3 are parameters determined with a χ^2 minimization, and the best values are shown on the plot.

Electron identification variables in the ATLAS standard tight and the tighter selection particular to this work are used primarily to separate DY electrons from those fake or

non-isolated electrons coming from inclusive jet events. While reducing a large amount of these background electrons with the tighter selection, a corresponding loss of some of the DY electrons cannot be avoided. The Drell-Yan electron identification efficiency can be calculated with the help of the MC truth information from the MC generator in a way similar to that used for the reconstruction efficiency. First the reconstructed electrons within the acceptance that have matching true electrons from DY processes are chosen. Then, they are tested to see whether they pass the tighter selection criteria. Identification efficiency can then be defined as the ratio of the number of the reconstructed electrons passing the tighter selection to the total number of reconstructed electrons.

In the early stages of the ATLAS experiment, it is important to use real data based techniques without relying on MC to calibrate and to measure the performance of the detector as it will take some time to re-tune the MC algorithms with the understanding of this new energy regime in order to match better the real data. The DY electron identification efficiency can be determined with a data based technique called tag & probe. In the tag & probe method, first a fairly clean (low background) sample of events with two potential electron candidates is chosen. One of these electron candidates must pass the tighter selection criteria in order to reduce the background and is called the tag. The other electron candidate is called the probe and is tested for the tighter selection criteria to determine the identification efficiency. The DY resonances Z, J/ψ and Υ are examined to see if they can be used to select tag & probe pairs, whose invariant masses are within one of these resonances. They will not only provide a low background sample but also the E_{T} and η

distributions of tag and probe electrons will be approximately the same. In other words, the efficiency obtained by just testing one of the pair electrons against the identification criteria shall be the same as testing both. Table 6.1 summarizes the tag & probe selection criteria specific to each resonance.

Selection	J/ψ	Υ	Z
Tag and probe E_{T} greater than [GeV]	7	7	15
η less than [rad] excluding crack	2.5	2.5	2.5
Invariant mass range [GeV,GeV]	[2.1,4.1]	[8,11]	[81,101]
ΔR range between tag & probe [rad]	[0.2,0.4]	[0.5,1.2]	[2.2,4.0]
Probe isolation less than	0.5	0.5	0.3

Table 6.1: Tag & probe method selection criteria specific to each DY resonance.

The tag & probe method selects two types of pairs: those where probes do not satisfy a tighter identification and those where probes do pass the tighter identification. The former happens with a probability of $2\epsilon_{\mathrm{pid}}(1-\epsilon_{\mathrm{pid}})$ where ϵ_{pid} is the DY electron identification efficiency. The latter happens with a probability of $\epsilon^2_{\mathrm{pid}}$. Consequently, the efficiency calculated with the tag & probe is expressed as

$$\epsilon_{\mathrm{tp}} = \frac{\epsilon^2_{\mathrm{pid}}}{\epsilon^2_{\mathrm{pid}} + 2\epsilon_{\mathrm{pid}}(1-\epsilon_{\mathrm{pid}})} = \frac{\epsilon_{\mathrm{pid}}}{2-\epsilon_{\mathrm{pid}}} \tag{6.2}$$

where ϵ_{tp} is the ratio of the number of probes passing the tighter selection to the total number of probes. Figure 6.4 shows a comparison of the DY identification efficiency, ϵ_{pid}, determined using the tag & probe method to MC truth method as a function of electron E_{T} on the left plots and η on the right plots. The results obtained from J/ψ, Υ and Z resonances with 2, 2.6 and 245 pb^{-1} of LHC data respectively are presented from top to bottom. Efficiencies from the tag & probe method using Z and Υ data are consistent with

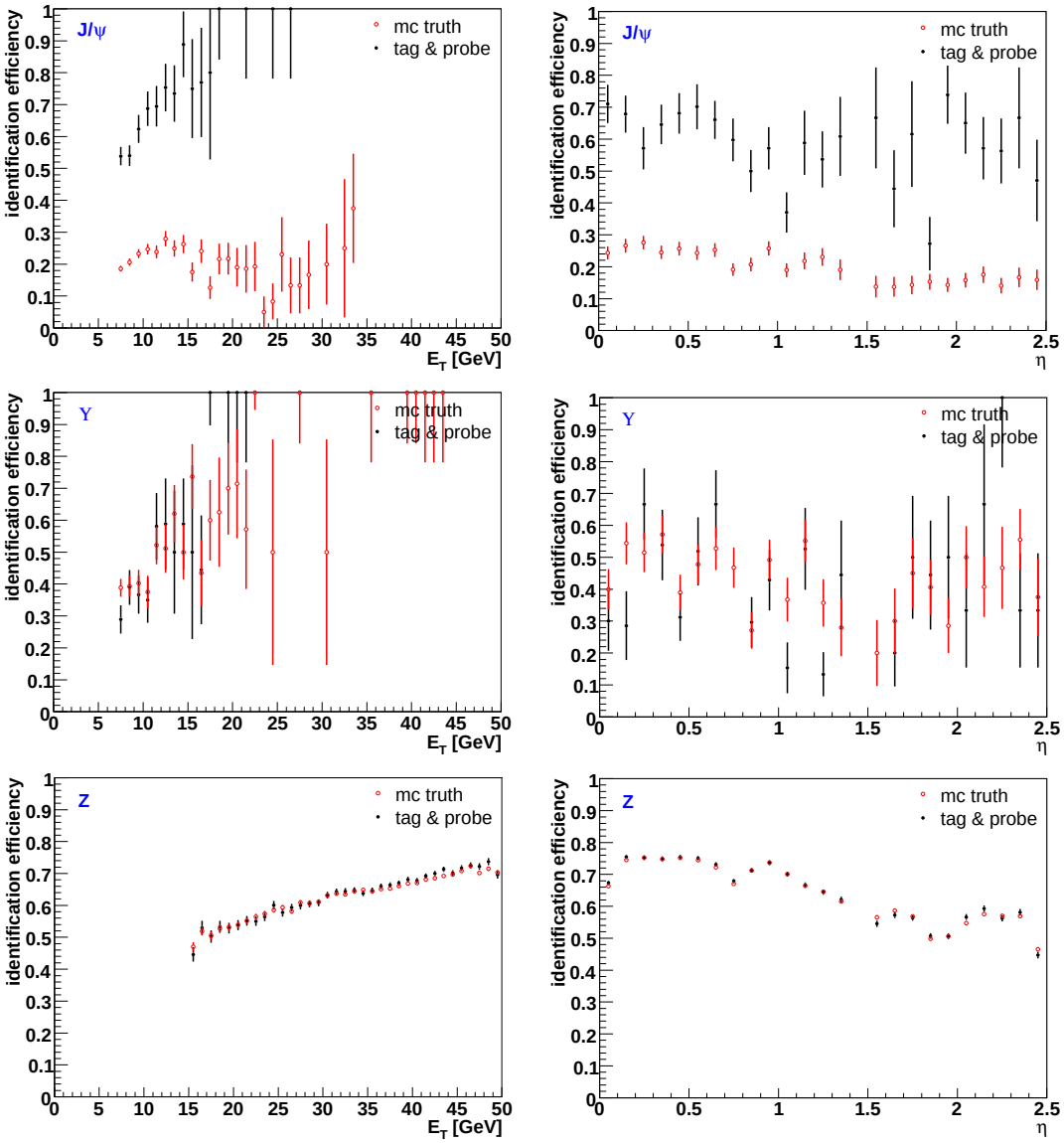

Figure 6.4: Comparison of electron identification efficiency with tag & probe method to MC truth as a function of electron E_{T} on the left and η on the right.

predictions from the MC truth method. There is a clear disagreement in the case of J/ψ data. The tag & probe electrons are geometrically very close to each other in the case of the J/ψ data. Hence, requiring the tag to satisfy the tighter selection with very stringent isolation criteria biases the selected probe to be more likely to satisfy the tighter selection criteria. The bias can be estimated using MC truth. However this would make the tag & probe method MC dependent. Therefore, only Υ and Z resonance data are combined to calculate the identification efficiency in the full E_{T} range of the low mass DY electrons of interest. Figure 6.5 presents the DY electron identification efficiency as a function of electron E_{T} combining the two resonances. The error bars represent 100 pb^{-1} of LHC data,

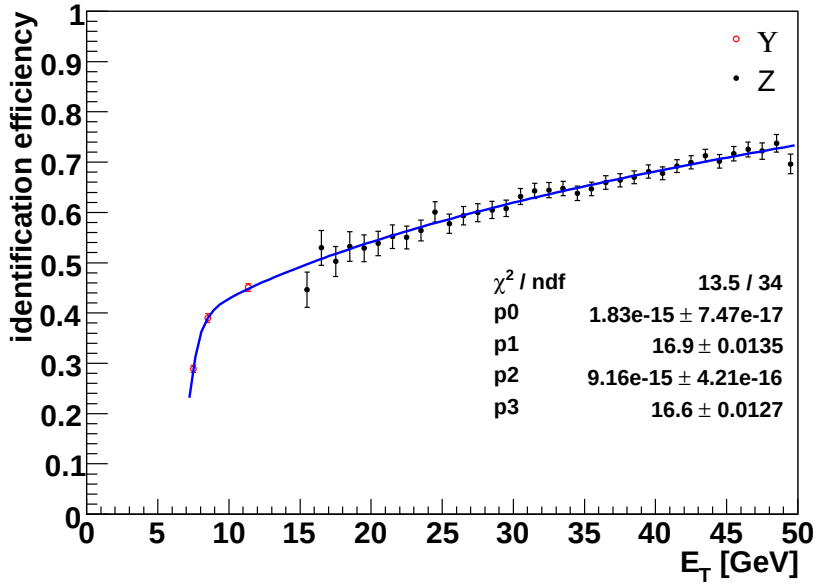

Figure 6.5: Drell-Yan electron identification efficiency as a function of E_{T} with the tag & probe method. Data from Υ and Z resonances are combined to cover the full E_{T} range of DY electrons. Error bars represent 100 pb^{-1} of LHC data.

though the intrinsic fluctuations between data points in each resonance correspond to 2.6

and 245 pb^{-1} for Υ and Z respectively. In the case of the Υ data points, a few E_{T} bins are summed together to have a statistically significant number of probes. The identification efficiency is parametrized as a function of E_{T} with a function of the form as in equation 6.1.

Trigger efficiency can also be calculated using the tag & probe method. In this work, the `2e5` trigger is used. The `2e5` trigger requires two electron candidates each satisfying a single electron trigger, `EF_e5`. Hence, testing whether the probe passing the tighter selection also satisfies the `EF_e5` trigger and squaring the calculated single electron trigger efficiency will give the efficiency for the `2e5` trigger. In the ATLAS trigger system, electron identification begins at the LVL1 trigger with the selection of EM objects using the calorimeter information only with a coarse granularity. The RoIs from these EM objects are then used in the HLT for a finer selection of isolated EM objects using the full granularity of the calorimeters. Finally, an electron is identified if an EM object has an associated track in the inner detector, and then the event is recorded. The selection criteria used in the trigger are much looser than the tighter electron identification used offline as listed in table 5.4. Hence, the trigger efficiency for selecting a DY electron satisfying the tighter selection will be about 100% in the whole E_{T} range except near the trigger E_{T} threshold. The trigger efficiency close to the E_{T} threshold will decrease due to the broader trigger energy resolution. Figure 6.6 presents the `EF_e5` trigger efficiency as a function of E_{T} on the left and η on the right using the MC truth method from the DY signal sample as there was no trigger simulation in the Υ sample on which to use the tag & probe method.

The overall efficiency is calculated by multiplying reconstruction, identification and

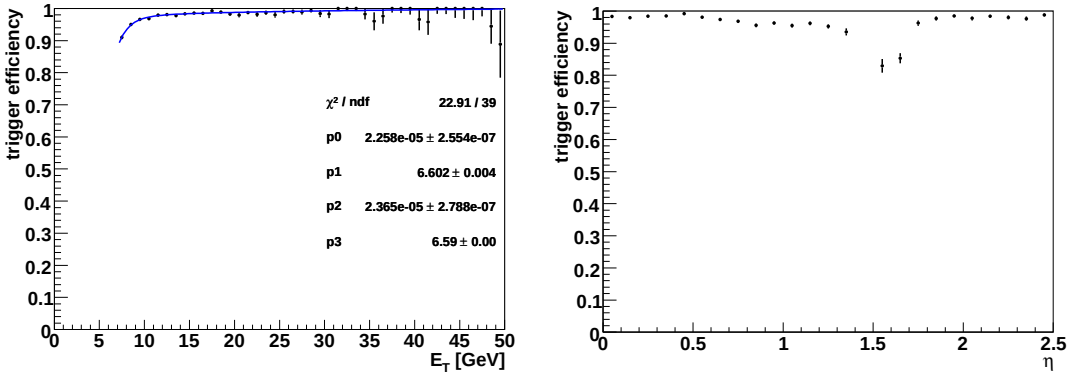

Figure 6.6: `EF_e5` trigger efficiency for Drell-Yan electrons as a function of electron E_{T} on the left and η on the right.

trigger efficiencies for each pair electron as a function of their E_{T} in three η regions: central barrel [0.0,0.8] rad, extended barrel [0.8,1.37] rad and endcap [1.52,2.5] rad. The small Υ sample limited the η binning to three. More binning will be possible with 100 pb^{-1}of LHC data. Figure 6.7 shows the mean overall efficiency as a function of pair invariant mass.

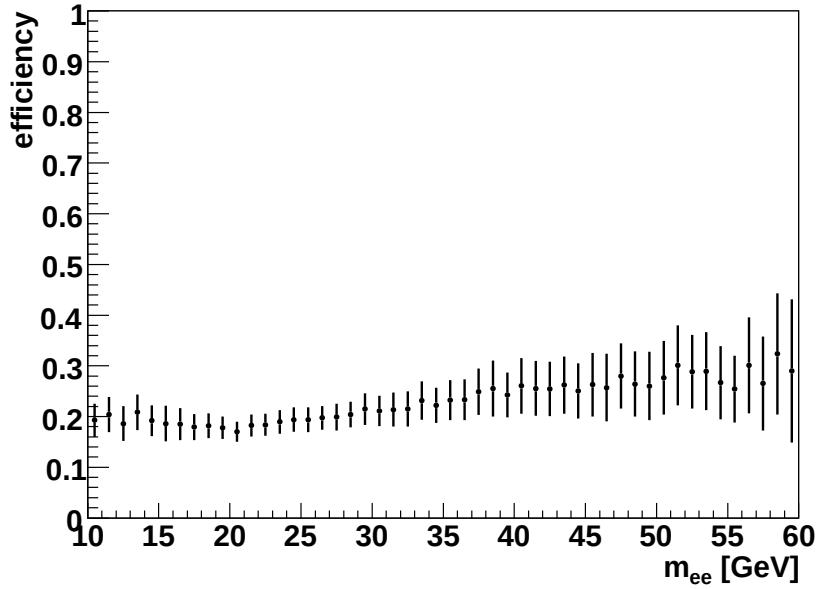

Figure 6.7: Drell-Yan event selection efficiency as a function of pair invariant mass. The error bars represent statistical errors for 100 pb^{-1} of data.

Chapter 7

Calculation of differential cross-section

In this chapter, the calculation of the Drell-Yan differential cross-section is described and the results of this analysis are presented. The uncertainties on the results presented are purely statistical at this point. Systematic uncertainties will be studied in the next chapter.

7.1 Expected spectrum

The expected differential cross-section before corrections, in other words what would be observed, is calculated by normalizing the raw invariant mass distribution of electron pairs shown in figure 5.13 to the corresponding integrated luminosity of the data samples analyzed. The following formula is used:

$$\left(\frac{d\sigma}{dm_{ee}}\right)^{(i)} = \frac{N^{(i)}}{\Delta m_{ee}^{(i)} \mathcal{L}^{(i)}} \tag{7.1}$$

where $\left(\frac{d\sigma}{dm_{ee}}\right)^{(i)}$ is the differential cross-section for bin i. $N^{(i)}$ is the number of electron pairs for bin i. $\Delta m_{ee}^{(i)}$ is the bin width, and $\mathcal{L}^{(i)}$ is the integrated luminosity of the data sample.

Differential cross-sections calculated for Drell-Yan signal and background processes are presented in figure 7.1. The total measured cross-section of all electron pairs including

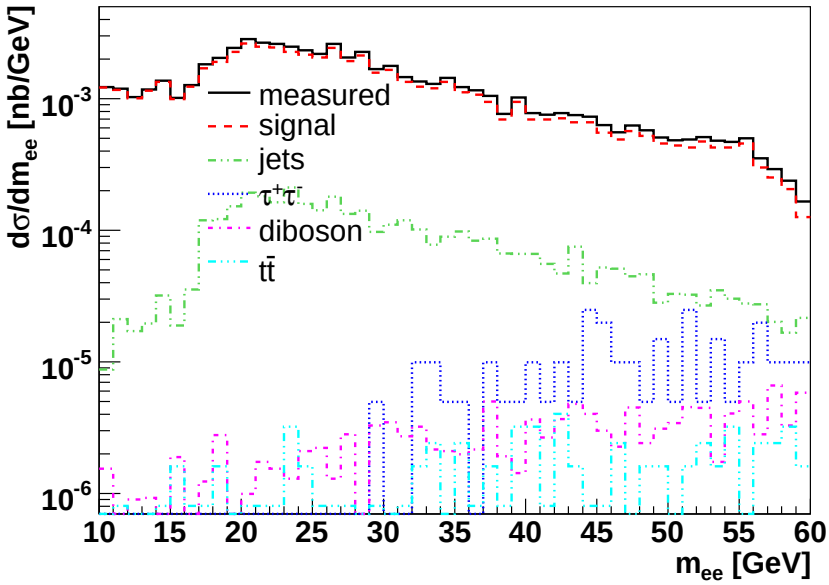

Figure 7.1: Measured Drell-Yan differential cross-section before corrections as a function of pair invariant mass. The solid-lined distribution represents the sum of the signal and all background species.

background for the selection criteria listed in table 5.4 is (63.6 ± 1.1) pb for the invariant mass range between 10 GeV and 60 GeV. It is expected that the Drell-Yan cross-section is 93% of the total.

Figure 7.2 presents the differential cross-sections as a function of p_{T} of the electron pair on the top plot and rapidity on the bottom plot. At higher p_{T}, the amount of inclusive jet background decreases relative to the Drell-Yan signal. The main reason for this is the exponential decrease in inclusive jet events with higher p_{T} whereas the decrease in the Drell-Yan signal follows a power law.

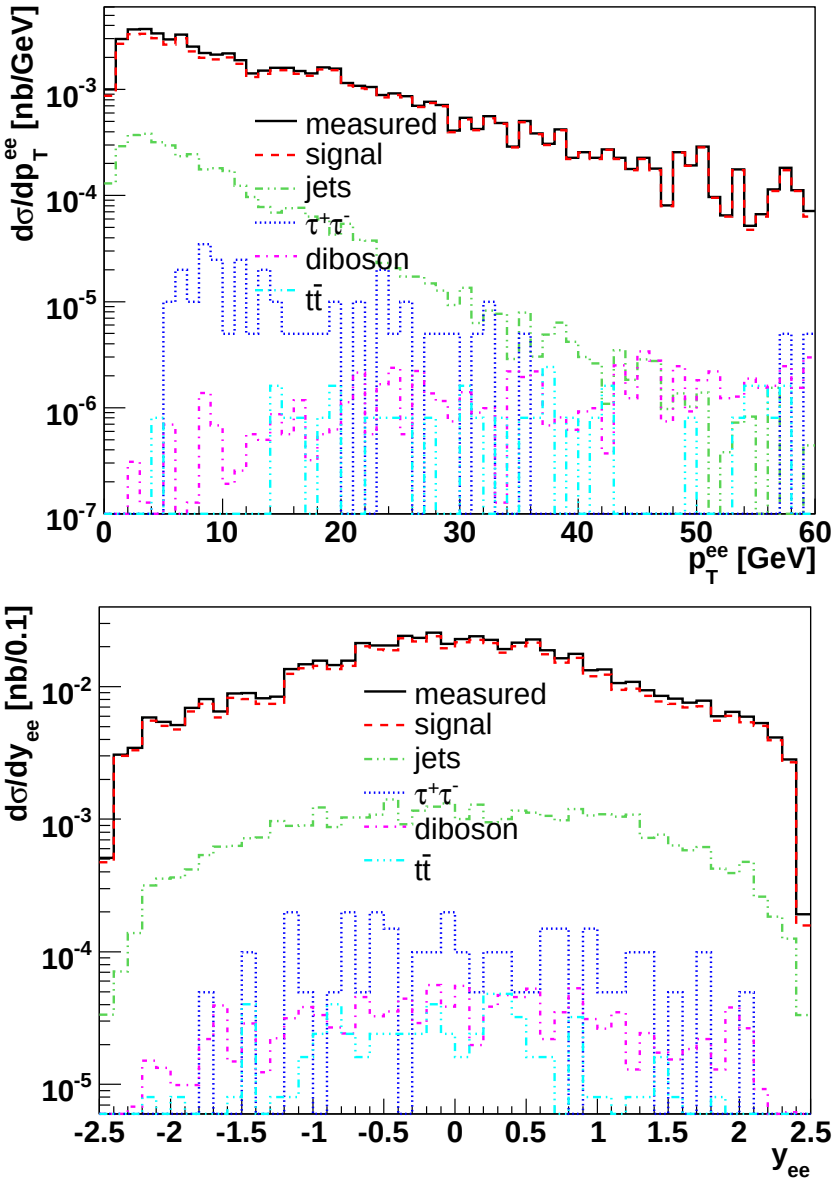

Figure 7.2: Measured Drell-Yan differential cross-section before corrections as a function of transverse momentum of the electron pair on the top plot and rapidity of the pair on the bottom plot. The solid-lined distribution represents the sum of the signal and all background species.

7.2 Corrected spectrum

In order to calculate the Drell-Yan differential cross-section, the measured differential cross-section of all electron pairs is corrected in three steps. First the estimated background is subtracted. Then, the background subtracted differential cross-section is corrected for the detection efficiency of Drell-Yan signal electrons determined in section 6.2. Finally, the background subtracted and efficiency corrected differential cross-section is corrected for the acceptance of DY electrons obtained in section 6.1. The formula used is as follows

$$\left(\frac{d\sigma}{dm_{ee}}\right)^{(i)}_{\mathrm{DY}} = \left[\left(\frac{d\sigma}{dm_{ee}}\right)^{(i)}_{\mathrm{meas}} - \left(\frac{d\sigma}{dm_{ee}}\right)^{(i)}_{\mathrm{bkg}}\right] / \left[\epsilon_i A_i\right] \tag{7.2}$$

where $\left(\frac{d\sigma}{dm_{ee}}\right)^{(i)}_{\mathrm{DY}}$ is the corrected Drell-Yan differential cross-section for bin i. $\left(\frac{d\sigma}{dm_{ee}}\right)^{(i)}_{\mathrm{meas}}$ is the measured differential cross-section of all electron pairs including background, and $\left(\frac{d\sigma}{dm_{ee}}\right)^{(i)}_{\mathrm{bkg}}$ is the measured differential cross-section of all background electron pairs for bin i. A_i and ϵ_i are the acceptance and efficiency for bin i, respectively.

Each correction step is displayed in figure 7.3 starting from the measured differential cross-section shown as the shaded-circles with error bars. The background subtracted distribution is shown as the unshaded-circles with error bars. The shaded-triangles with error bars present the background subtracted and efficiency corrected differential cross-section. The fully corrected, including acceptance, Drell-Yan differential cross-section is shown as the unshaded-triangles with error bars. The solid-lined distribution represents the theoretical expectation. All of the error bars are statistical and represent 100 pb^{-1} equivalent LHC data, though the intrinsic fluctuations between bins are mainly due to the 63 pb^{-1}

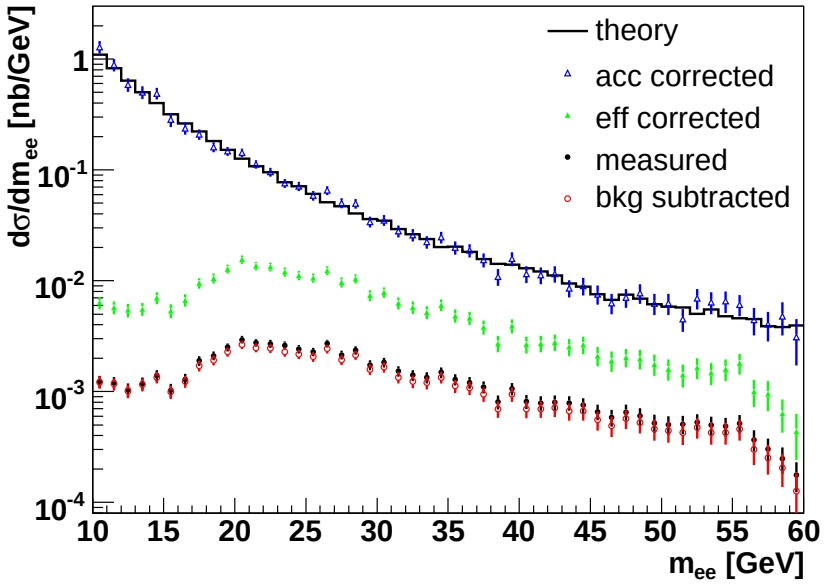

Figure 7.3: Corrected Drell-Yan differential cross-section as a function of pair invariant mass. The solid-lined distribution represents the theoretical expectation.

equivalent Drell-Yan signal sample used for this analysis. The corrected distribution agrees well with the theoretical expectation.

The total corrected Drell-Yan cross-section is (5.90 ± 0.24) nb for the invariant mass range between 10 GeV and 60 GeV. The quoted uncertainty of 4.1% is statistical. Potential systematic uncertainties are studied in chapter 8.

Figure 7.4 presents the corrected DY differential cross-section as a function of p_{T} of the electron in the top plot and rapidity in the bottom plot. It is clear from the differential cross-section as a function of rapidity plot that the acceptance and efficiency corrections need to be calculated for more η bins than the three (barrel, extended barrel and endcap) used in chapter 6 as the amount of dead material in front of the EM calorimeter varies more with increasing η. More binning in η was not possible with the 2.6 pb^{-1} Υ sample.

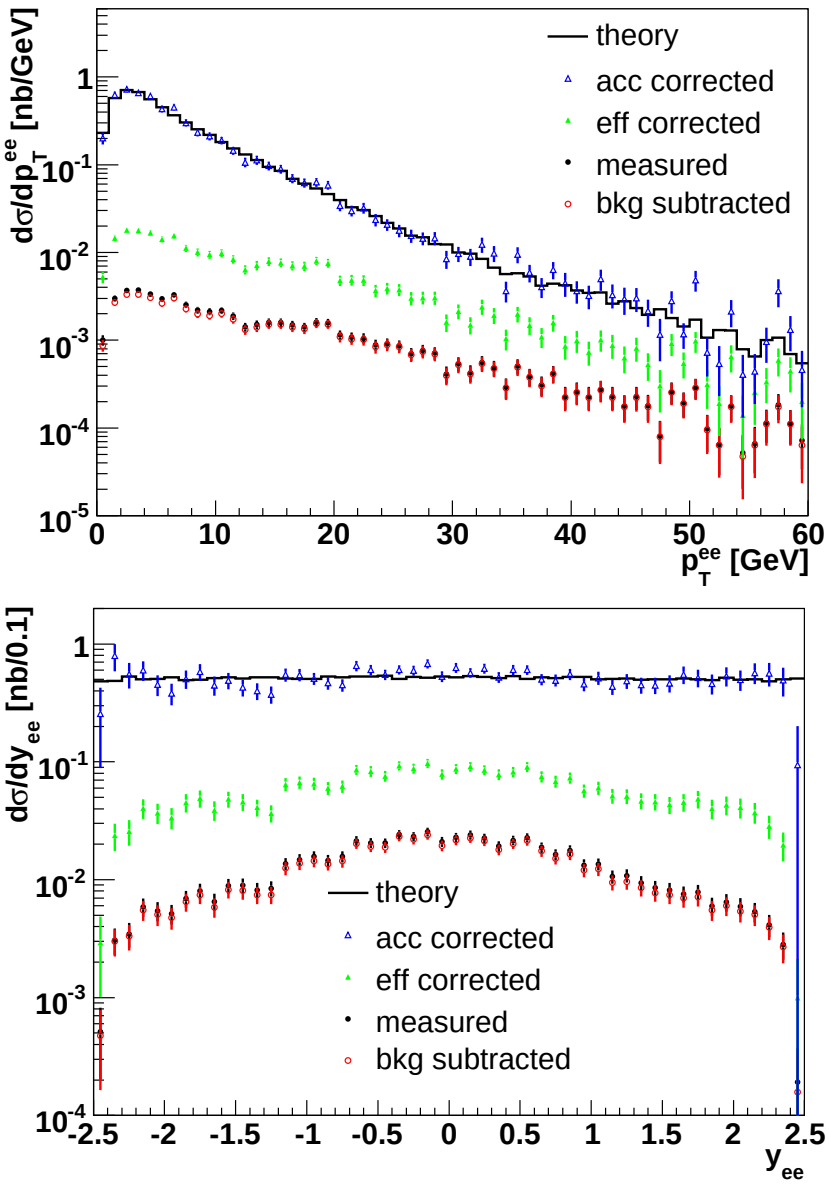

Figure 7.4: Corrected Drell-Yan differential cross-section as a function of pair transverse momentum on the top plot and y_{ee} on the bottom plot. The solid-lined distribution represents the theoretical expectation.

Chapter 8

Assessment of systematic uncertainties

In this chapter, the potential sources of systematic uncertainties are studied. The systematics considered are those affecting the calculation of the acceptance and efficiency, and the estimation of the inclusive jet background.

8.1 Acceptance uncertainty

The main source of uncertainty on the calculation of the acceptance correction to the differential cross-section is due to the uncertainty on the PDFs used in the event generation. A detailed description of PDF uncertainty determination can be found in [47] and [48]. CTEQ PDFs are used in the ATLAS MC production. The CTEQ group provides 40 eigenvector PDF sets along with a best-fit set for studies of PDF uncertainty. These eigenvector sets are also called the PDF error sets. CTEQ uses the Hessian method to assess the uncertainties on the PDFs. In version CTEQ6, the global data used for PDF determination is fit with 20 free parameters, a_i, and minimizing the χ^2 of the fit yields a best fit which is called the

central PDF set, S_0. Then, the change in the global χ^2, $\Delta\chi^2$, is given by

$$\Delta\chi^2 = \sum_{i}^{N}\sum_{j}^{N} H_{ij}(a_i - a_i^0)(a_j - a_j^0) \tag{8.1}$$

where H_{ij} is the Hessian error matrix, the superscript zero denotes the central value, and N is equal to 20 in the case of CTEQ6. The matrix is diagonalized to get 20 eigenvectors each of which probes a direction in the PDF parameter space. The eigenvectors are numbered from highest to lowest eigenvalue. Highest eigenvalues correspond to the best determined directions. Each eigenvector is varied up and down to get 40 new parameter sets, $S_i^{\pm}$, that can be used for uncertainty analysis.

In order to estimate the acceptance uncertainty on the Drell-Yan cross-section due to the choice of PDF parametrization, the CTEQ6.1M central set and the first 20 of the associated error sets are used. With each of the 21 PDF sets, 2×10^5 low mass Drell-Yan events corresponding to 36 pb^{-1} of LHC data in the invariant mass range 10 GeV to 60 GeV are generated using PYTHIA. Figure 8.1 shows the Drell-Yan differential cross-section within the acceptance, determined using these 21 different PDF sets on the top plot. The error bars are statistical. The bottom plot presents the spread of the differential cross-sections obtained using 20 error sets from the one obtained using the central PDF set. The average spread is 13.7%. The acceptance systematic uncertainty on the total cross-section between 10 GeV to 60 GeV invariant mass is 2.4%.

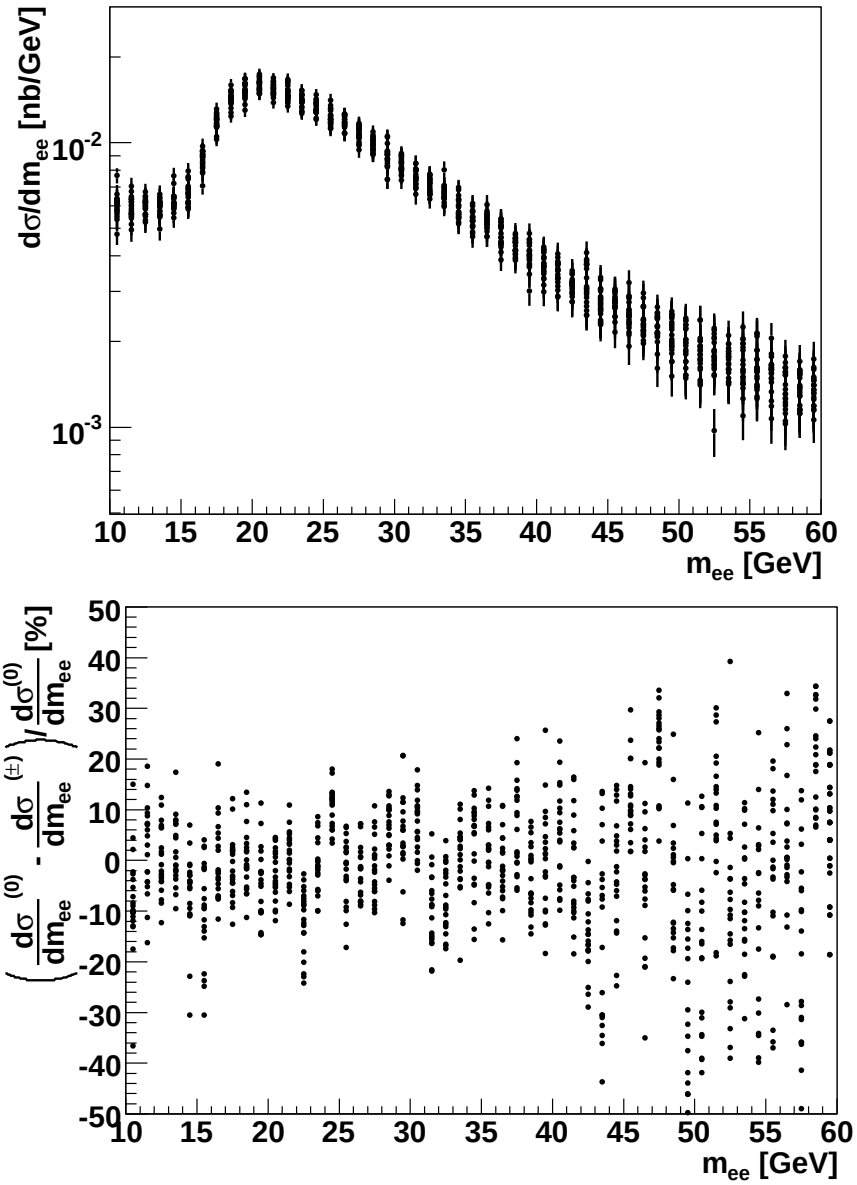

Figure 8.1: Acceptance uncertainty on the Drell-Yan spectrum.

8.2 Efficiency uncertainty

The largest efficiency correction comes from electron identification. As described in section 6.2, the electron identification efficiency is calculated with the tag & probe method. This method can introduce bias for two main reasons compared to, for instance, the conventional MC method used to calculate the reconstruction efficiency. The first is due to the fact that the tag electron is more likely to be identified in an η region where the efficiency is higher, and therefore the probe electron naturally may be found in η where the efficiency is lower as it is highly correlated with the tag electron. Figure 8.2 illustrates a comparison of η distributions of the tag and probe electron candidates from the Z boson sample. The two

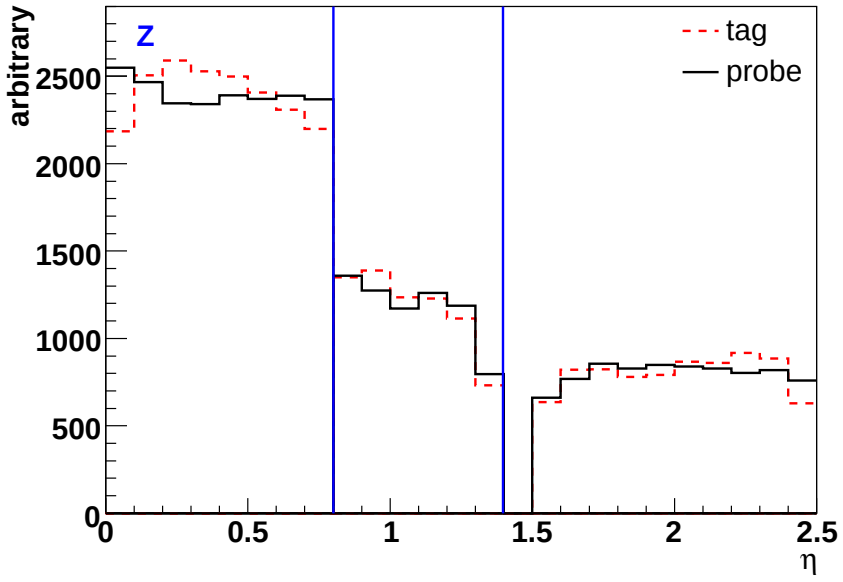

Figure 8.2: Comparison of η distributions of the tag and probe electron candidates. The two solid vertical lines separate the η regions at which the identification efficiency is calculated.

solid vertical lines separate the η regions for which the identification efficiency is calculated.

Taking the central barrel region, $|\eta| < 0.8$, for example, the tag electron candidates are selected more from the middle of this region and hence pushing the probes to be selected more from the edges. The middle region, where the tags are selected, is where the efficiency is higher in this central barrel region as is shown on the bottom right plot of the figure 6.4. Since the identification efficiency is calculated as a function of E_{T} of the electron candidates and integrated over the η range of this region, the bias in selecting probes in the less efficient η region causes an under-estimation of the efficiency for a particular electron candidate E_{T}. Similar behaviour can be observed in the extended barrel and the endcap regions as well. The second reason for a bias is the fact that there will be background electron pairs in the tag & probe sample used for efficiency calculation. Figure 8.3 shows the invariant mass distribution of tag & probe pairs in the range 1 GeV and 110 GeV where for the purpose of illustration, the tag & probe selection criteria from the Υ resonance, presented in table 6.1 with the exception of ΔR and invariant mass cuts, are used for all data samples including the inclusive jet background and the Z boson resonance. As can be seen in the plot, the signal tag & probe pairs dominate at the resonances compared to the background, though the background is still significant. Away from the resonances, the background is about an order of magnitude higher than the signal. Consequently, the amount of background under the resonance peaks can be estimated using the regions where the background dominates. For instance, fitting an exponential function in the invariant mass region 12 GeV to 18 GeV and using this function to estimate the background under the Υ peak yields a result accurate within 5% of the actual background which means an underestimate of the background

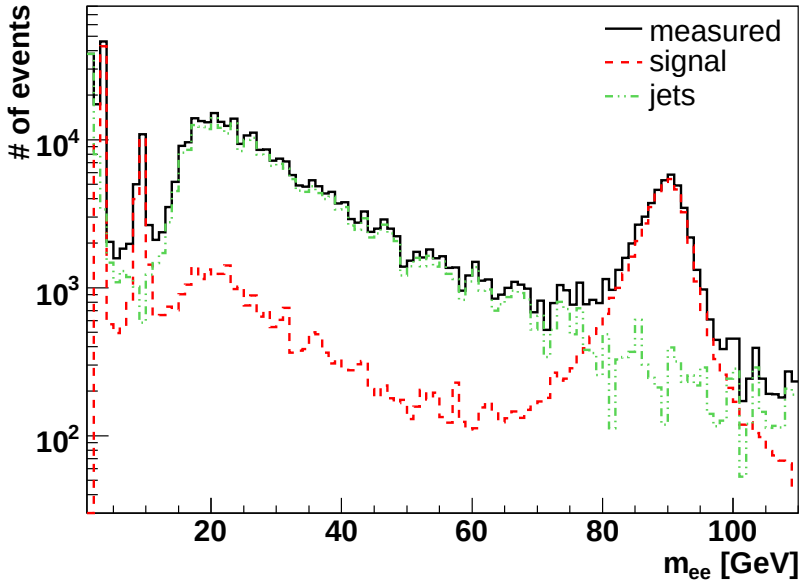

Figure 8.3: Drell-Yan resonances and background for the tag & probe method.

of about 1%.

In order to simulate the degradation effect of background in the efficiency calculation and compare the tag & probe method with the conventional MC method, the total number of probes is increased by 1% for the Υ data and 0.5% for the Z data. In other words, the denominator of equation 6.2 is increased without changing the numerator as the efficiency of background probes passing the tighter identification criteria is negligibly small relative to the signal probes. Figure 8.4 shows the comparison of the corrected Drell-Yan differential cross-section using the efficiency calculated with the tag & probe method from Υ and Z samples to the differential cross-section corrected using the efficiency calculated with the MC method from the Drell-Yan signal sample in the top plot. The error bars are statistical. The bottom plot shows the spread of the tag & probe method result with respect to the one

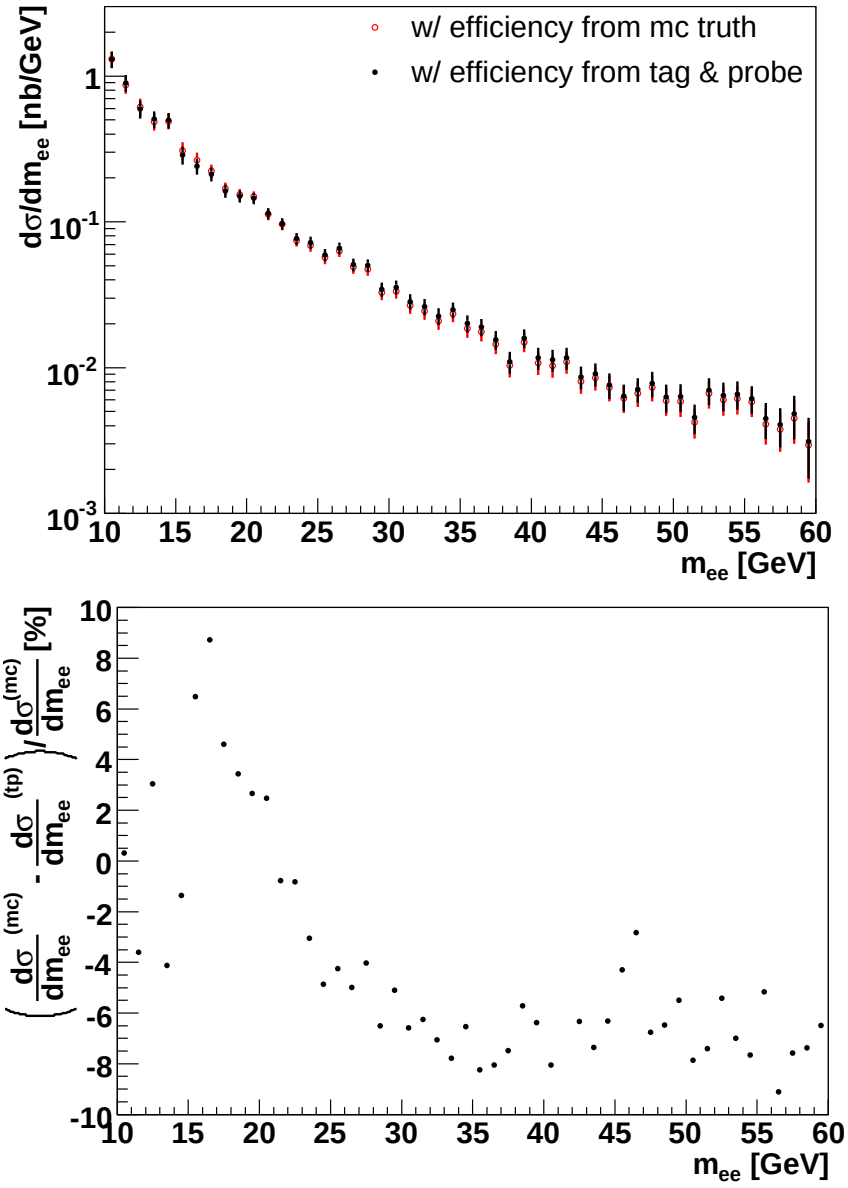

Figure 8.4: Efficiency uncertainty on the Drell-Yan spectrum.

from the MC method. The average spread is 6.1%. The negative spread at higher invariant masses well above the E_{T} threshold means the tag & probe method under-estimates the efficiency, which results in an over-correction of the differential cross-section. Both reasons for bias described in the first paragraph of this section lead to such an under-estimation of the efficiency. The bias on the probe η distribution causes most of this spread. The positive spread at lower invariant masses is largely due to the very small, 2.6 pb^{-1}, Υ sample allowing for only three bins in η and three bins in electron E_{T} between 8 GeV and 15 GeV for the calculation of efficiency. 100 pb^{-1} equivalent LHC data will allow for more binning and hence for a more precise calculation of the efficiency using the tag & probe method. In other words, the spread will be reduced significantly with 100 pb^{-1} of data. The efficiency systematic uncertainty on the total cross-section between 10 GeV to 60 GeV invariant mass is 0.2%.

8.3 QCD background uncertainty

The estimation of the inclusive jet background is explained in detail in section 5.5. The lack of enough inclusive jet MC data did not allow for a more accurate DY-like di-electron analysis of the background. Instead, an estimation of the jet background is made relying on information obtained from single electrons. The systematic uncertainties on the cross-section arising from the estimation of the inclusive jet background are investigated separately for the normalization and shape of the background.

The uncertainty on the estimated probability of finding a pair of electrons satisfying the tighter selection listed on table 5.4 in an inclusive jet event is calculated to be 22%.

In order to determine the systematic uncertainty on the cross-section, the inclusive jet background is assumed to be over or under-estimated by 22% and subtracted from the measured distribution. The top plot in figure 8.5 shows the comparison of the corrected Drell-Yan differential cross-section assuming a perfect estimation of the jet background to the cases where over or under-estimation occurs. The bottom plot shows the spread of the results from over or under-estimation of the background with respect to the perfect estimation. The average spread is 2.5%. The jet background normalization systematic uncertainty on the total cross-section between 10 GeV to 60 GeV invariant mass is 1.5%.

The shape of the inclusive jet background is estimated by re-weighting the base invariant mass distribution of all jet background electrons within acceptance before any of the identification cuts are applied. The weights are obtained as a function of the electron E_{T} from the efficiency of the jet background electrons passing the tighter identification as a function of their E_{T}. The assumption is that the shape of the invariant mass distribution of the jet background electrons within acceptance will change once the tighter identification is applied since the tighter identification efficiency on the background electrons varies with η. This assumption is validated for the case of loose identification and the actual shape of the invariant mass distribution of the loose background electrons could be estimated with this re-weighting technique. Although it is reasonable to assume such a re-weighting technique can be used to estimate the shape of the background after tighter selection, there is no way of validating such an assumption due to the lack of enough MC data with a DY-like di-electron analysis. Therefore, the systematic uncertainty on the cross-section that may arise

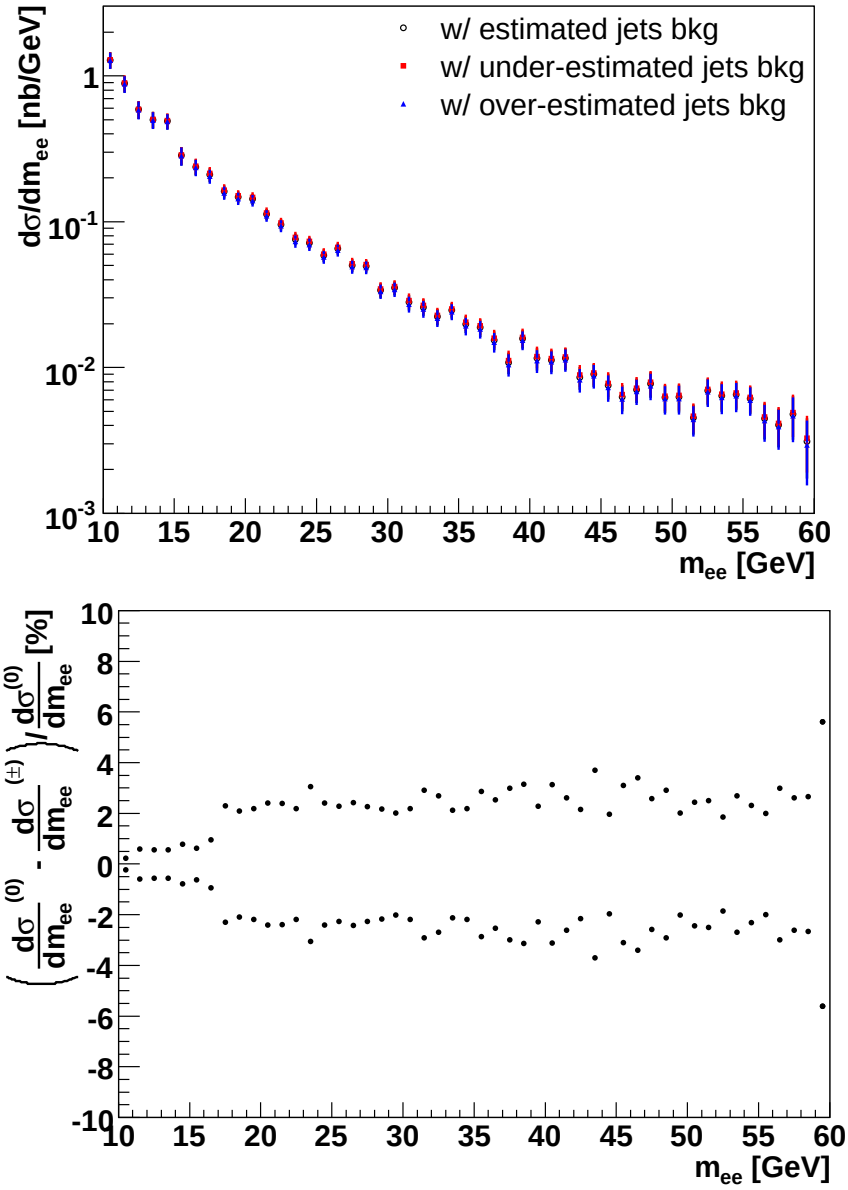

Figure 8.5: Jet background normalization uncertainty on the Drell-Yan spectrum.

from this shape is studied by comparing the corrected differential cross-section including an estimation and subtraction of the jet background for which the shape is obtained with this re-weighting technique to the one where the shape of the background is assumed to be the same as the base distribution before tighter selection so that the reweighting is not applied. Figure 8.6 presents such a comparison in the top plot. The bottom plot shows the spread of the result without reweighting from the result with reweighting. The average spread is 3.5%. This uncertainty will be reduced as it is common for particle physics experiments to produce nearly as much MC data as the experimental data collected, and therefore the shape of the background will be determined more accurately. The jet background shape systematic uncertainty on the total cross-section between 10 GeV to 60 GeV invariant mass is 0.5%.

Consequently, the overall jet background systematic uncertainty on the total cross-section between 10 GeV to 60 GeV invariant mass is 2.0% which is the sum of the shape and normalization uncertainties since the two are correlated.

A summary of statistical and all systematic uncertainties studied is provided at the beginning of the discussion chapter that follows.

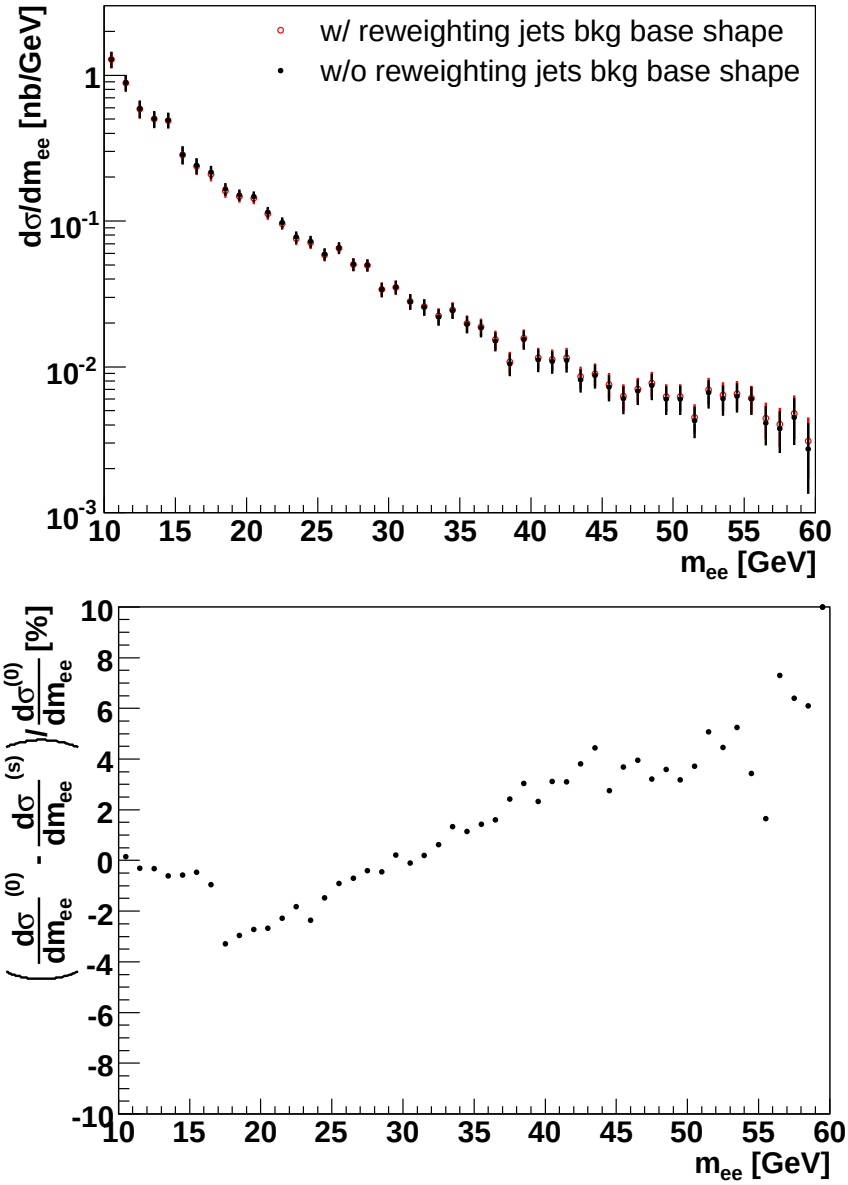

Figure 8.6: Jet background shape uncertainty on the Drell-Yan spectrum.

Chapter 9

Discussion

The analysis performed assuming 100 pb^{-1} of LHC data has yielded a total cross-section of 5.90 nb for the Drell-Yan electron pair invariant mass range of 10 GeV to 60 GeV. The statistical and systematic uncertainties on the total cross-section are listed on table 9.1. The total

Source	Uncertainty [%]
Statistical	4.1
Acceptance	2.4
Efficiency	0.2
Inclusive jets	2.0
Total systematic	3.1
Total statistical and systematic	5.1

Table 9.1: Summary of uncertainties on the total Drell-Yan cross-section in the 10 GeV to 60 GeV invariant mass range for 100 pb^{-1} LHC data.

systematic and statistical uncertainty is obtained by adding the individual uncertainties in quadrature.

In this chapter, comparison of the results of this analysis with the current theoretical predictions and the measurements from previous experiments is provided, followed by a discussion on the proposed set of low E_T Drell-Yan electron identification variables for the

early data taking at the LHC.

9.1 PDF uncertainty on the cross-section

The DY cross-section is the convolution of the parton level cross-section and PDFs as can be seen in the formulae given in section 2.2.2. The uncertainty on the cross-section mainly comes from the uncertainty on the PDFs. The determination of the PDF uncertainty is explained briefly in section 8.1. In order to calculate the uncertainty on any physical observable, X, due to the uncertainties on the PDFs, the CTEQ group suggests the use of the following master formulae

$$\Delta X^{+}_{\max} = \sqrt{\sum_{i=1}^{N} \max\left(X_i^{+} - X_0, X_i^{-} - X_0, 0\right)^2} \tag{9.1}$$

$$\Delta X^{-}_{\max} = \sqrt{\sum_{i=1}^{N} \max\left(X_0 - X_i^{+}, X_0 - X_i^{-}, 0\right)^2} \tag{9.2}$$

where N is the number of free parameters and is equal to 20 in the case of CTEQ6. X_i^{+} and X_i^{-} are the values of the observable X calculated using the positive and negative PDF error sets respectively from the i^{th} direction of the PDF parameter space. X_0 is the value of the observable X calculated using the central PDF set.

In this work, the observable X is the Drell-Yan cross-section that can be obtained using the LO differential cross-section equation 2.30 and integrating over the pair invariant mass range of interest. The accuracy of the cross-section equation is validated by comparing with the differential cross-section from the PYTHIA event generator using the same PDF set as shown on figure 9.1. The solid-lined curve is obtained using the cross-section equation. Good agreement between PYTHIA and the theoretical calculation shows that cross-sections

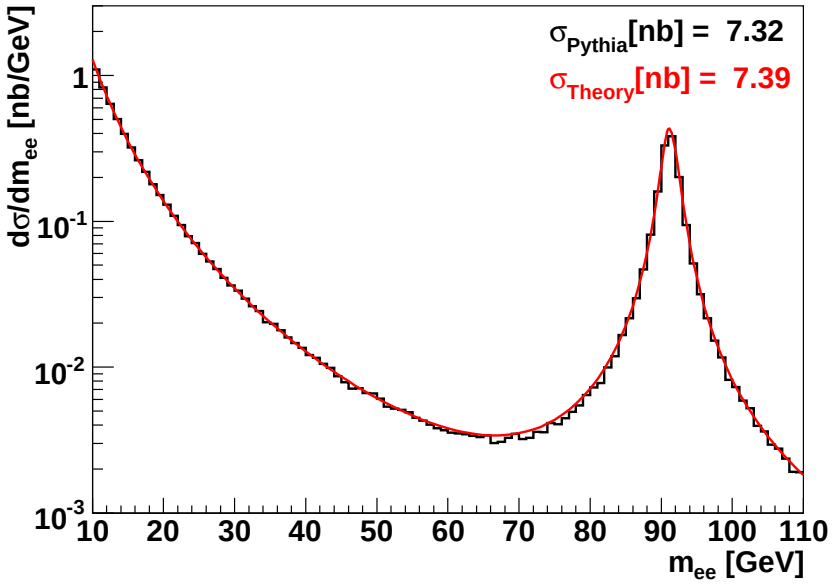

Figure 9.1: Drell-Yan differential cross-section as a function of the electron pair invariant mass assuming a perfect detection efficiency and acceptance. The solid-lined curve is a theoretical calculation using the LO formulae in section 2.2.2.

are calculated to the LO in PYTHIA.

Using the master formulae and the cross-section equation along with the CTEQ6.1M central and 40 associated PDF sets, the larger of the asymmetric uncertainties on the total Drell-Yan cross-section in the invariant mass range between 10 GeV and 60 GeV is found to be 7.6%.

With the 7.6% theoretical uncertainty on the total Drell-Yan cross-section at low mass and the overall expected measurement uncertainty of 5.1%, 100 pb^{-1} of LHC data already seems to be enough to begin constraining the PDFs and reducing their uncertainties.

9.2 Comparison with the previous measurements

Experiments at the Fermilab TEVATRON [49], currently the highest energy accelerator colliding beams of protons and anti-protons at a centre of mass energy of 1.96 TeV, provide previous measurements comparable to this work. Measurements of Drell-Yan differential cross-sections for invariant masses above 11 GeV and 40 GeV are reported in [50] and [51], respectively. The reference [50] uses about 85 pb^{-1}, while the reference [51] uses 108 pb^{-1} of TEVATRON data taken at 1.8 TeV centre of mass energy.

For the invariant mass range of 11 GeV to 15 GeV, the reference [50] presents a statistical uncertainty of 12.1%, a systematic uncertainty of 27.1% and a total uncertainty of 29.7% on the Drell-Yan cross-section. For the same invariant mass range with 100 pb^{-1} of LHC data, a statistical uncertainty of 6.8%, a systematic uncertainty of 5.1% and a total uncertainty of 8.5% on the cross-section are expected.

For the invariant mass range of 20 GeV to 30 GeV, reference [50] presents a statistical uncertainty of 5.4%, a systematic uncertainty of 8.5% and a total uncertainty of 10.1% on the Drell-Yan cross-section. For the same invariant mass range with 100 pb^{-1} of LHC data, a statistical uncertainty of 3.1%, a systematic uncertainty of 5.9% and a total uncertainty of 6.7% on the cross-section are expected.

For the invariant mass range of 40 GeV to 50 GeV, reference [51] presents a total uncertainty of 20.4% on the Drell-Yan cross-section. For the same invariant mass range with 100 pb^{-1} of LHC data, a total uncertainty of 12.3% on the cross-section is expected.

The higher centre of mass energy of the LHC means a larger Drell-Yan cross-section

which in turn will result in many more Drell-Yan events for the same integrated luminosities compared to the TEVATRON. Therefore, statistical uncertainties on the measurement of the Drell-Yan spectrum will be reduced significantly at LHC and should help reduce the systematic uncertainties. More importantly, at the TEVATRON centre of mass energies, the proton structure is probed down to a momentum fraction of about 2×10^{-2}, whereas it will be probed down to about 10^{-4} at the LHC.

9.3 Drell-Yan electron identification for early running

The ATLAS standard tight electron identification has quite a few cuts applied in 42 different E_{T} and η bins as discussed in section 5.3. Each of these variables will have to be studied thoroughly and optimized in each bin. Understanding the systematics and optimization of each of these variables in each E_{T} and η bin will require a statistically significant number of electrons. Such study and optimization will take time and require on the order of a few 10 pb^{-1} of LHC data. Therefore, for the early LHC operation, a small subset of the standard tight identification variables most relevant for the identification of the low E_{T} Drell-Yan electrons is studied in addition to the three additional tighter selection variables used to further reduce the inclusive jet background as explained in section 5.6.

In order to select four of the standard tight selection variables, the signal and inclusive jet background electrons passing the tighter ClusterIsolation, TrackA0 and PtRelJetAxis variables are used to calculate the discrimination power of the remaining standard tight identification variables. The TrackTRTratio, TrackMatchEoverP, TrackMatchEta and ClusterStripsWtot are found to be the most discriminating. These four variables are op-

timized in two η bins, namely barrel and endcap as is done for ClusterIsolation, TrackA0 and PtRelJetAxis. Table 9.2 presents the optimized cut values for each bin for each of the identification variables proposed to be used during the early data taking at the LHC. These

Identification variable	Cut values
ClusterIsolation	{0.12,0.12}
TrackA0	{0.09,0.15} mm
PtRelJetAxis	{3.5,3.5} GeV
TrackTRTratio	{0.09,0.11}
TrackMatchEoverP	min:{0.9,1.0} and max:{1.5,2.0}
TrackMatchEta	{0.0023,0.0023}
ClusterStripsWtot	{2.9,3.1}

Table 9.2: Low E_{T} Drell-Yan electron identification variables for early running period of the LHC. Cut values are presented for barrel, $|\eta| < 1.37$, and endcap, $|\eta| > 1.52$, within the ATLAS tracking region, $|\eta| < 2.5$. TrackTRTratio is only applied up to the TRT coverage, $|\eta| < 2.0$.

seven cuts applied only in two η bins achieves the same signal to background ratio as on table 5.4 using the combination all of the ATLAS standard electron identification and the three tighter identification variables.

Chapter 10

Conclusions

The structure of the proton is parametrized with the Parton Distribution Functions (PDFs). The PDFs are best determined experimentally and are used to calculate cross-sections or in other words the likelihood of observed physical processes, which are crucial in exploiting the discovery potential of the Large Hadron Collider (LHC), the highest energy accelerator ever built that will begin operation in late 2009.

Drell-Yan (DY) is a well understood process involving the annihilation of a quark from one hadron with an anti-quark from another hadron producing an oppositely charged lepton pair, and hence it probes a well defined initial state. The charged leptons, electrons and muons specifically, are the most readily detected and arguably the best measured particles at ATLAS. The DY process therefore has significant practical experimental advantages to understand the performance of and to calibrate the ATLAS detector, and will play an essential role in many of the physics goals envisioned at the LHC. Examples of such physics goals are precision measurements of the Standard Model (SM), discovery of the only unobserved particle predicted by the SM, the Higgs boson, and understanding the electroweak

symmetry breaking process.

This dissertation has studied the prospects for measuring the DY spectrum in the 10 GeV to 60 GeV low invariant mass range using e^+e^- pairs from the initial LHC data in order to further constrain the PDFs. In this invariant mass range, the proton structure is probed down to about 10^{-4} in momentum fractions carried by partons.

The analysis is based on the full Monte Carlo simulation of the ATLAS detector response to signal (DY) electrons and background (inclusive jets, $\tau^+\tau^-$, di-boson and $t\bar{t}$) processes.

The total Drell-Yan cross-section in the invariant mass range 10 GeV to 60 GeV is expected to be

$$\sigma_{\mathrm{DY}} = 5.90 \pm 0.24(\mathrm{stat}) \pm 0.18(\mathrm{syst})\ \mathrm{nb}$$

where the statistical uncertainty represents an assumed data sample of 100 pb^{-1} which the LHC is capable of delivering in less than a week at a moderate luminosity of 10^{33} $\mathrm{cm}^{-2}\mathrm{s}^{-1}$. The systematic uncertainties come from the PDF uncertainty on the acceptance, the tag & probe method uncertainty on the efficiency, and the uncertainty on the estimation of the inclusive jet background. The result corresponds to an overall uncertainty of 5.1% when the statistical and systematic uncertainties are added in quadrature. In comparison to the current theoretical uncertainty of 7.6% in the same invariant mass region and the previous measurements from the TEVATRON, currently the highest energy accelerator in operation, the results indicate that the PDF uncertainties can be reduced and hence the proton structure can be further constrained with as little as 100 pb^{-1} of LHC data.

References

[1] The LHC Study Group, *Design Study of the Large Hadron Collider*, CERN-91-03, 1991. 1

[2] DSU - Communication Group, 2007, *CERN's Flagship Project: The LHC*, http://public.web.cern.ch/Public/Welcome.html 1

[3] D. J. Griffiths, *Introduction to Elementary Particles*, John Wiley & Sons Inc., 1987. 1

[4] D. H. Perkins, *Introduction to High-Energy Physics*, 4$^{\text{th}}$ Edition Reprint, Cambridge University Press, 2001. 1

[5] F. Halzen, A. D. Martin,*Quarks & Leptons: An Introductory Course in Modern Particle Physics*, John Wiley & Sons Inc., 1984. 1

[6] E. Eichten, I. Hinchliffe, K. Lane, C. Quigg, *Supercollider Physics*, Reviews of Modern Physics, Volume 56 No 4 (p579-p707), 1984.

E. Eichten, I. Hinchliffe, K. Lane, C. Quigg, *Erratum: Supercollider Physics [Rev. Mod. Phys. 56, 579 (1984)]*, Reviews of Modern Physics, Volume 58 No 4 (p1065-p1073), 1986. 1, 21

[7] S. D. Drell, T. M. Yan, *Massive Lepton-Pair Production in Hadron-Hadron Collisions at High Energies*, Physical Review Letters, Volume 25 No 5 (p316-p320), 1970. 2

[8] J. J. Aubert et al, *Experimental Observation of a Heavy Particle J*, Physical Review Letters, Volume 33 No 23 (p1404-p1406), 1974.

J.-E. Augustin et al, *Discovery of a Narrow Resonance in e^+e^- Annihilation*, Physical Review Letters, Volume 33 No 23 (p1406-p1408), 1974. 2

[9] S. W. Herb et al, *Observation of a Dimuon Resonance at 9.5 GeV in 400 GeV Proton-Nucleus Collisions*, FERMILAB-Pub-77/58-EXP, 1977. 2

[10] C. Rubbia, *Experimental Observation of the Intermediate Vector Bosons W^+, W^-, and Z^0*, Nobel Lecture, 1984. 2

[11] ATLAS Letter of Intent for a General Purpose pp Experiment at the Large Hadron Collider at CERN, CERN-LHCC-92-4, 1992. 6

[12] Particle Data Group, *Review of Particle Physics*, Journal of Physics G Nuclear and Particle Physics, Volume 33, Institute of Physics Publishing, 2006. 7, 15, 20, 22, 131

[13] I. J. R. Aitchison, A. J. G. Hey, *Gauge Theories in Particle Physics*, Volumes I and II, Taylor & Francis Group, 2003. 9

[14] J. Pumplin, D. R. Stump, J. Huston, H. L. Lai, P. Nadolsky, W. K. Tung, *New Generation of Parton Distributions with Uncertainties from Global QCD Analysis*, hep-ph/0201195v3, 2002. 11

[15] A. D. Martin, R. G. Roberts, W. J. Stirling, R. S. Thorne,*Physical Gluons and high-E_T Jets*, hep-ph/0410230v1, 2004. 11

[16] DESY, 2009, *HERA Home Page*, http://adweb.desy.de/mpy/hera 11

[17] G. Altarelli, M. L. Mangano, *Proceedings of the Workshop on Standard Model Physics (and More) at the LHC*, CERN-2000-004, 2000. 12

[18] V. D. Barger, R. J. N. Philips, *Collider Physics*, Updated Edition, Westview Press, 1996. 11, 23, 126

[19] R. K. Ellis, W. J. Stirling, B. R. Webber, *QCD and Collider Physics*, Cambridge University Press, 2003. 15, 17, 19, 22

[20] R. Hamberg, W. L. van Neerven, *A complete calculation of the order α_s^2 correction to the Drell-Yan K-factor*, Nuclear Physics B, Volume 359 (p343-p405), 1991.

R. Hamberg, W. L. van Neerven, T. Matsuura, *Erratum: A complete calculation of the order α_s^2 correction to the Drell-Yan K-factor [Nucl. Phys. B 359 (1991) 343]*, Nuclear Physics B, Volume 644 (p403-p404), 2002. 21

[21] ATLAS Detector and Physics Performance Technical Design Report, Volumes I and II, CERN-LHCC-99-14 and 15, 1999. 24

[22] L. Evans and P. Bryant (editors), *LHC Machine*, JINST 3 (2008) S08001. 26

[23] S. Myers, *The LEP Collider, from Design to Approval and Commissioning*, John Adams Memorial Lecture, CERN, 1990. 26

[24] The ATLAS Collaboration, *The ATLAS Experiment at the CERN Large Hadron Collider*, JINST 3 (2008) S08003. 26

[25] The CMS Collaboration, *The CMS Experiment at the CERN LHC*, JINST 3 (2008) S08004. 26

[26] LHC Conceptual Design Report, CERN-AC-95-05, 1995. 26

[27] CERN, 2009, *CERN: The accelerator complex*, http://public.web.cern.ch/public/en/Research/AccelComplex-en.html 27

[28] ATLAS Inner Detector Technical Design Report, CERN-LHCC-97-16, 1997. 30

[29] ATLAS Liquid Argon Calorimeter Technical Design Report, CERN-LHCC-96-41, 1996. 33

[30] ATLAS Tile Calorimeter Technical Design Report, CERN-LHCC-96-42, 1996. 33

[31] T. Ince, *Position Resolution of the ATLAS Electromagnetic Endcap Calorimeter*, MSc Thesis, University of Victoria, 2005. xiii, 33, 51

[32] ATLAS Muon Spectrometer Technical Design Report, CERN-LHCC-97-22, 1997. 37

[33] ATLAS Level-1 Trigger Technical Design Report, CERN-LHCC-98-014, 1998. 38

[34] ATLAS High Level Trigger, Data Acquisition and Controls Technical Design Report, CERN-LHCC-2003-022, 2003. 39

[35] T. Sjöstrand, S. Mrenna, P. Skands, *PYTHIA 6.4 Physics And Manual*, hep-ph/0603175v2, 2006. 42

[36] G. Corcella, I. G. Knowles, G. Marchesini, S. Moretti, K. Odagiri, P. Richardson, M. H. Seymour, B. R. Webber, *HERWIG 6.5: an event generator for Hadron Emission Reactions with Interfering Gluons (including supersymmetric processes)*, hep-ph/0011363v3, 2002. 42

[37] P. Golonka, Z. Was, *Next to Leading Logarithms and the PHOTOS Monte Carlo*, hep-ph/0604232v1, 2006. 42

[38] J. M. Butterworth, M. H. Seymour, *JIMMY4: Multiparton Interactions in HERWIG for the LHC*, draft write-up, http://projects.hepforge.org/jimmy, 2005. 43

[39] M. A. Dobbs, S. Frixione, E. Laenen and K. Tollefson (editors), *Les Houches Guidebook to Monte Carlo Generators for Hadron Collider Physics*, hep-ph/0403045v2, 2004. 43

[40] GEANT4 Collaboration, *GEANT4: a simulation toolkit*, Nuclear Instruments and Methods A, Volume 506, (p250-p303), 2003. 44

[41] E. Richter-Was, D. Froidevaux, L. Poggioli, *ATLFAST 2.0 a fast simulation package for ATLAS*, ATL-PHYS-98-131, 1998. 46

[42] S. Frixione, B.R. Webber, *Matching NLO QCD computations and parton shower simulations*, hep-ph/0204244, 2002. 49

[43] The ATLAS Collaboration, G. Aad et al., *Expected Performance of the ATLAS Experiment, Detector, Trigger and Physics*, CERN-OPEN-2008-020, Geneva, 2008. 49

[44] J. Han, *The Differential Cross Section Distribution of Drell-Yan Dielectron Pairs in the Z Boson Mass Region*, PhD Dissertation, 2008. 64

[45] M. Boonekamp, Private communication. 64

[46] L. Lyons, *Statistics for nuclear and particle physicists*, Cambridge University Press, 1986. 70

[47] J. Pumplin, D. R. Stump, R. Brock, D. Casey, J. Huston, J. Kalk, H. L. Lai, W. K. Tung, *Uncertainties of predictions from parton distribution functions II: the Hessian method*, hep-ph/0101032v3, 2001. 99

[48] J. M. Campbell, J. W. Huston, W. J. Stirling, *Hard interactions of quarks and gluons: a primer for LHC physics*, Reports on Progress in Physics, Volume 70 (p89-p193), 2007. 99

[49] Fermilab, 2009, *Fermi National Accelerator Laboratory Tevatron Department Beams Division*, http://www-bdnew.fnal.gov/tevatron 114

[50] A. F. Scott, *A Measurement of Low-Mass Drell-Yan Production at the Collider Detector at Fermilab*, PhD Dissertation, 2000. 114

[51] CDF Collaboration, *Measurement of $d\sigma/dM$ and Forward-Backward Charge Asymmetry for High Mass Drell-Yan e^+e^- Pairs from $p\bar{p}$ Collisions at $\sqrt{s} = 1.8$ TeV*, hep-ex/0106047v1, 2001. 114

Appendix A

Kinematics of the Parton Model and the Drell-Yan process

Consider a process $A + B \rightarrow c + X$ as shown in figure A.1 where c is a fermion and X can be any particle(s).

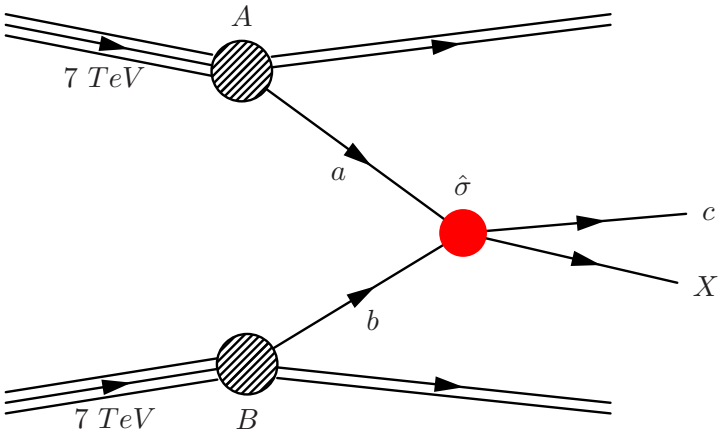

Figure A.1: Schematic diagram of a proton-proton collision.

In the Parton Model, the total cross section for producing the fermion c, in the

lowest order (LO), is calculated as [18]

$$(\sigma)_{\mathrm{LO}} = \sum_{a,b} C_{ab} \int dx_a dx_b \left[f_{a/A}(x_a, Q^2) f_{b/B}(x_b, Q^2) + (A \leftrightarrow B \text{ if } a \neq b) \right] \hat{\sigma} \tag{A.1}$$

where a and b are the partons in the protons A and B, C_{ab} is the initial colour averaging factor, $\hat{\sigma}$ represents the subprocess or constituent level cross section for the interaction of the two partons a and b to form the final state c and X, and $\sum$ is the sum over all possible parton pairs that can produce $c + X$. The term $A \leftrightarrow B$ is

$$A \leftrightarrow B \equiv f_{a/B}(x_b, Q^2) f_{b/A}(x_a, Q^2)$$

to account for the possibility of the parton a coming from the proton B carrying a momentum fraction x_b and the parton b coming from the proton A carrying a momentum fraction x_a. The initial colour averaging factors for quarks and gluons are

$$C_{q\bar{q}} = \frac{1}{9} \ , \ C_{qg} = \frac{1}{24} \ , \ C_{gg} = \frac{1}{64}$$

since there are three and eight different colour charges carried by each quark and gluon, respectively.

The momentum fraction $x_{a,b}$ carried by each parton, ignoring the parton masses, is given by

$$p_{a,b} = x_{a,b} p_{A,B} \tag{A.2}$$

where $p_{a,b}$ ($p_{A,B}$) represents the four-momentum of each parton (proton). Thus, the invariant mass squared $\hat{s}$ of the parton pair, assuming that the protons are in the centre of mass

frame, and there is no angle between the interacting partons, is

$$\begin{aligned}\hat{s} &= (p_a + p_b)^2 \qquad \text{(A.3)}\\ &= \underbrace{m_a^2 + m_b^2}_{0} + 2p_a p_b \\ &= 2(E_a E_b - \underbrace{|\overrightarrow{p_a}|}_{E_a}\underbrace{|\overrightarrow{p_b}|}_{E_b}\underbrace{\cos\theta}_{-1}) \\ &= 4E_a E_b = 4x_a E_A x_b E_B\end{aligned}$$

$$\hat{s} = x_a x_b s = \tau s \qquad \text{(A.4)}$$

where s is the invariant mass squared of the proton pair, and the variable $\tau = x_a x_b$, a number between 0 and 1, is defined in order to simplify future formulae. Rewriting the cross section in terms of x_a and τ yields

$$(\sigma)_{\mathrm{LO}} = \sum_{a,b} C_{ab} \int_0^1 d\tau \int_\tau^1 \frac{dx_a}{x_a} \left[f_{a/A}(x_a, Q^2) f_{b/B}(\frac{\tau}{x_a}, Q^2) + (A \leftrightarrow B \text{ if } a \neq b) \right] \hat{\sigma} \qquad \text{(A.5)}$$

and hence, the differential cross section can be written as

$$\left(\frac{d\sigma}{d\tau}\right)_{\mathrm{LO}} = \sum_{a,b} \frac{d\mathcal{L}_{ab}}{d\tau} \hat{\sigma}(\hat{s} = \tau s) \qquad \text{(A.6)}$$

where

$$\frac{d\mathcal{L}_{ab}}{d\tau} = C_{ab} \int_\tau^1 \frac{dx_a}{x_a} \left[f_{a/A}(x_a, Q^2) f_{b/B}(\frac{\tau}{x_a}, Q^2) + (A \leftrightarrow B \text{ if } a \neq b) \right] \qquad \text{(A.7)}$$

is called parton luminosity since multiplication of it with the parton cross section $\hat{\sigma}$ gives the total cross section in a pp (or hadron-hadron) collision.

In hadron-hadron collisions, it is more convenient to use rapidity, y, in calculations of cross sections or other observables since the hard scatter (ab system) centre of mass moves in the lab frame (i.e. x_a and x_b are not necessarily equal) along the beam axis, and

the shape of observable distributions in y are relativistically invariant. The rapidity is a variable that transforms simply, by adding a constant, under boosts. It is defined as

$$y = \frac{1}{2}\ln\left(\frac{E^{(\text{c.m.})} + p_{||}^{(\text{c.m.})}}{E^{(\text{c.m.})} - p_{||}^{(\text{c.m.})}}\right) = \frac{1}{2}\ln\frac{x_a}{x_b} \tag{A.8}$$

where $E^{(\text{c.m.})}$ is the energy and $p_{||}^{(\text{c.m.})}$ is the longitudinal momentum of the ab system in the AB centre of mass frame. The AB centre of mass frame is the lab frame for the LHC. Pseudorapidity is often used as an approximation for y when mass of a particle is small compared to its energy and is defined as $\eta = -\ln\left(\tan\frac{\theta}{2}\right)$ where θ is the polar angle. The rapidity can be written in terms of x_a and x_b only when assuming that the partons are massless, and there is no angle between them. The momentum fraction $x_{a,b}$ can be rewritten in terms of y and τ as

$$x_{a,b} = \sqrt{\tau}e^{\pm y} \ . \tag{A.9}$$

The Jacobian transformation from variables x_a and x_b to y and τ is

$$\begin{aligned} dyd\tau &= \begin{vmatrix} \frac{dy}{dx_a} & \frac{dy}{dx_b} \\ \frac{d\tau}{dx_a} & \frac{d\tau}{dx_b} \end{vmatrix} dx_a dx_b \\ &= \begin{vmatrix} \frac{1}{2x_a} & \frac{-1}{2x_b} \\ x_b & x_a \end{vmatrix} dx_a dx_b \\ dyd\tau &= dx_a dx_b \end{aligned} \tag{A.10}$$

and therefore the differential cross section in terms of y and τ is

$$\left(\frac{d^2\sigma}{dyd\tau}\right)_{\text{LO}} = \frac{d^2\sigma}{dx_a dx_b} = \sum_{a,b} C_{ab}\left[f_{a/A}(x_a, Q^2) f_{b/B}(\frac{\tau}{x_a}, Q^2) + (A \leftrightarrow B \text{ if } a \neq b)\right]\hat{\sigma} \tag{A.11}$$

and if the longitudinal momentum fraction of the ab system is defined as

$$x = x_a - x_b \tag{A.12}$$

then the momentum fraction x_a can be written in terms of x and τ as follows

$$\begin{aligned} x_a - x_b &= x && \text{(A.13)} \\ x_a - \frac{\tau}{x_a} &= x && \text{(A.14)} \\ x_a^2 - x x_a - \tau &= 0 && \text{(A.15)} \\ x_a &= \frac{1}{2}\left(x + \sqrt{x^2 + 4\tau}\right) && \text{(A.16)} \end{aligned}$$

and similarly x_b can be written as

$$x_b = \frac{1}{2}\left(-x + \sqrt{x^2 + 4\tau}\right) \ . \qquad \text{(A.17)}$$

Hence, the differential cross section can be written in terms of x and τ as

$$\frac{d^2\sigma}{dy d\tau} = (x^2 + 4\tau)^{\frac{1}{2}} \frac{d^2\sigma}{dx d\tau} \qquad \text{(A.18)}$$

since

$$\begin{aligned} x &= \sqrt{\tau}\left(e^y - e^{-y}\right) \\ dx &= \sqrt{\tau}\left(e^y + e^{-y}\right) dy = (x_a + x_b) dy \\ dx &= \left(x^2 + 4\tau\right)^{\frac{1}{2}} dy \ . && \text{(A.19)} \end{aligned}$$

In the practical case of the Drell-Yan process as shown in figure A.2, the total cross section for producing a DY pair (i.e. lepton-antilepton pair) can be, using the Parton Model formulae, calculated to LO as

$$(\sigma)_{LO} = \sum_q \int dx_1 dx_2 \left[f_{q/A}(x_1, m_{ll}^2) f_{\bar{q}/B}(x_2, m_{ll}^2) + (q \leftrightarrow \bar{q}) \right] \hat{\sigma}_{q\bar{q} \to l^+ l^-} \qquad \text{(A.20)}$$

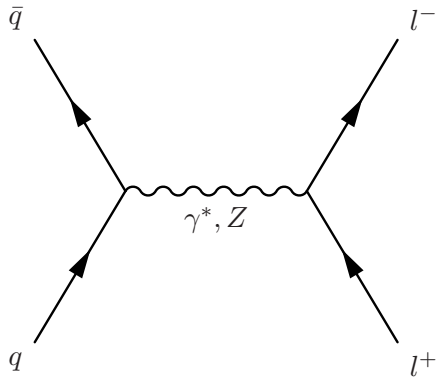

Figure A.2: Feynman diagram of the tree level Drell-Yan process.

where unlike a $p\bar{p}$ collision, $q \leftrightarrow \bar{q}$ term is added explicitly rather than multiplication with a factor of two since there is an imbalance of quarks and anti-quarks in a pp collision due to the valence quarks. In the lowest order, the subprocess cross section $\hat{\sigma}$ due to the exchange of a virtual photon is given by

$$\hat{\sigma}(q(p_1)\bar{q}(p_2) \to \gamma^* \to l^+l^-) = N_c C_{q\bar{q}} \frac{4\pi\alpha^2}{3\hat{s}} e_q^2 \tag{A.21}$$

where

$$\hat{s} = m_{ll}^2 = (p_1 + p_2)^2 = x_1 x_2 s = \tau s \tag{A.22}$$

$$\tau = m_{ll}^2/s \tag{A.23}$$

and p_1 and p_2 are the four-momenta of the quarks. The running electromagnetic coupling, $\alpha \equiv \alpha(m_{ll}^2)$, is given by

$$\alpha(m_{ll}^2) = \frac{\alpha(m_e^2)}{1 - \frac{\alpha(m_e^2)}{3\pi}\left[\sum_f e_f^2 N_c \left(\ln\frac{m_{ll}^2}{m_f^2} - \frac{5}{3}\right)\right]} \tag{A.24}$$

with the fine structure constant $\alpha(m_e^2) = 1/137.036$ [12]. N_c is equal to one for leptons and three for quarks. m_{ll} is the invariant mass of the lepton pair while m_f represents the fermion masses less than m_{ll}. The factor $N_c C_{q\bar{q}} = \frac{1}{3}$ reflects the fact that only three of nine colour combinations are possible matching colours from a quark and antiquark pair that can lead to a colour-less virtual photon. The subprocess differential cross section for producing a DY pair of mass m_{ll} can be calculated as

$$\frac{d\hat{\sigma}}{dm_{ll}^2} = N_c C_{q\bar{q}} \frac{4\pi\alpha^2}{3m_{ll}^2} e_q^2 \delta(\hat{s} - m_{ll}^2) \tag{A.25}$$

where the Dirac delta function $\delta(\hat{s} - m_{ll}^2)$ imposes $\hat{s} = m_{ll}^2$. Hence the total differential cross section is given by

$$\begin{aligned}
\left(\frac{d\sigma}{dm_{ll}^2}\right)_{LO} &= \int_0^1 dx_1 dx_2 \sum_q \left[f_{q/A}(x_1, m_{ll}^2) f_{\bar{q}/B}(x_2, m_{ll}^2) + (q \leftrightarrow \bar{q})\right] \times \frac{d\hat{\sigma}}{dm_{ll}^2}(q\bar{q} \to l^+ l^-) \\
\left(\frac{d\sigma}{dm_{ll}^2}\right)_{LO} &= N_c C_{q\bar{q}} \frac{4\pi\alpha^2}{3m_{ll}^2} \int_0^1 dx_1 dx_2 \delta(x_1 x_2 s - m_{ll}^2) \\
&\quad \times \sum_q e_q^2 \left[f_{q/A}(x_1, m_{ll}^2) f_{\bar{q}/B}(x_2, m_{ll}^2) + (q \leftrightarrow \bar{q})\right]
\end{aligned} \tag{A.26}$$

and using the following Dirac delta function property

$$\delta(x_1 x_2 s - m_{ll}^2) = \frac{1}{s}\delta(x_1 x_2 - m_{ll}^2/s) = \frac{1}{s}\delta(x_1 x_2 - \tau) \ , \tag{A.27}$$

the total differential cross section can be rewritten in terms of $\tau = m_{ll}^2/s$ as

$$\begin{aligned}
\left(\frac{d\sigma}{dm_{ll}^2}\right)_{LO} &= N_c C_{q\bar{q}} \frac{4\pi\alpha^2}{3m_{ll}^4} \tau \int_0^1 dx_1 dx_2 \delta(x_1 x_2 - \tau) \\
&\quad \times \sum_q e_q^2 \left[f_{q/A}(x_1, m_{ll}^2) f_{\bar{q}/B}(x_2, m_{ll}^2) + (q \leftrightarrow \bar{q})\right] \\
\left(\frac{d\sigma}{dm_{ll}}\right)_{LO} &= N_c \frac{8\pi\alpha^2}{3m_{ll}^3} \sum_q e_q^2 \frac{\tau d\mathcal{L}(\tau)}{d\tau}
\end{aligned} \tag{A.28}$$

which depends only on τ, but not on m_{ll} or s individually. $\frac{d\mathcal{L}(\tau)}{d\tau}$ was defined in equation 2.6.